ABSTRACT

Title of Dissertation: Self-Assembled InAs/GaAs Quantum Dot Solar Cells

Tian Li, Doctor of Philosophy, 2015

Dissertation directed by: Professor, Mario Dagenais, Electrical Engineering

Our work focuses on experimental and theoretical studies aimed at establishing a fundamental understanding of the principal electrical and optical processes governing the operation of quantum dot solar cells (QDSC) and their feasibility for the realization of intermediate band solar cell (IBSC).

Uniform performance QD solar cells with high conversion efficiency have been fabricated using carefully calibrated process recipes as the basis of all reliable experimental characterization. The origin for the enhancement of the short circuit current density (Jsc) in QD solar cells was carefully investigated. External quantum efficiency (EQE) measurements were performed as a measure of the below bandgap distribution of transition states. In this work, we found that the incorporation of self-assembled QDs interrupts the lattice periodicity and introduce a greatly broadened tailing density of states extending from the

bandedge towards mid-gap. In particular, the below-bandgap photocurrent generation has been attributed to transitions via confined energy states and background continuum tailing states. Photoluminescence measurement is used to measure the energy level of the lowest available state and the coupling effect between QD states and background tailing states because it results from a non-equilibrium process. A basic I-V measurement reveals a degradation of the open circuit voltage (Voc) of QD solar cells, which is related to a one sub-bandgap photon absorption process followed by a direct collection of the generated carriers by the external circuit. We have proposed a modified Shockley-Queisser (SQ) model that predicts the degradation of Voc. Whenever an energy state within the forbidden gap can facilitate additional absorption, it can facilitate recombination as well. We have also investigated the QD trapping effects as deep level energy states. Electron-doping helps with better carrier collection efficiency, however, we have also measured a smaller transition probability from valance band to QD states as a direct manifestation of the Pauli Exclusion Principle.

The non-linear performance is of particular interest. For the first time, we are able to distinguish the nonlinearity effect by 1PA and 2PA process. The observed 2PA current under off-resonant and on-resonant excitation comes from a two-step transition via the tailing states instead of the QD states.

Self-Assembled InAs/GaAs/ Quantum Dot Solar Cells

By

Tian Li

Dissertation submitted to the Faculty of the Graduate School of the
University of Maryland, College Park, in partial fulfillment
of the requirements for the degree of

Doctor of Philosophy

2015

Advisory Committee:
Professor Mario Dagenais, Chair
Professor Martin Peckerar
Professor Christopher C. Davis
Assistant Professor Liangbing Hu
Professor Lourdes G. Salamanca-Riba

© Copyright by

Tian Li

2015

Dedication

To my family

Acknowledgements

Obtaining a PhD is not just a journey for me. It has changed me in a way that I couldn't expect. Probably none of my future experiences will ever again match this immense privilege with enthusiasm, passion, and willingness to take on challenges. I would like to express my greatest gratitude to my academic advisor Prof. Mario Dagenais, for his constant guidance, motivation and direction during my stay here. I am extremely grateful to him for giving me a strong interest in this field, and for his vision in guiding this thesis work.

I am also gratefully thankful for the courses I have taken here. The ENEE 691 Optical Communication course by Prof. Dagenais has cultivated in me an enthusiasm in the field especially with his own valuable experience. I am grateful to Prof. Peckerar for his kindness and expertise in solid state physics. I still benefit from the lectures in ENEE 601 and the academic discussions including the C-V profiling techniques and Schottky junction analysis (Chapter 3.1). During last semester, I had the honor to work as the Teaching Assistant to ENEE 496 by Prof. Davis. I was deeply impressed by his engaging lectures. When I first joined the group, I knew very little about solar cells. During these years, I found myself in debt with all the lectures I have taken and all the discussions I had in this field. Dr. Munday's lecture ENEE789C on solar energy conversion has cultivated in me a systematic understanding of solar cell's performance, which inspired my work

on the modified Shockley Queisser model incorporating the tailing state (Chapter 4.8). Prof. Salamanca-Riba's course on defects in materials (ENMA 671) has contained valuable information in characterizing the semiconductor materials defect-related properties especially for 1-D and 2-D structures. Dr. Liangbing Hu's course on Nanotechnology for Energy has introduced many cutting-edge research and applications which have greatly broadened my horizon. The list could go on.

I wish to thank the members of my dissertation committee, namely Prof. Mario Dagenais, Prof. Martin Peckerar, Prof. Christopher C. Davis and Dr. Liangbing Hu and Prof. Lourdes G. Salamanca-Riba for sparing their time and effort.

Special thanks are due to Tom Loughran, John Abrahams, Jonathan A. Hummel, Mark Lecates and Jim O'Connor at Fablab in Nanocetner who have been extremely helpful to me in the usage of fabrication tools. Their expertise and kindness have greatly accelerated my progress in the development of the process recipes (Chapter 2) that I have used in this thesis.

Finally, I would like to thank my parents for always having been supportive of me in my academic pursuits.

Table of Contents

Section **Page**

List of Figures ……………………….……………………..……….……..ix

List of Tables ……………………….……………………………..…..xvii

List of Publications……………………………..………………………......xix

1 Introduction.. 1

1.1 Abstract.. 1

1.2 Background and current status.. 4

1.3 Dissertation outline.. 13

2 An overview of GaAs fabrication techniques and the process flow of GaAs solar cell fabrication... 17

2.1 Cleaning.. 17

2.2 Etching.. 19

2.2.1 Dry etching and its application to our process................................ 21

2.2.2 Wet etching and its application to our process................................ 23

2.3 Electrode contacts 25

2.3.1 Electrode formation 25

2.3.2 The electrode contact characterization 27

2.3.3 Schottky contacts and barrier height extraction 31

2.4 Passivation 34

2.5 Device thinning down 39

2.5.1 Lift-off 39

2.5.2 Backside thinning 41

2.6 The developed process flow for GaAs solar cell fabrication 42

3 Major characterization techniques and bulk GaAs solar cell characterization 47

3.1 Solar cell parameters and major characterization methods 47

3.1.1 Current-voltage characterization 47

3.1.2 External quantum efficiency characterization 50

3.1.3 Photoluminescence /Electroluminescence measurement 51

3.1.4 Doping profile characterization with Hall measurement and Capacitance-Voltage measurement 55

3.2 Comparison between different bulk GaAs solar cells 59

3.2.1 The effect of absorption layer doping level...................................... 59

3.2.2 The effect of absorption layer thickness... 61

4 Quantum dot solar cells.. 64

4.1 InAs/GaAs quantum dot solar cell... 64

4.2 The current-voltage characteristics of QD solar cell 67

4.3 The existence of an extended Urbach tail 70

4.4 The effect of Urbach tail on below band-gap absorption and the derivation of Urbach energy 73

4.5 Derivation of band tail absorption width 75

4.6 Derivation of Quantum dot and wetting layer absorption coefficient 79

4.7 The effect of Urbach tail on the QD device's EQE, IV, and PL results ... 86

4.8 The analysis of Voc degradation and Jsc enhancement from a modified Shockley-Queisser model 88

4.8.1 Comparison of the width of the tailing states from an EQE measurement between InAs/GaAs QDs and In0.5Ga0.5As/GaAs QDs........ 97

4.8.2 The effect of tailing states on the carrier relaxation process 99

4.8.3 The effect of tailing states on the carrier collection process.......... 104

5 Investigation of Non-linear Sub-bandgap Photocurrent Generation and its implication in the realization of intermediate band solar cell model 106

5.1 Current status of non-linear properties in QD solar cells 106

5.2 Non-linear properties in QDSC for off-resonant excitation 108

5.3 Non-linear properties in QDSC for on-resonant excitation 117

5.4 Characterization of signal generated with second transition via IR absorption and its implication in the realization of IBSC model.................... 123

6 Electron trapping properties of QDs and the electron-doping effect... 130

6.1 The impact of electron delta doping to quantum dots on short circuit current density.. 131

6.2 The impact of electron doping on quantum dot energy states absorption and emission 137

7 Summary.. 142

Appendix A……………………………………………………….………145

Appendix B…………………………………………………………………152

Bibliography…………………………………………………………...156

List of Figures

Figure 1-1: Loss mechanisms in a traditional solar cell: (1) transmission loss; (2) thermalization loss; (3) junction loss; (4) contact loss; (5) recombination loss 5

Figure 1-2: The proposal of the intermediate band solar cell model 6

Figure 1-3: (a) Simplified diagram for the illustration of the concept of IBSC; (b) efficiency promise of IBSC compared with tandem cell and single gap cell (Luque and Mart í 1997a)...7

Figure 1-4: The self-assembled growth mode. QDs are formed with a layer of quantum well (wetting layer) left behind. 9

Figure 1-5: Utilizing QDs to facilitate below-bandgap photon absorption 11

Figure 2-1: (a) A GaAs device that is etched by wet etching method. (b) A GaAs device that is etched by dry etching method. The scale bar is the same in both devices. As can be seen, the sidewall after wet etching is much thicker than that after dry etching process. The etch profiles largely depends on crystal orientation after wet etching while dry etching process is more isotropic. 22

Figure 2-2:Bulk GaAs solar cell IV performance before and after citric acid treatment. The Voc has increased from 0.84 V to 0.91 V and the Jsc has increased from 20.2 mA/cm^2 to 23.2 mA/cm^2. 24

Figure 2-3: Illustration of lift-off method for electrode deposition 26

Figure 2-4: Pattern of cTLM for characterization of contact resistance 28

Figure 2-5: Fabricated cTLM pattern image under optical microscope 29

Figure 2-6: Measured IV curves with difference value of ***d*** in cTLM pattern for n and p GaAs contact layer with a doping density of 3e18 cm^{-3}and 5e18 cm^{-3} respectively for the extraction of contact resistance and sheet resistance. 30

Figure 2-7: Illustration of the formation of Schottky barrier (web resource) 32

Figure 2-8: Example of a Schottky barrier. (a) IV plot of AZO/perovskite contact and (b) the semi-log plot to extract parameter *Is*. 33

Figure 2-9: After passivation, the value of Voc has increased from 0.92 V to 0.94 V while the Jsc has increased from 20.4 mA/cm^2 to 22.9 mA/cm^2. The red curve is the measured data while the blue curve is from an experimental fitting based on the two-diode model. 38

Figure 2-10. Lift-off device (device that has been lift off from GaAs substrate with a thickness of 2 μm and e-beam deposited top and backside electrodes) 41

Figure 2-11: Illustration of the process flow of GaAs device...............................44

Figure 3-1: Simplified solar cell diode model 48

Figure 3-2: (a) The dark IV characteristics for bulk GaAs solar cell M1215. (b) From a fitting under reserve bias, the dark saturation current can be estimated. 50

Figure 3-3: External quantum efficiency setup..51

Figure 3-4: Photoluminensence setup with halogen lamp as light source. A 700 nm short pass filter is inserted (GaAs bandgap is around 880 nm) 53

Figure 3-5: A (500 μm)^2 bulk GaAs device illuminating under (a) 0.7 V and (b) 1 V bias. The area close to the wired electrode bar is brighter due to a higher generated current density. 54

Figure 3-6: The device configuration for Capacitance-voltage profiling technique 56

Figure 3-7: Measured CV curve and the derived doping profile for a Fe-doped GaN sample patterned with Ti/Al/Ni/Au electrodes 58

Figure 4-1: 1×1 μm^2 atomic force microscopy image of QDs, showing a sheet density of around $\mathbf{3.8 \times 1010/cm2}$...66

Figure 4-2: (a) Layer diagram for bulk device (b) Layer diagram for quantum dot device. 67

Figure 4-3: (a) Measured and fitted current-voltage characteristics for bulk and QD sample before anti-reflection coating (b) Current-voltage characteristics for quantum dot sample before and after anti-reflection coating. 68

Figure 4-4: Energy diagram illustrating exponential distribution of tailing density of states for (a) an InAs quantum dot inserted region and (b) a bulk GaAs layer. 71

Figure 4-5: Density of states distribution diagram of the tailing states superposed with the quantum dots and wetting layer energy states...72

Figure 4-6: (a) Schematics of proposed interdot carrier transfer mechanism through continuum density of states due to Urbach tail absorption in the GaAs matrix in intrinsic layer and (b) External quantum efficiency of GaAs/InAs quantum dot sample with no anti-reflection coating. The Urbach tail contributions for both devices are shown by the dotted lines. Note that the Urbach tail arising from the QD region has a much smaller slope, meaning a much higher characteristic width E1 for the absorption edge. Absorption

peaks corresponding to different size QDs or QD transition energies are observed. 74

Figure 4-7: (a) External quantum efficiency due to carrier generation via the Urbach tail, the QD and the WL energy levels (b) derived quantum dot and wetting layer absorption coefficient and the Gaussian lineshape fitting for multiple transitions.............................84

Figure 4-8: (a) The perturbation of the band edges by Coulomb interaction with inhomogeneously distributed impurities (Pankove, 1975). This leads to (b) the reduction between the separation of electron chemical potential and hole chemical potential, which will yield a reduction in Voc. 90

Figure 4-9: The emission functions for SQ model assumption, GaAs bulk device and InAs/GaAs QD device respectively. 92

Figure 4-10: Integration of black-body radiation and emissivity that yields dark saturation current density with 1) steeply rising emission edge and 2) exponential rising emission edge...................................93

Figure 4-11: Integration of black-body radiation of the sun and absorptivity that yields light-generated current density with 1) steeply rising absorption edge and 2) exponential rising absorption edge 96

Figure 4-12: Semilog EQE plot to extract Urbach energy for InAs/GaAs QD device and $In_{0.5}Ga_{0.5}As$/GaAs QD device 99

Figure 4-13: Photoluminescence measurements for InAs/GaAs QD device and $In_{0.5}Ga_{0.5}As$/GaAs QD device..101

Figure 4-14: IV performance comparison for InAs/GaAs QD device and $In_{0.5}Ga_{0.5}As$/GaAs QD device 102

Figure 5-1: One low energy photon excites electron from the valance band to the below-bandgap tailing density of states while the tail also functions as a collection pathway so that the carriers that are generated by this 1PA process can be detected. Meanwhile, the tailing density of states can also act as an intermediate level to facilitate a two photon absorption (2PA) process. The electrons that are excited by a 2PA process will thermalize to the bandedge and will be detected as the 2PA contributed photocurrent. 107

Figure 5-2: Z-scan configuration of fabricated quantum dot device 109

Figure 5-3: A sub-bandgap photon generates an electron on the energy states within the gap. The free electron will either leak to the matrix via a continuum tailing DOS (1PA process as shown on the LEFT side) or be excited again by a sequential absorption of another sub-bandgap photon (2PA process as shown on the RIGHT side). .109

Figure 5-4: (a) Diagram of quantum dots solar cell (b) The position of tailing states of both the QD device and the bulk GaAs device (c) Current-voltage characteristics and (d) Photoluminescence measurement with one peak centered around QD ground state 1.12 eV. 111

Figure 5-5: (a) Photocurrent dependence along with propagation direction for ***1550 nm*** laser (b) The quadratic photocurrent plot indicating a 2PA photocurrent generation efficiency of around 0.01 nA/mW^2 (c) 1PA photocurrent generation efficiency plot with different beam power where the nonlinear component is due to local heating. 116

Figure 5-6: (a). QD device's response of ***1060 nm*** laser. (b)(c)(d) A comparison between fitted curve and measured data with 49.2 mW, 41.0 mW and 32.8mW input power. A saturation current density of 10 $mW/\mu m^2$ was fitted under all input powers. 121

Figure 5-7: Low temperature IR response setup...129

Figure 6-1: (a) Current-voltage characteristics of undoped, 2e/dot and 4e/dot devices (b) above bandgap absolute EQE of 0e/dot and 4e/dot 134

Figure 6-2: The majority of the above bandgap photo carriers are generated close to the device surface due to the large absorption coefficient

of the incident photons. (a) Holes are directly collected at the p-electrode while above bandgap generated electrons need to transport through the QDs region and collected at n-electrode. (b) Electrons transport through a single QDs layer. (c) Electrons transport through one quantum dot. 136

Figure 6-3: Normalized EQE for evaluating below bandgap photon response ...138

Figure 6-4: Photoluminescence of 0e/dot, 2e/dot and 4e/dot devices 139

List of Tables

Table 2-1: Comparison between dry etching and wet etching 20

Table 2-2: Summary of the key parameters of the cell before and after removing top layer 25

Table 2-3: Contact resistant derivation of n- and p- electrodes using cTLM 31

Table 2-4 Summary of the performance before/after passivation 37

Table 3-1: Structure comparison between M1091 and M1215 60

Table 3-2: The performance comparison between M1091 and M1215 61

Table 3-3: Structure comparison between M1215/M1216/M1217 62

Table 3-4: Performance comparison of M1215, M1216, M1217 before passivation and AR coating 63

Table 4-1: Fitted parameters based on two diode model before anti-reflection coating (Illuminated area is used to calculate current density) 69

Table 4-2: Fit transition states of QD absorption, compared with results measured by photo reflectance. Unit: eV 82

Table 4-3: Summary of the devices with step-like absorption edge, a 13 meV tailing width and a 50 meV tail width. 95

Table 4-4: Performance comparison among different InAs or InGaAs QD devices
.... 104

Table 6-1 Device Performance of 0e/dot, 2e/dot and 4e/dot device.................. 131

List of Publications

[1]. **Li, Tian**, Bartolo, R.E., Dagenais, M., Challenges to the Concept of an Intermediate Band in InAs/GaAs Quantum Dot Solar Cells. **Appl. Phys. Lett.** 103, 141113, 2013

[2]. **Li, Tian** and Dagenais, M., Below-Bandgap Absorption in InAs/GaAs Self-Assembled Quantum Dot Solar Cells, **Progress in Photovoltaics: Research and Applications.** 2014 doi:10.1002/pip.2515 (Impact Factor: 9.696)

[3]. **Li, Tian**, Lu, H., Fu, L., Tan, H., Jagadish, C. and Dagenais, M., Enhanced Carrier Collection Efficiency and Reduced Quantum State Absorption by Electron Doping in Self-Assembled Quantum Dot Solar Cells, **Appl. Phys. Lett.** 106, 053902, 2015

[4]. **Li, Tian** and Dagenais, M., Non-Resonant Below-Bandgap Two-Photon Absorption in Quantum Dot Solar Cells, **Appl. Phys. Lett.** 106, 171101, 2015

[5]. **Li, Tian**, Amirloo, J., Murray, J., Sablon, K.A., Little, J., Uppal, P., Munday, J., Dagenais, M., A comparison of bulk and quantum dot GaAs solar cells, **IEEE Photonics Conference (IPC)**, pp. 194–195, 2012

[6]. (**Invited**) Dagenais, M., **Li, Tian**, Zhang, Y., Bartolo, R., Intermediate Band Solar Cells: Promises and Reality, **International Photonics and**

Optoelectronics Meetings (POEM), Optical Society of America, p. ASa2A.1, 2013

[7]. **Li, Tian** and Dagenais, M., GaAs/InAs Quantum Dot High Efficiency Solar Cell, **IEEE Photonics Conference (IPC)**, pp. 572–573, 2013

[8]. **Li, Tian** and Dagenais, M., Urbach Tail in Intermediate Band InAs/GaAs Quantum Dot Solar Cells. **40th IEEE Photovoltaic Specialist Conference**, 2014

[9]. Dagenais, M and **Li, Tian**, Challenges to the Realization of Intermediate Band Solar Cells using InAs/GaAs Quantum Dots. **35th Piers**, 2014

[10]. **(Invited)** Dagenais, M and **Li, Tian**, Challenges to the Concept of Intermediate Band Solar Cells based on Quantum Dots. **Latin America Optics & Photonics Conference**, 2014

[11]. **Li, Tian** and Dagenais, M., Investigation of Room Temperature Non-linear Sub-bandgap Photocurrent Generation in InAs/GaAs Quantum Dot Solar Cells. **42nd IEEE Photovoltaic Specialist Conference**, 2015

[12]. **Li, Tian**, Lu, H., Fu, L., Tan, H., Jagadish, C. and Dagenais, M., The Role of Electron-doping and the Urbach Tail on Quantum Dot Charge Trapping Dynamics. **Fall MRS**, 2015

[13]. **Li, Tian** and Dagenais, M., Modified Shockley-Queisser Limit for Quantum Dot Solar Cells. **42nd IEEE Photovoltaic Specialist Conference**, 2015

[14]. **Li, Tian** and Dagenais, M., IEEE Student poster competition in optics and photonics, 04/2013

[15]. **Li, Tian** and Dagenais, M., ICAM Workshop, 11/2011

1 Introduction

This chapter introduces the topic of the dissertation. First an abstract for the dissertation is presented, along with a brief summary of our first-time contributions. Next the background is described. Finally, the organization of the rest of the dissertation is outlined.

1.1 Abstract

Our work focuses on experimental and theoretical studies aimed at establishing a fundamental understanding of the principal electrical and optical processes governing the operation of quantum dot solar cells (QDSC) and their feasibility for the realization of intermediate band solar cell (IBSC).

Uniform performance QD solar cells with high conversion efficiency have been fabricated using carefully calibrated process recipes as the basis of all reliable experimental characterization. The origin for the enhancement of the short circuit current density (Jsc) in QD solar cells was carefully investigated. External quantum efficiency (EQE) measurements were performed as a measure of the below bandgap distribution of transition states. In this work, we found that the incorporation of self-assembled quantum dots (QDs) interrupts the lattice periodicity and introduce a greatly broadened tailing density of states extending from the bandedge towards mid-gap. A below-bandgap density of states (DOS) model with an extended Urbach tail has been developed. In particular, the below-

bandgap photocurrent generation has been attributed to transitions via confined energy states and background continuum tailing states. Photoluminescence measurement is used to measure the energy level of the lowest available state and the coupling effect between QD states and background tailing states because it results from a non-equilibrium process. A basic I-V measurement reveals a degradation of the open circuit voltage (Voc) of QD solar cells, which is related to a one sub-bandgap photon absorption process followed by a direct collection of the generated carriers by the external circuit. We have proposed a modified Shockley-Queisser (SQ) model that predicts the degradation of Voc compared with a reference bulk device. Whenever an energy state within the forbidden gap can facilitate additional absorption, it can facilitate recombination as well. If the recombination is non-radiative, it is detrimental to solar cell performance. We have also investigated the QD trapping effects as deep level energy states. Without an efficient carrier extraction pathway, the QDs can indeed function as mobile carriers traps. Since hole energy levels are mostly connected with hole collection under room temperature, the trapping effect is more severe for electrons. We have tried to electron-dope the QDs to exert a repulsive Coulomb force to help improve the carrier collection efficiency. We have experimentally observed a 30% improvement of Jsc for 4e/dot devices compared with 0e/dot devices. Electron-doping helps with better carrier collection efficiency, however, we have also measured a smaller transition probability from valance band to QD states as a direct manifestation of the Pauli Exclusion Principle.

The non-linear performance is of particular interest. With the availability of laser with on-resonance and off-resonance excitation energy, we have explored the photocurrent enhancement by a sequential two-photon absorption (2PA) process via the intermediate states. For the first time, we are able to distinguish the nonlinearity effect by 1PA and 2PA process. The observed 2PA current under off-resonant and on-resonant excitation comes from a two-step transition via the tailing states instead of the QD states. However, given the existence of an extended Urbach tail and the small number of photons available for the intermediate states to conduction band transition, the experimental results suggest that with the current material system, the intensity requirement for an observable enhancement of photocurrent via a 2PA process is much higher than what is available from concentrated sun light. In order to realize the IBSC model, a matching transition strength needs to be achieved between valance band to QD states and QD states to conduction band. However, we have experimentally shown that only a negligible amount of signal can be observed at cryogenic temperature via the transition from QD states to conduction band under a broadband IR source excitation. Based on the understanding we have achieved, we found that the existence of the extended tailing density of states together with the large mismatch of the transition strength from VB to QD and from QD to CB, has systematically put into question the feasibility of the IBSC model with QDs.

1.2 Background and current status

Solar cell is a general term for all the devices that can convert light into electricity. The most common form of solar cell is based on a PN junction semiconductor. The first generation solar cell came with no surprise as a silicon-based photovoltaic cell, since silicon is the most abundant semiconductor material. However, it typically requires a thickness of over 100 μm. Its indirect bandgap also implies that it has a low absorption coefficient. The second-generation solar cell is a thin film solar cell coming from a variety of materials such as CdTe, CIGS, CZTS. They generally have a very high absorption coefficient so that only a few micrometer thickness is needed for the absorption. The photovoltaics industry relentlessly pushes towards an ever-increasing solar conversion efficiency, just like the microelectronics industry pushes toward smaller features.

There are several major fundamental loss mechanisms for a solar device including transmission loss, thermalization loss, contact loss, junction loss and recombination loss. For a traditional solar cell, all the photons with energy smaller than the bandgap are transmitted without being used. This is called "transmission loss". When the photons with energy higher than the bandgap are absorbed, hot carriers are generated and then thermalized to the band edge. The extra energy is then released to the lattice in the form of generated heat. Thus the energy above the bandgap is wasted. This is called "thermalization loss". Contact loss is the

energy wasted at the interface of an electrode with the semiconductor material, while the energy loss in the active region is the junction loss. Finally, recombination loss is the non-ideal carrier recombination that reduces the cell's overall conversion efficiency.

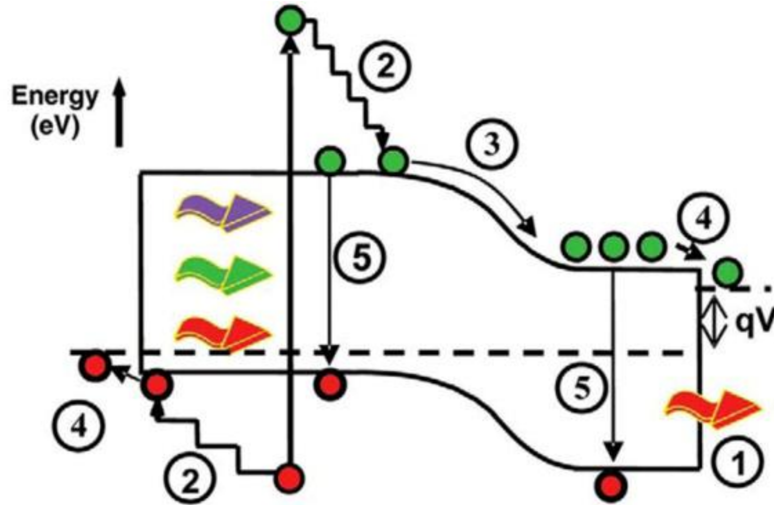

Figure 1-1: Loss mechanisms in a traditional solar cell: (1) transmission loss; (2) thermalization loss; (3) junction loss; (4) contact loss; (5) recombination loss

To meet the urgent need for high performance thin film solar cell technology, new concepts have been proposed and in some ways break the fundamental limit of solar cell. They are the so-called "third generation" solar cells. One of the most pursued paths among them is utilizing nano-scale structures. Quantum dot based solar cells can be considered as "new generation" or "third generation" photovoltaic (PV) devices. New advances in quantization effects in semiconductors allow for the possibility of these nanocrystals to be incorporated in the regular semiconductor materials. Interest in using III-V quantum dots

(QDs) to raise the sub-gap photocurrent has arisen following the recent proposal for the introduction of an intermediate band solar cell (IBSC)(Luque and Martí 1997). The IBSC model suggests taking advantage of a two-step absorption within the forbidden band with longer wavelength photons so that a better coverage of the solar spectrum, at the meantime maintaining an open circuit voltage, can be achieved, as shown in Figure 1. Lower energy photons can thus be utilized which will reduce the transmission loss.

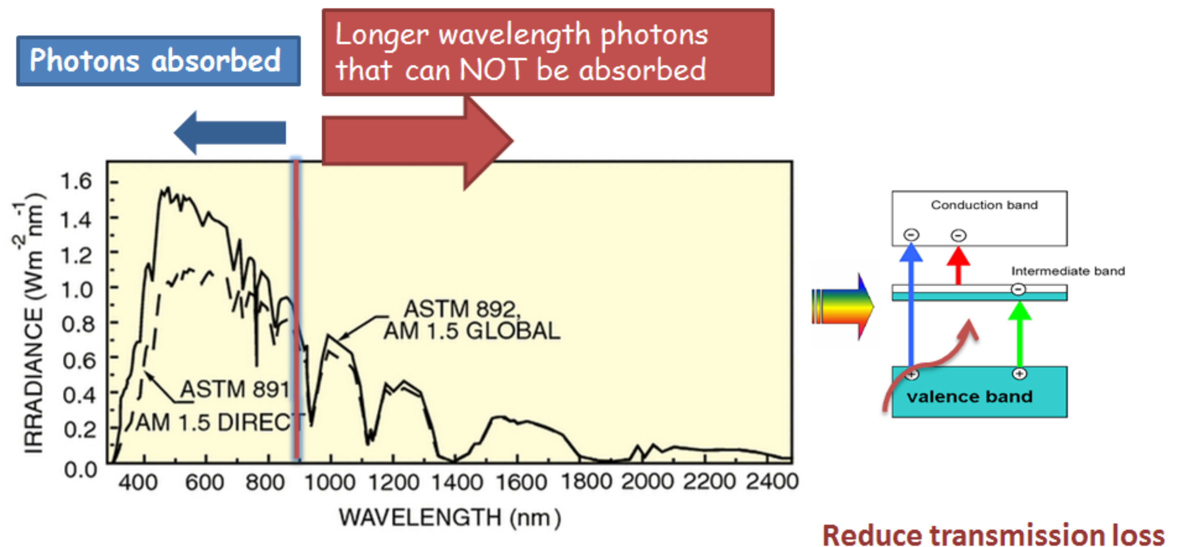

Figure 1-2: The proposal of the intermediate band solar cell model

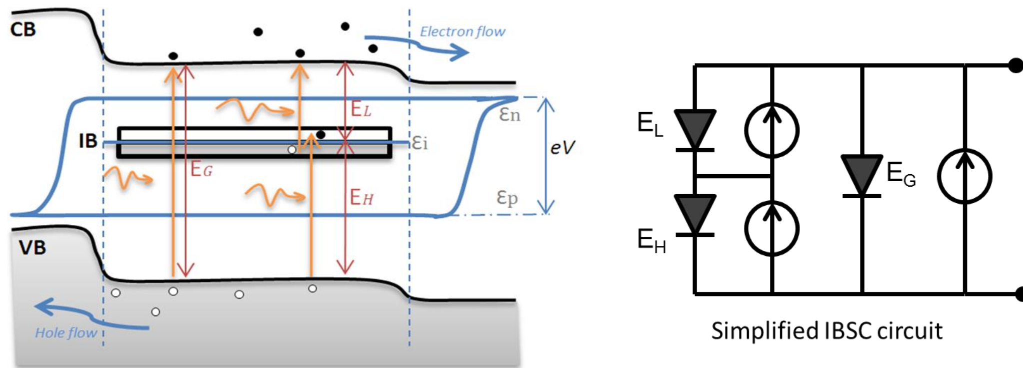

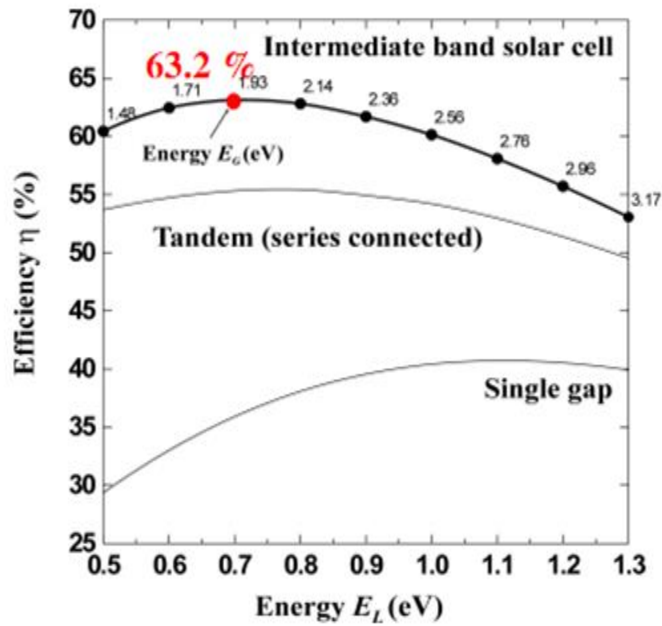

Figure 1-3: (a) Simplified diagram for the illustration of the concept of IBSC; (b) efficiency promise of IBSC compared with tandem cell and single gap cell (Luque and Mart í 1997a).

The non-concentrator solar cell efficiency has now reached 28.8% in single junction thin film GaAs solar cell (Braun et al., 2013; Green et al., 2013; Miller et al., 2012) under the global AM 1.5 spectrum at 25 ℃. The Shockley-Queisser efficiency limit (Shockley and Queisser, 1961) for a single-junction solar cell is 33.5%. The non-concentrator cell record for a 3-junction solar cell was obtained by Sharp in an InGaP/GaAs/InGaAs solar cell and is 37.5% (Green et al., 2013). The 3-junction solar cell breaks the Shockley-Queisser limit but at the price of increased complexity. In 1997, the concept of an intermediate band solar cell was introduced by Luque and Marti (Luque and Mart í 1997b). It is a single junction solar cell and it promises to realize high conversion efficiency at a low level of complexity. In addition to the advantages of single junction solar cells, the intermediate band solar cell model potentially increases the photocurrent without affecting the open circuit voltage, thus increasing the overall conversion efficiency.

It has been suggested that the intermediate band solar cell concept can be implemented using InAs QDs in a GaAs barrier material (Luque and Mart í 2010). In such a system, it is predicted that, the non-concentrator efficiency can be 30.2%. Under concentration, the intermediate band solar cell efficiency in this material system increases to 51.6%, as compared to 36.7% for bulk GaAs solar cells, under a 1000 sun concentration. Since the technology of InAs quantum dots is relatively well-understood, the InAs (or the InGaAs) QD solar cell has become the standard prototype intermediate band solar cell (Bailey et al., 2012; Jolley et

al., 2010; Oshima et al., 2010; Shoji et al., 2013; Sugaya et al., 2012a; Tanabe et al., 2012).

The InAs/GaAs QDs are formed in the self-assembled growth mode. It is by far the most commonly used method to fabricate semiconductor quantum dots. During the epitaxial growth of highly strained material, under the Stranski-Krastanov growth mode, three-dimensional islands are formed following the creation of a two-dimensional wetting layer. The resulting strained nanoscale islands are pyramidal in shape. The intermediate level arises from the confined states of the electrons in the potential well created by the conduction band offset between the dot and the matrix material.

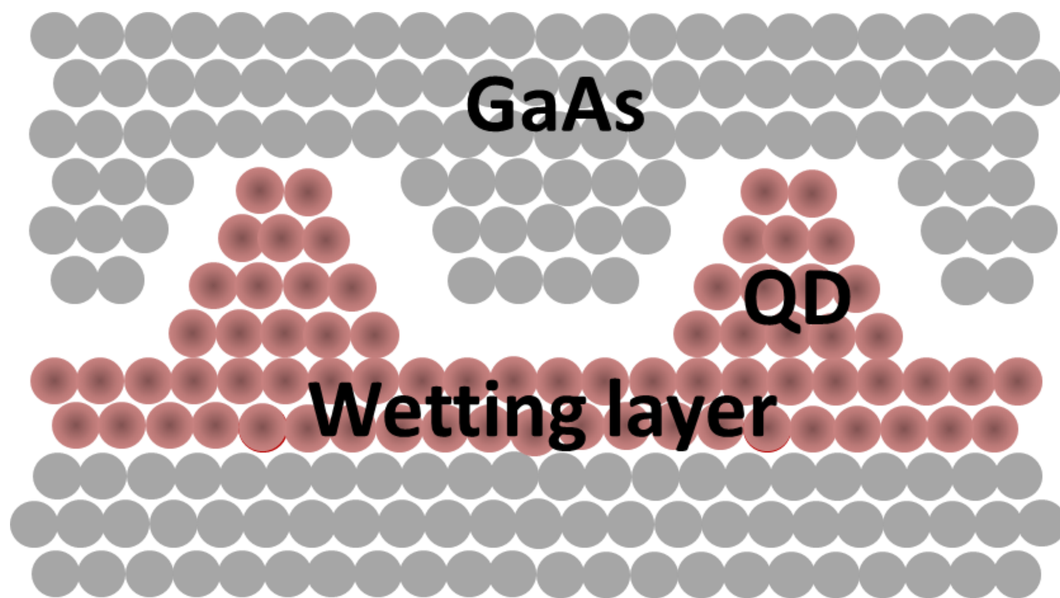

Figure 1-4: The self-assembled growth mode. QDs are formed with a layer of quantum well (wetting layer) left behind.

Quantum dots are semiconductor nanocrystals immersed in a higher band gap semiconductor matrix. The intermediate band arises from the confined states of electrons in the tridimensional potential wells created by the conduction band offset between the dot and the matrix material. If the density of quantum dots is sufficiently high, the intermediate state forms a band due to the overlapping wavefunctions. A quantum dot spacing of order 10 nm or less is required for the formation of a band. But spacing around 10 nm will create severe line dislocations that would sacrifice the device's performance. Consequently, under the current growth condition, individual energy levels are formed instead of a band. In this way, the model suggests that photons with energy less than the GaAs band gap can be absorbed by transitions that pump an electron from the valence band to the quantum dot states and subsequently from the QD states to the conduction band. Therefore, an extra path is now allowed for an electron to make the transition from the valence band to the conduction band. It involves the absorption of two single photons. This extra path leads to the absorption of two lower energy photons below the bandgap that would otherwise not be possible in a bulk single bandgap solar cell. By the same token, the photocurrent is also enhanced and the voltage given by the conduction and valence band quasi-Fermi levels at the n- and p-contacts, respectively, is expected to stay the same. According to the model, no extra photocurrent should be detected in the outside circuit from the single photon absorption process acting alone from the valence band to the intermediate band.

This is a key requirement for the operation of the intermediate band solar cell and, as we will discuss, is a very difficult condition to realize in practice.

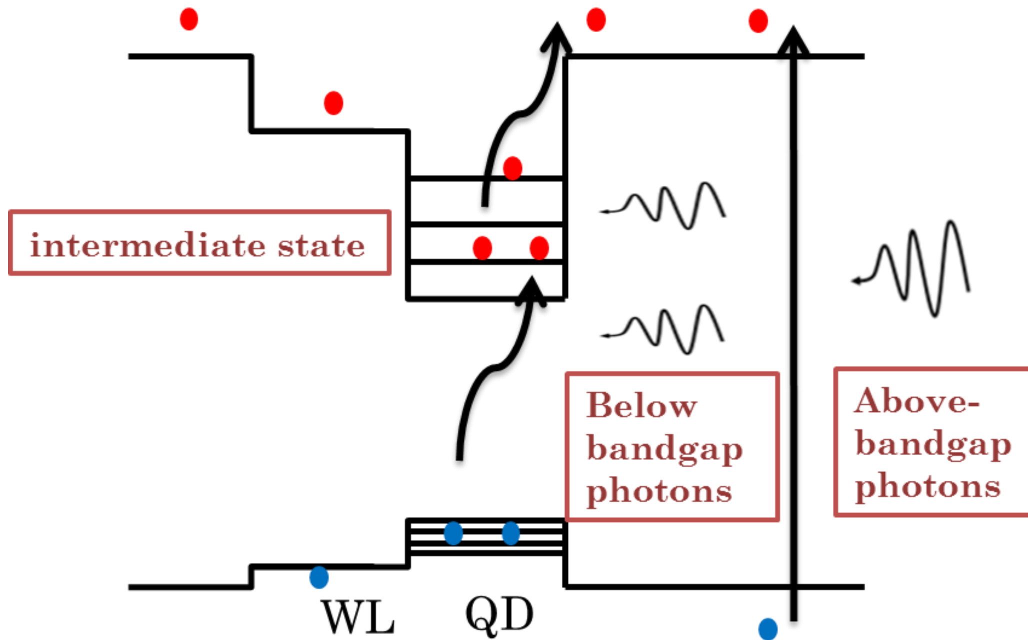

Figure 1-5: Utilizing QDs to facilitate below-bandgap photon absorption

The absorption of the second photon involves a transition from a bound (ground state of QD) to an unbound state in the conduction band. Since momentum should still be conserved, such a transition is possible only for small values of the momentum associated with the extended states in the conduction band. Since the electron in a quantum dot is bound over a potential of dimension of order 1- 10 nm, only wavevectors k of magnitude given by the uncertainty principle $\Delta x \times \Delta k \approx 1$ are allowed. This leads to optical wavelengths in the λ = 5 –

10 μm range, as typically required for absorption in quantum dot infrared photodetectors [13-15].

Beginning in the late 1990s and extending to today, a great deal of effort has been driven into experimental characterization of the QD-based IBSC realization. However, no experimental results show a higher efficiency of InAs/GaAs QDs device than a bulk GaAs device. Even though QDs device sometimes exhibits a slightly higher Jsc from enhanced below bandgap absorption, a degraded Voc is frequently observed. Unfortunately, there have been a lot of papers in the field that are either based on wrong assumptions or wrong interpretation of the experimental results. For example, the enhancement of Jsc has then been mistakenly attributed to the second transition where in fact there does not exist any second transition and the enhancement is just due to tailing absorption or fabrication error. People are also attributing a photoresponse to lower energy photon absorption by the second transition, simply overlooking the fact that the tail itself can facilitate below-bandgap absorption and keeping it in mind that a bound to unbound transition has a low transition probability.

Till now, a systematic study into the QDSC operation principle doesn't exist. The enhancement of the Jsc and degradation of Voc don't have any quantitative measure at all. Non-linear characterization and electron doping effects have never been clarified. The generation-recombination process has not been clearly studied.

1.3 Dissertation outline

In my Ph.D. work, uniform performance QD solar cells with high conversion efficiency (17.8% with Jsc=29.9 mA/cm^2) have been fabricated using carefully calibrated process recipes as the basis of all reliable experimental characterization. The development of a good process flow is very critical. In **Chapter 2**, I have described in great detail the different fabrication recipes and the rationale behind them in the hope that it can benefit future readers interested in III/V solar cell fabrication.

GaAs bulk device structure design and performance comparison with different bulk structures is presented in **Chapter 3** along with an introduction to the characterization systems we have set up in the lab. Solar device characterization is of critical importance since it sheds light on the semiconductor layers information, photon absorption process, carrier collection and transport process and its opto-electrical conversion process. In this work, external quantum efficiency measurements were performed as a measure of the below bandgap distribution of transition states. In particular, the below-bandgap photocurrent generation has been attributed to transitions via confined energy states and background continuum tailing states. Photoluminescence measurement is used to measure the energy level of the lowest available state and to indicate the background coupling between tailing states and quantum dot states. A basic I-V measurement reveals a degradation of open circuit voltage (Voc) of QD solar cells, which is related to the

one sub-bandgap photon absorption process followed by a direct collection of the generated carriers in the external circuit.

Chapter 4 is a discussion of the formation of an extended tailing density of states upon the incorporation of self-assembled QDs into the bulk GaAs device. It also contains an original and detailed discussion on the tail's effect on Jsc and Voc, two of the most important parameters describing a solar cell. The origin for the enhancement of the short circuit current density and degradation of open circuit voltage in QD solar cells has been carefully investigated. From this work, we found that the incorporation of self-assembled QDs interrupts the lattice periodicity and introduce a greatly broadened tailing density of states extending from the bandedge towards mid-gap. A below-bandgap density of states (DOS) model with an extended Urbach tail has been developed. The tailing states contribution to the overall Jsc have been distinguished from the QD and WL states from a fitting based on an exponential distribution of the tail. We have also derived the QD energy states based on a Gaussian lineshape fitting and derived an inhomogeneous broadening of 25 meV. In order to account for the effect of extended tailing states to the degradation of Voc in a quantum dot device, we have developed a modified Shockley-Queisser model. The experimental results are generally in agreement with theoretical values predicted by our model. The extended tailing density of states has been proven to be functioning as an efficient carrier relaxation and extraction pathway.

Besides a careful investigation of the one-photon process on the aspects of both enhancement of Jsc and degradation of Voc, with the availability of laser with on-resonance and off-resonance excitation energy, we have also explored the photocurrent enhancement by a sequential two-photon absorption (2PA) process via the intermediate states. The non-linear opto-electronic properties are of particular interest to the QD IBSC research, since the IB model involves a two-step photon absorption process. Our proposed experimental detail and results are described in **Chapter 5**. Our method has clearly distinguished the 2PA current generation with other nonlinearity including quantum dot saturation effect and local heating effect. The measured room temperature photon-response that is attributed to the second transition turned out to be due to a transition from an unbound state to an unbound state rather than from a quantum dot states to an unbound state transition. The extended tailing density of states has shown to be coupled to the QD states and has proven to be largely responsible for the observed second photon absorption. For the QD bound states to continuum transition, it is shown to be negligible at room temperature. The QD state to conduction band transition is too small to be able to produce a matching carrier flow from the QD state to the conduction band with that from the valance band to the QD states. It is fundamentally impossible to realize with the intermediate band model utilizing the self-assembled QDs.

Whenever an energy state can facilitate additional absorption, it can facilitate recombination as well. And if the recombination is non-radiative, it can be

detrimental to solar cell performance. Through a careful investigation, we found that QDs can indeed function as multi-electron traps. By a comparison with quantum dots of different electron-doping levels, we conclude that electron doping can exert a repulsive Coulomb force to the mobile electrons so that the electrons will tend to circumvent the dots and get collected at the electrodes. A larger Jsc has been measured for a 4e/dot device compared with an 0e/dot device. In the meantime, electron doping will decrease the direct transition from the valance band to the QD states as shown in our high resolution EQE results. The corresponding discussion appears in **Chapter 6**.

Based on the understanding and the characterization results we have achieved, we summarize our key findings in **Chapter 7.**

2 An overview of GaAs fabrication techniques and the process flow of GaAs solar cell fabrication

This chapter summarizes the process techniques and the developed fabrication recipe for GaAs based solar cell. A great deal of detail is put into important process steps such as cleaning, etching, metal contact, passivation and so on. At last, a complete process flow is presented along with the rationale behind each step.

2.1 Cleaning

It is *vital* to properly clean the surface of a semiconductor. Before some critical steps such as etching, metal deposition and annealing, the surface of GaAs must be handled carefully to make sure that it is 1) free of both organic and inorganic contamination, 2) has a surface oxide layer as thin as possible and 3) retains a proper Ga to As atomic ratio.

The surface of the GaAs wafer can be contaminated by organic grease very easily. Even by exposing the wafer to air for a moderate amount of time, the organic vapor in cleanroom can re-deposit on the surface of the wafer and therefore prevent proper formation of Ohmic contacts. Touching the wafer with

bare hands should never be allowed because the complete removal of the finger grease is extremely difficult. After the growth, wafer handling and process steps can contaminate the wafer with inorganic impurities.

An organic solvent cleaning protocol needs to be applied to degrease the wafer. The proper cleaning should consist of the following steps: 1) immerse the wafer in boiling acetone for 10 min, 2) immerse the wafer in boiling methanol for 10 min, 3) immerse the wafer in boiling isopropanol for 10 min. Solvents, especially acetone, evaporate very fast. It is important to cover the container while boiling. The re-deposition of the grease to the wafer after all solvent evaporates becomes much harder to remove. If there is still residual grease after these steps, take the container with the wafer for ultra-sonic cleaning. Potential heating of solvent while in ultra-sonic equipment is desired since it can effectively clean the surface with a minimum amount of vibration.

Following such steps of solvent cleaning is a set of inorganic cleaning protocol which consists of the following steps: 1) rinse the wafer in $HCl:H_2O=1:10$ for 30 s, 2) rinse the wafer in DI water for 30 s, 3) rinse the wafer in $NH_4OH:H_2O=1:10$ for 30 s, 4) rinse the wafer in DI water for 30 s, 5) blow try with Nitrogen flow. A rinse in $NH_4OH:H_2O=1:10$ removes the native oxide and metallic impurities. After the wafer is grown, a native oxide layer of the order to 1 nm should be expected. Note that a rinse in $HCl:H_20=1:10$ could result in an As-rich surface. The NH_4OH solution generally could restore a more nearly

stoichiometric surface by removing excess As atoms. The solution needs to be diluted so that it won't etch into GaAs at the cleaning stage. Experimentally, an oxide-free GaAs surface is hydrophobic. This can be directly observed after cleaning the wafer. It is worth noticing here that the main difference between a cleaning and etching process is that during etching, an oxidization agent is added. In the case of the NH_4OH etching recipe, H_2O_2 is added.

2.2 Etching

Device patterning is mainly achieved by etching. There are two main etching methods—dry etching and wet etching. "Dry" by definition is to use gas-phase processes while "wet" is to use solution-based etchant.

In order to evaluate the effectiveness of the etching process, we need to consider five characteristics: *etching rate, profiles, selectivity, uniformity, resulting surface damage*. The table below summarized the pros and cons for dry and wet etching. Generally speaking, chemical reaction provides high selectivity, well-controlled rate with lower damage. While the ion bombardment during dry etching yields better uniformity and well-defined vertical etch walls, sometimes in order to obtain the desirable etching results, a combination of chemical and physical etching process is used. A good example would be the GaN ohmic contact optimization project I have done in my first year. In order to obtain a uniform, well-defined, yet smooth surface, I have used dry etching first to define the structure and then used wet etching to smooth out the etched surface. Wet

etchant attacks dangling bonds and etching pits so that a much smoother surface can be achieved.

Table 2-1: Comparison between dry etching and wet etching

	Dry etching	Wet etching
Profile control	Excellent	Dependent on crystal orientation
Selectivity	Low	High
Uniformity	High	Low
Surface damage	High	Low
Reproducibility	High	Sensitive to solution conditions such as PH value and Temperature
Ease to use	Complex equipment, limited number of available gas	Inexpensive, easy and abundance of available chemicals

2.2.1 Dry etching and its application to our process

We have used Fluorine-Induced Coupled Plasma (F-ICP) from Oxford to define the Si_3N_4 hard mask and Chlorine-Induce Coupled Plasma (Cl-ICP) for the sequential etching into the GaAs. ICP provides separate RF and ICP generators to control the ion energy and ion density which enables high process flexibility. The power of plasma can be tuned to a relatively high value where there is negligible bombardment with high energy ions where the wafer temperature might be elevated. In the plasma etching mode, the device will sit in the generated plasma without applied RF power so that there are few ions with high energy that will strike the GaAs surface. The RF power controls the powered electrode underneath the device. It provides energetic ion bombardment for the purpose of profile control. Thus a good combination of the ICP and RF power is needed to achieve a vertical etch profile while maintaining a smooth surface. In my experience, we have used BCl_3/Cl_2 mixtures because it tends to produce smoother surfaces than Cl_2 only plasmas.

Dry etching is much more desirable than wet etching in defining mesa area. Wet etching will create a tilted mesa wall that depends on the crystal orientation. The Figure below shows the top view of the mesa side wall with wet and dry etching respectively. As can be seen, there is a visible slope from the wet etching method while the dry etching has produced a very good vertical wall.

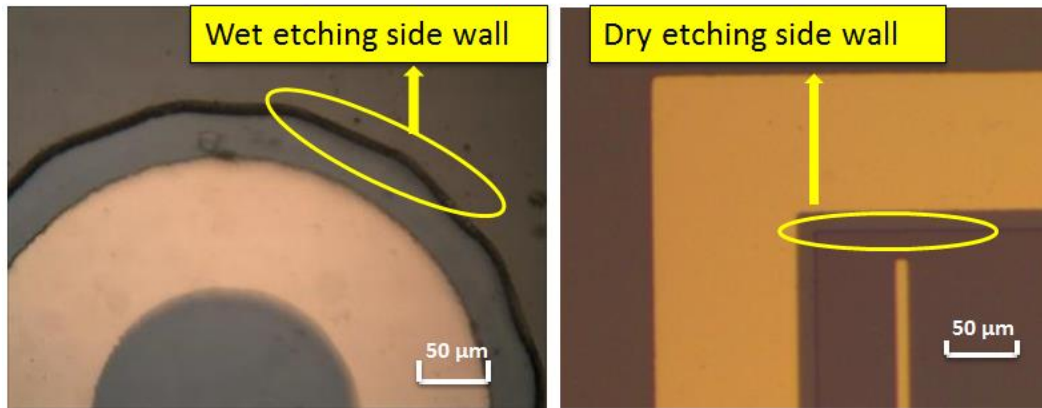

Figure 2-1: (a) A GaAs device that is etched by wet etching method. (b) A GaAs device that is etched by dry etching method. The scale bar is the same in both devices. As can be seen, the sidewall after wet etching is much thicker than that after dry etching process. The etch profiles largely depends on crystal orientation after wet etching while dry etching process is more isotropic.

While dry etching is preferred over wet etching for its better profile control and etching uniformity, it could seriously degrade the electronic properties of the surface by forming a large density of surface defect states, creating dangling bonds, and changing the surface stoichiometry which changes the Fermi level pinning position or even surface doping type. For very small etched devices as in our case where the typical device dimension is (300 to 500 μm)^2, the sidewall area is an important feature of the device. Ion induced damage of sidewalls becomes very important. This is reason why the surface passivation is required after the fabrication of the device.

2.2.2 Wet etching and its application to our process

Wet etching provides a better surface because it is free of physical bombardment. Thus it is preferred when surface quality needs to be preserved. In our devices, the top layer of GaAs is generally 20 nm to 50 nm. Due to the high absorption coefficient, a large amount of high energy photons are absorbed within the top layer region before they reach into the active region (the active region includes the depletion region and the electron & hole diffusion region). An $Al_{0.8}Ga_{0.2}As$ window layer is beneath the GaAs top contact layer. Selective etching can't be used here since $Al_{0.8}Ga_{0.2}As$ will oxidize quickly once exposed to air. The only feasible way is to thin down the top layer to about 5 nm. We have used citric acid etchant with an etching rate or 5 nm/min. The solution is prepared fresh every time for a uniform etching rate. After etching, the performance of the device has been enhanced in both Jsc and Voc.

Below is the performance comparison before and after top layer thinning for structure M1161. As can be seen, the Voc has increased from 0.84 V to 0.91 V and the Jsc has increased from 20.2 mA/cm^2 to 23.2 mA/cm^2. The fill factor has increased from 60.67% to 79.38%. It might be possible that the slow etching recipe has also unintentionally saturated and smoothed out the top surface and the etched side wall. To conclude, the effect of the slow etching here is as least two-fold: 1) it thins down the top contact layer so that more photons can reach the active region and 2) it can help with surface and mesa wall treatment.

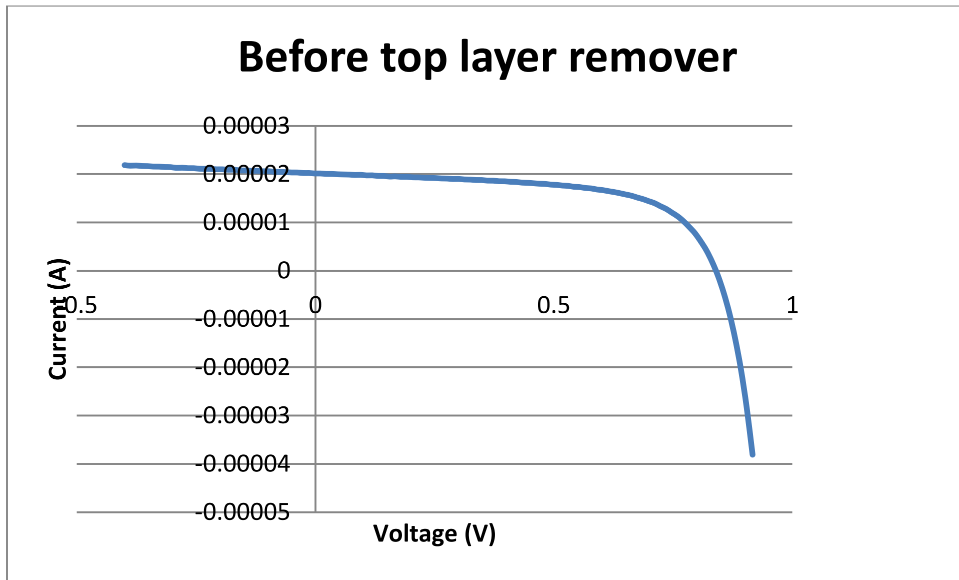

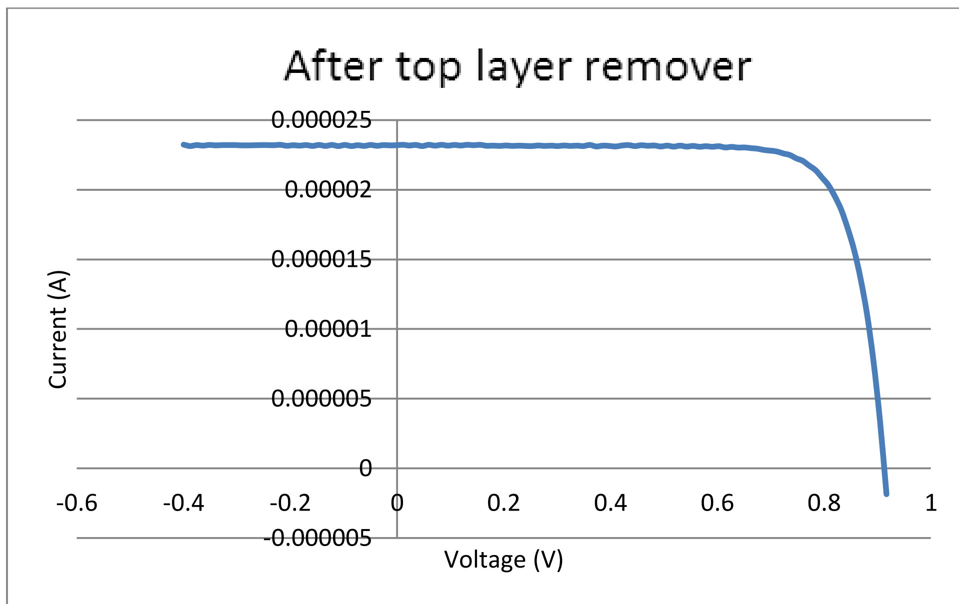

Figure 2-2: Bulk GaAs solar cell IV performance before and after citric acid treatment. The Voc has increased from 0.84 V to 0.91 V and the Jsc has increased from 20.2 mA/cm^2 to 23.2 mA/cm^2.

Table 2-2: Summary of the key parameters of the cell before and after removing top layer

M1161	Voc (V)	Jsc (mA/cm^2)	Fill Factor (%)	Efficiency (%)
Before removing top layer	0.84	20.18	60.67	10.28
After removing top layer	0.91	23.18	79.38	16.79

2.3 Electrode contacts

2.3.1 Electrode formation

The lift-off method is commonly used to make a metallic pattern on a semiconductor. The general steps are as follows: 1) A pattern is defined on a substrate using photoresist. 2) Uniformly deposit a metallic film, covering the photoresist and areas in which the photoresist has been cleared. 3) Immerse the device in acetone. The photoresist under the film is removed with solvent, and leaving only the electrode pattern itself.

In order to achieve a good lift-off film, there are several things that are worth noting: 1) Semiconductor surface cleanness is critical; 2) A good undercut profile is necessary (with a negative slope created by negative PR); 3) the temperature

during metal deposition needs to be controlled to remain the gel-like property of photoresist.

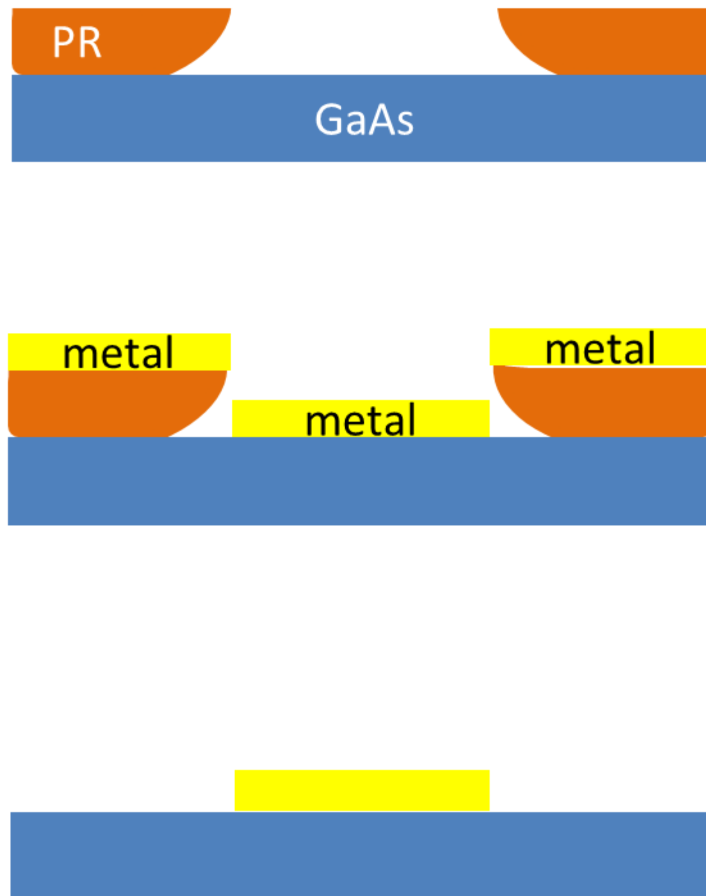

Figure 2-3: Illustration of lift-off method for electrode deposition

P-type electrode Ti/Pt/Au is quite standard. As the first deposited layer, Ti is for adhesion purpose. Pt is to provide a large work function to form an Ohmic

contact with p-type GaAs. The last layer of Au needs to be at least 100 nm for the gold wire-bonding process.

Au/Ge/Ni/Au 5/30/20/100 nm has been used for n-type GaAs. The Au and Ge thickness ratio is chosen so that the resulting alloy is near eutectic composition. Then during a rapid thermal annealing process, Au and Ge can melt as the eutectic temperature of the alloy is reached (361 ℃). The Ni layer is to provide the right work function. The last layer of Au is to provide a layer for the bonding and packaging purpose.

2.3.2 The electrode contact characterization

An Ohmic contact is to provide a linear relationship between current and applied voltage. If the contact is a Schottky contact due to mismatch of the metal's work function and the semiconductor's Fermi level position, it creates another non-linear electronic component that could seriously affect the shape of the IV curve.

Given an Ohmic contact, the optimization of the contact resistance is vital. Low contact resistances for both electrodes are highly desirable. For a highly doped thin film solar cell, the resistance of the device itself is generally very low. Consequently, the parasite series resistant is dominated by the contact resistance. A high contact resistance can reduce both the fill factor and the open circuit voltage. It might also rise the device temperature when operating under high concentration factor. We have used the circular Transmission Line Method

(cTLM) to evaluate the effectiveness of the procedure to realize Ohmic contact formation (Figure 2-4).

CTLM Patterns

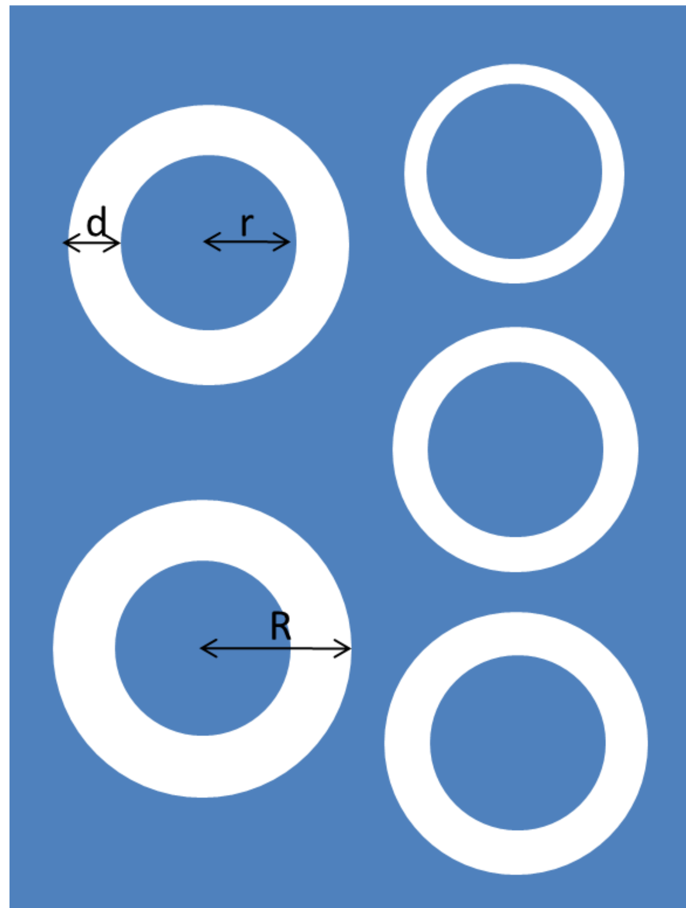

Figure 2-4: Pattern of cTLM for characterization of contact resistance

We now list the steps required for obtaining a good contact resistance between a semiconductor and its electrode:

1. The semiconductor surface has firstly been cleaned. Then we use the lift-off method to deposit a cTLM pattern with the electrode material. The pattern that

we have designed has an r=200 μm, with d=8 μm, 14 μm, 20 μm, 30 μm and 50 μm respectively (Figure 2-4).

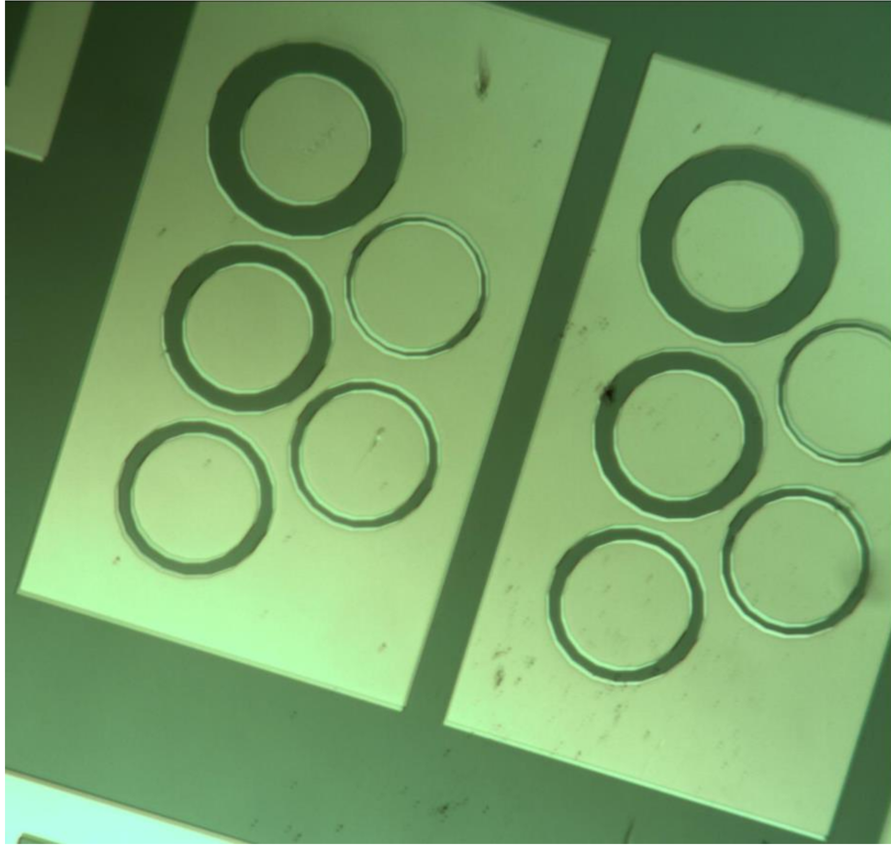

Figure 2-5: Fabricated cTLM pattern image under optical microscope

2. Measure the resistance Rt between each center circle and the outer surrounding. Now we have the value of Rt for d = 8 μm, 14 μm, 20 μm, 30 μm and 50 μm respectively.
3. Plot Rt vs In((d+r)/r). Extract the slope of the curve. The slope is the sheet resistance Rsh/(2π). Thus Rsh can be obtained.
4. Then take the value of the Y-intercept, which is Rsh × Lt/(rπ) where Lt is the transfer length that can be expressed as $(\rho_c/Rsh)^{1/2}$. ρ_c is the contact resistance.

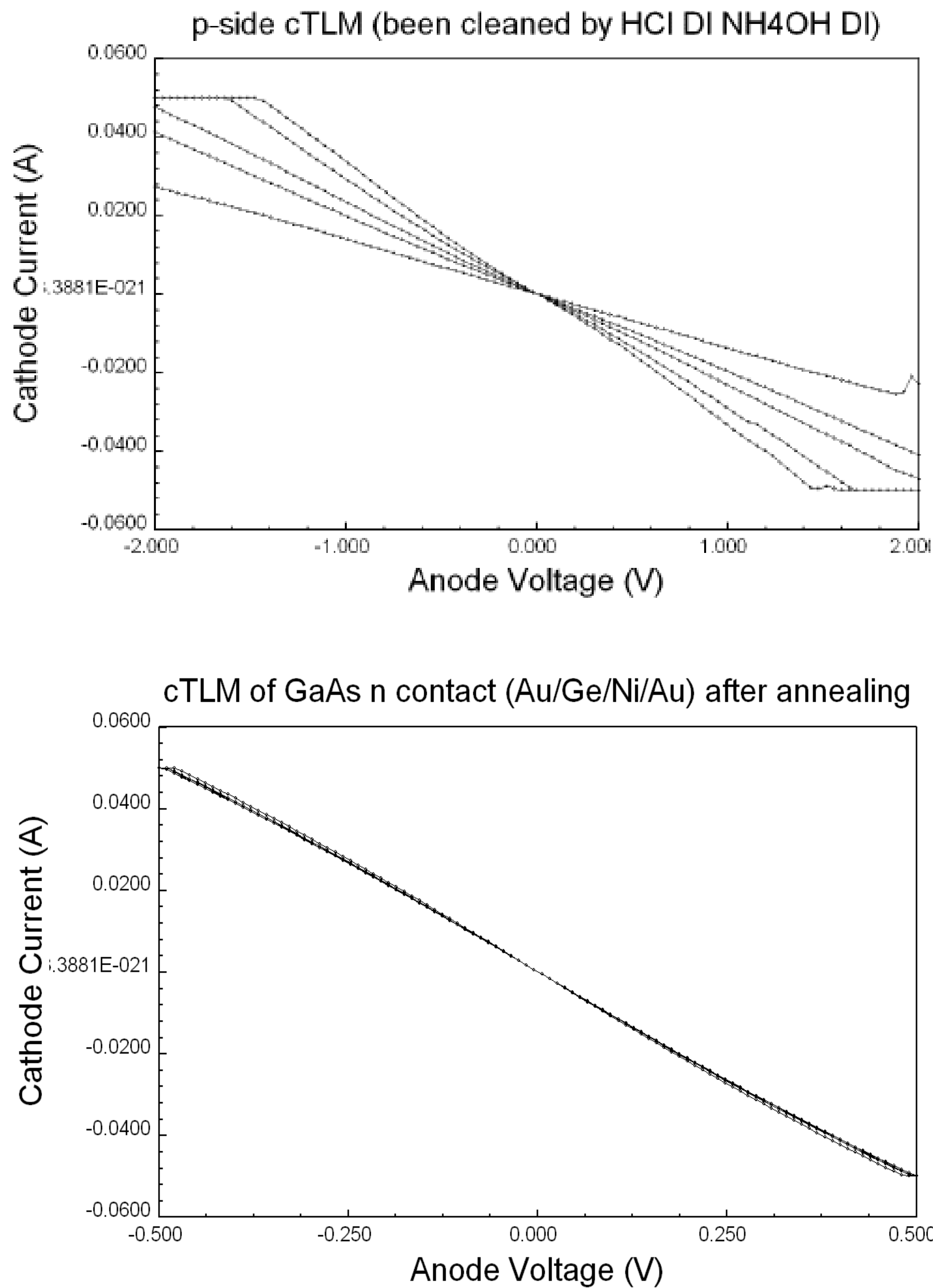

Figure 2-6: Measured IV curves with difference value of ***d*** in a cTLM pattern for n and p GaAs contact layer with a doping density of 3e18 $cm^{-3}$and 5e18 cm^{-3} respectively for the extraction of the contact resistance and the sheet resistance.

By using this method on n and p-electrodes for GaAs, we have obtained the plot of Rt vs d shown in Figure 2-6. The extracted sheet resistant Rsh and contact resistance ρ_c is summarized in Table 2-3.

Table 2-3: Contact resistant evaluation of n- and p- electrodes using cTLM

	METAL TYPE	ρ_c ($\Omega\cdot cm^2$)
N-TYPE	Au/Ge/Ni/Au	0.0114
P-TYPE	Ti/Pt/Au	0.00054

2.3.3 Schottky contacts and barrier height extraction

A Schottky contact is used to describe a metal/semiconductor interface that has a non-linear diode-like current-voltage behavior. The primary parameter of a Schottky barrier is the barrier height $\Phi_{B,}$ which is the difference of the metal-vacuum work function and the semiconductor-vacuum electron affinity. The formation of the Schottky barrier is shown here.

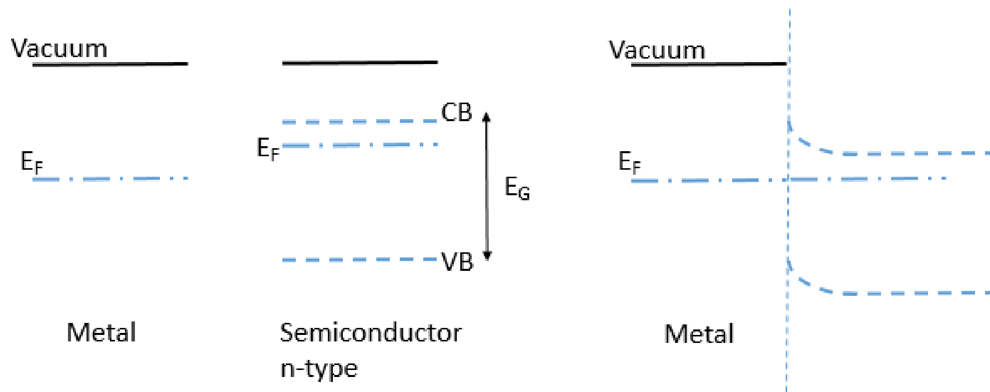

Figure 2-7: Illustration of the formation of Schottky barrier (web resource)

A depletion region will form due to the Schottky barrier, which yields variant resistance under different bias. Thus, the Schottky contact gives a non-linear rectifying characteristic. If the electrode contact is Schottky type, it will function as a back-to-back diode in series with the semiconductor pn junction. We need to avoid this for realizing semiconductor solar cells. However, the measured IV curve of a Schottky barrier can give very important information on the position of the Fermi level of the semiconductor and the work function of the contact metal. Here we show an example where we use the IV characteristics to extract the barrier height between AZO and perovskite. AZO exhibits a work function ranging from 3.6 eV to 4.0 eV depending on the growth condition. A fitting to the barrier IV curve can be used to estimate the work function of fabricated AZO.

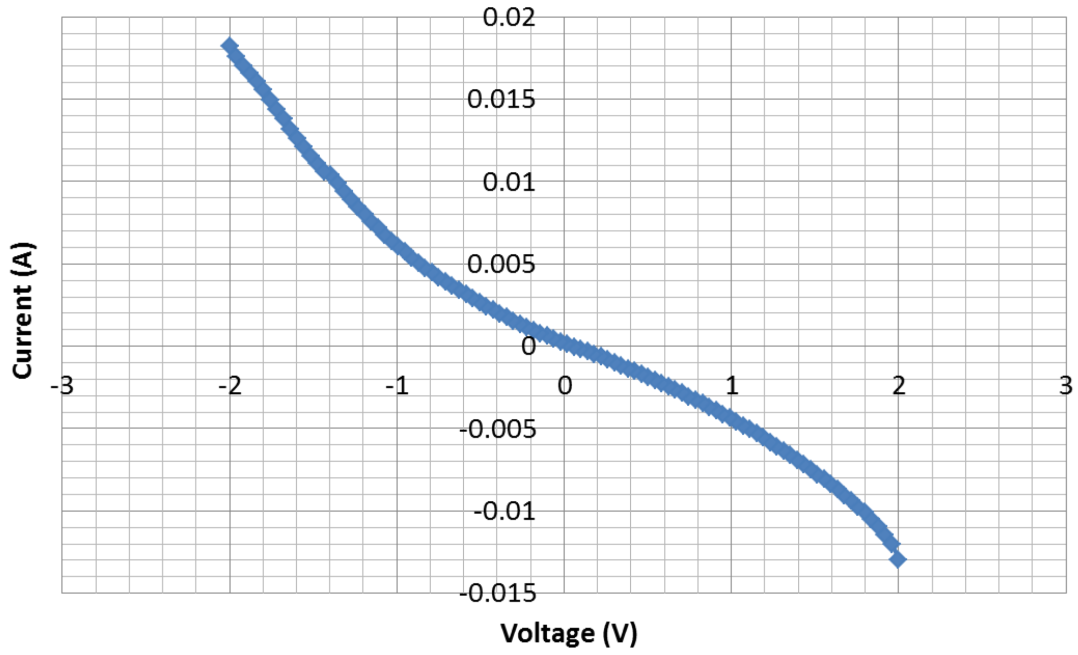

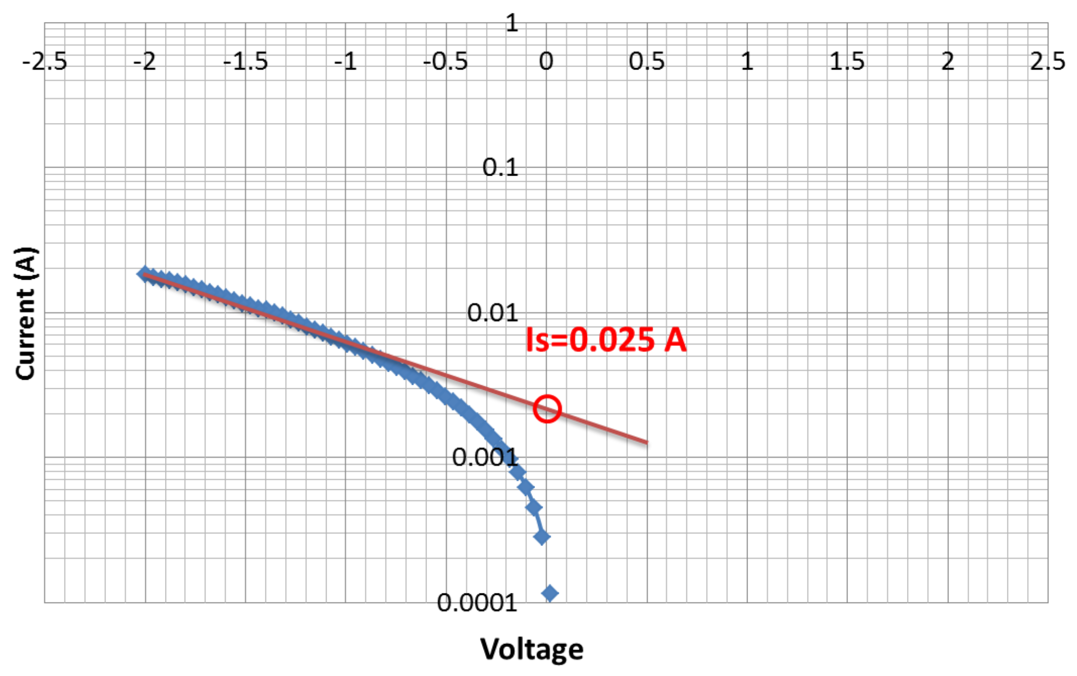

Figure 2-8: Example of a Schottky barrier. (a) IV plot of AZO/perovskite contact and (b) the semi-log plot to extract parameter *Is*.

Barrier height ϕ_B can be expressed as follows:

$$\phi_B = kT/q \times \ln(A \times B \times T^2/Is)$$

where A is the area of the contact, B is a parameter that depends on the material itself. T=300K, Is is extracted from the IV characteristics. According to Figure 2-8, Is is extracted to be 0.025 A. The most uncertain of the parameters here is B, rendering this method only as accurate as the knowledge of B. Fortunately, B appears in the "ln" term so the error is small. The equation can be rewritten as 0.39 eV + $0.026 \times \ln(B)$. A typical value of B will be around 10 A/cm^2K^2. The barrier height can thus be derived.

2.4 Passivation

GaAs typically has a high surface recombination velocity for especially high energy photons. The extremely high density of surface states will effectively pin the Fermi level at the interface and profoundly alter the band diagram at the surface. A certain degree of band bending should be expected for doped GaAs layer. Therefore, it will produce a surface electric field which will drive carriers from the surface and will form a depletion region. For example, for a n-doped GaAs bulk layer with a doping level of 10^{17} cm^3. The surface states roughly pin the Fermi level at the mid gap.

Upon illumination, photons with energy higher than the bandgap energy will be absorbed and produce carriers. GaAs has an extremely high absorption coefficient. The carriers generated will follow an exponentially decaying density profile extending into the bulk material, as shown as

$$\text{Carrier density} = A \times I_0 \times e^{-At}$$

Where I_0 is the incident light intensity, t is the thickness and A is the absorption coefficient. As can be seen, the light generated carriers have the highest concentration at the surface. Since the surface states are mostly centered at the mid-gap, they can very effectively trap both carriers and mediate non-radiative recombination. These surface mid-gap states can be more deleterious to higher energy photons due to an even higher absorption coefficient. Nevertheless, the aforementioned surface electric field due to surface Fermi level pinning will assist the surface recombination process by sweeping minority carriers towards the surface.

Thus, the importance of passivation is self-evident. “Passivation” by definition is to passivate the surface recombination effect by deactivating the defects through reaction to reduce the density of surface states.

Sulfur has been used most commonly mainly due to two reasons: 1. S can bond with Ga and As and it will prevent further surface oxidation process, 2. A Sulphided surface has shown much less surface states. The Ga-S bonds create states outside of the forbidden band while the As-S bonds create states close to the

conduction band that basically function as electron dopant that can be easily thermalizied. Ammonium sulphide is most commonly used to passivate the GaAs surface. Before immersing the device into Ammonium sulphide solution, I generally would use diluted HCl solution to remove the native oxide layer first so that the subsequent reaction of Ga and As atoms with sulpur can more readily happen. 15 min immersion into $(NH_4)_2S$ solution under room temperature is enough. To increase the effectiveness, additional S powder is added into the solution to make $(NH_4)_2Sx$ solution. A sequential immersion for 15 min in DI water can help to take away excess sulfur to avoid possible shunting (the excess sulfur will accumulate at the side wall and provide a current leakage path). After passivation, an immediate encapsulation of Si_3N_4 is desired for the long-term protection since the Sulfur can evaporate within a short period of time. The effect of Si_3N_4 thin film is three-fold: 1) Si_3N_4 encapsulates Sulfur to keep it from evaporating, 2) Si_3N_4 is a good diffusion barrier and it is inert to many chemical reaction, 3) Si_3N_4 has a dielectric constant between air and GaAs so it can function as Anti-Reflection layer to the GaAs solar cell.

We show with experimentally measured IV characteristics in a GaAs bulk solar cell (M1215) the effect of passivation on the cell's performance. As can be seen, the value of Voc has increased from 0.92 V to 0.94 V while the Jsc has increased from 20.4 mA/cm^2 to 22.9 mA/cm^2. The blue curve is from an experimental fitting based on a two-diode model (please refer to Chapter 4.2 for a detailed description of two diode model). The fitted curve perfectly overlaps with

the experimentally measured data. A look into the change of the dark saturation current J_{01} and J_{01} indicates a much lower surface and sidewall recombination rate.

Table 2-4 Summary of the performance before/after passivation

	Voc (V)	Jsc (mA/cm^2)	FF	**J_{01} (mA/cm^2)**	**J_{02} (mA/cm^2)**
Before passivation	0.92	20.4	80.3%	**3.5e-15**	**7.5e-7**
After passivation	0.94	22.9	81.4%	**6.9e-16**	**5e-7**

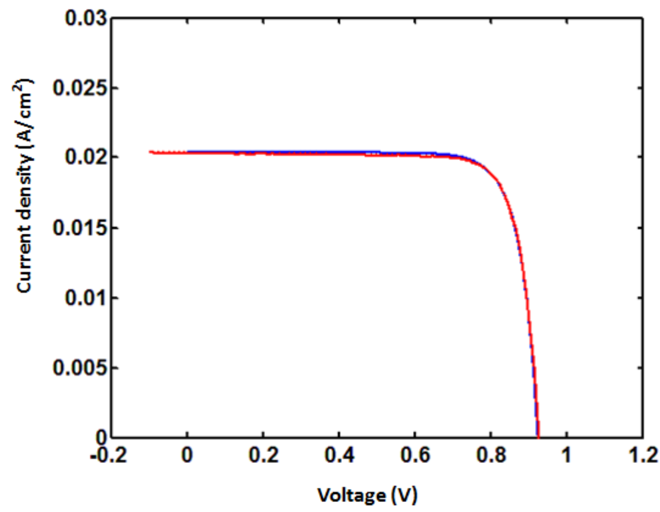

(a) Before passivation

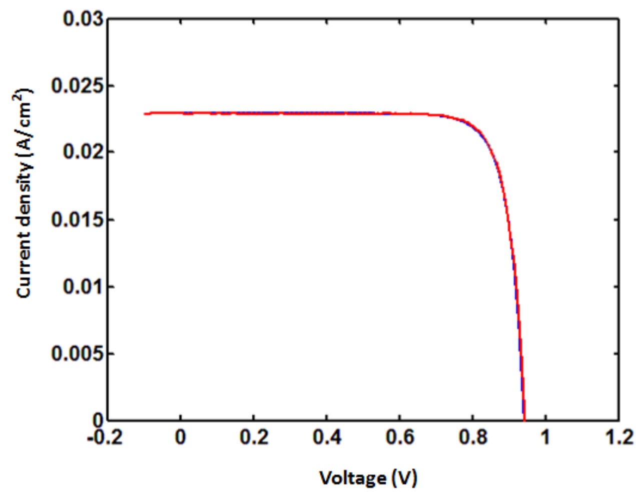

(b) After passivation

Figure 2-9: After passivation, the value of Voc has increased from 0.92 V to 0.94 V while the Jsc has increased from 20.4 mA/cm^2 to 22.9 mA/cm^2. The red curve is the measured data while the blue curve is from an experimental fit based on the two-diode model.

2.5 Device thinning down

There has been great progress in the solar cell efficiency due to the recognition of the need to increase photon travelling path by surface texturing. GaAs has been the center of study as one of the most promising high efficiency (~28%, close to its Shockley-Queisser limit) thin film material systems. For such solar cells with a high absorption coefficient, the active region for light absorption is generally of the order of several micrometers only. Only the top 3 μm thick GaAs layer is responsible for the light-electricity conversion. The hundreds of micrometers of GaAs substrate are very expensive and will greatly raise the overall dollars-per-watt value of the cell. In order to reduce the material cost, the active layer will generally be transferred to a much less expensive substrate followed by an epitaxial lift-off process. By this way, the GaAs substrate can be reused for the growth process several times.

In this section, we have described our efforts in device thinning down for thin, flexible and light weight application. There are two main approaches for realizing this: active layer lift off and backside substrate etching.

2.5.1 Lift-off

The bulk GaAs solar cell M1091 has been chosen for lift-off practice. M1091 has both a top and a bottom window layer. We have used the bottom window layer

($Al_{0.8}Ga_{0.2}As$ 100 nm) to serve as the sacrificial layer for lift-off purpose. The steps are as follows:

1. Pattern the device with top p-type electrode Ti/Pt/Au.
2. Use ICP to define the area for lift-off. Etch into the device to just **above** the bottom sacrificial layer.
3. Protect the front window layer so that it won't be affected during lift-off process using black wax, as shown in the figure below. Black wax is used because it can provide a tensile strain on the active film during etching so that it can help peel off the film from the substrate.
4. Make 10% HF solution. Immerse the device in the solution for 48 hours. In order to speed the peeling off process, the device has been immersed into DI water with ultra-sonic vibration. The device is then detached from the substrate.
5. Deposit n-type electrode Au/Ge/Ni/Au on the backside of the device.
6. Immerse the fabricated device with protecting wax into acetone to dissolve the wax carefully. Keep the device inside the solvent, pull out the old solution and fill in the fresh one until the dissolved wax is gone completely.
7. Attach the device to a thin glass slide while immersed in solution and carefully pull it out. The device is shown in Figure 2-10. The total thickness is only 2 μm. As can be seen, the edge area has been curved up.

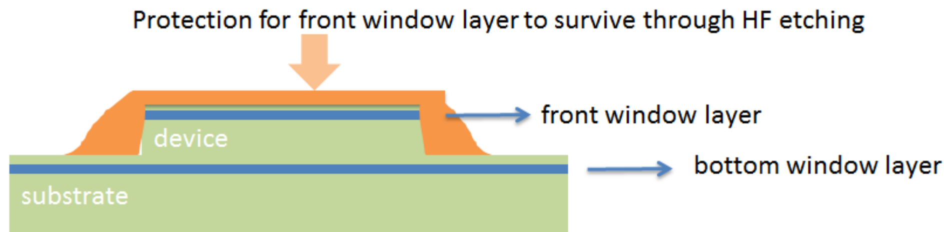

Figure 2-10. Lift-off device (device that has been lifted off from GaAs substrate with a thickness of 2 μm and e-beam deposited top and backside electrodes)

2.5.2 Backside thinning

The structure M1091 has been used for backside thinning down practice. The bottom window layer $Al_{0.8}Ga_{0.2}As$ has been used as etch stop layer.

1. Apply device upside down and wax it to a polishing stage. Use mechanical polishing for the back surface. Thin down the device to 100 to 200 μm. Take the device off and clean it properly.

2. Apply SU8 as protection to the backside and fix the device upside down to a microscope glass slide. Observe from the glass side to make sure there is no bubble in between the device and the substrate glass.
3. Bake it for 10 min at 90 ℃.
4. 1 min exposure under mask aligner 365 nm UV light.
5. Mix $NH_4OH:H_2O_2$ = 1:3 for a fast etching rate (etch rate 10 μm/min) and immerse the device in the solution for 1 hour until the device is reasonably thin. The etching solution needs to be stirred constantly.
6. Mix $NH_4OH:H_2O_2$ = 1:30 for a max selectivity between GaAs and AlGaAs. Immerse the device in the solution for 40 min until the etch stops when it reaches AlGaAs layer. The etching solution needs to be stirred constantly.
7. Dissolve SU8 in acetone.

The resulting etched device could be very fragile and subject to cracking easily. For thin and flexible application, the thinned down device will then be transferred to an inexpensive and flexible substrate.

2.6 The developed process flow for GaAs solar cell fabrication

This developed recipe for our GaAs device fabrication is based on my own experiences during fabrication and the equipment's condition. The condition of equipments in Fablab can change all the time. <u>Please always run a calibration run prior to important steps.</u>

The detailed process recipe is described in the following paragraph:

1. After a proper three-step cleaning of the wafer, flip it upside down; use diluted NH_4OH ($NH_4OH:H_2O$=1:10) solution to create a fresh backside surface. The pre-clean step is critical for achieving low electrical resistance in the contact. After cleaning, load the wafer into the metal deposition chamber immediately to avoid further oxidation. Deposit Au/Ge/Ni/Au = 5/30/20/100 nm under a chamber pressure smaller than 5×10^{-6} Torr. The deposition should be followed immediately by a rapid thermal annealing. Load the sample and run Nitrogen into the chamber for 10 min to purge out residual air/oxygen. Anneal the sample in Nitrogen gas for 1 min at 400 ℃. The deposition of the backside electrode should be the first step before patterning the mesa area and depositing the p-type electrode.
2. Use PECVD to deposit a 500 nm standard Si_3N_4 film on the top of the wafer. Run a pre-run to ensure that the set temperature is as desired.
3. Pattern the wafer with photoresist for the mesa areas. Follow standard AZ5214 PR patterning recipe.
4. Use Fluorine-based ICP etcher with SF_6 gas to etch into Si_3N_4 hard mask. Fluorine based ICP is generally used for dielectric materials such as SiO_2 and Si_3N_4. Adjust the etching time based on the etching rate and aim for a little bit over-etch. If etching rate is uncertain, run an etching rate calibration with bulk GaAs wafer. Apply the heat conducting oil to the backside of the wafer or else

photoresist can be burned. Run a pre-run for chamber cleanness and to ensure stable etching temperature. The recipe requires a running temperature of 5 degree. Without any pre-run, the processing temperature could be between room temperature and 5 ℃, which might leads to the burning of PR. Once the PR gets burned, it changes from gel-like to powder-like properties, thus definitely losing the masking function. The burned PR is also difficult to remove completely.

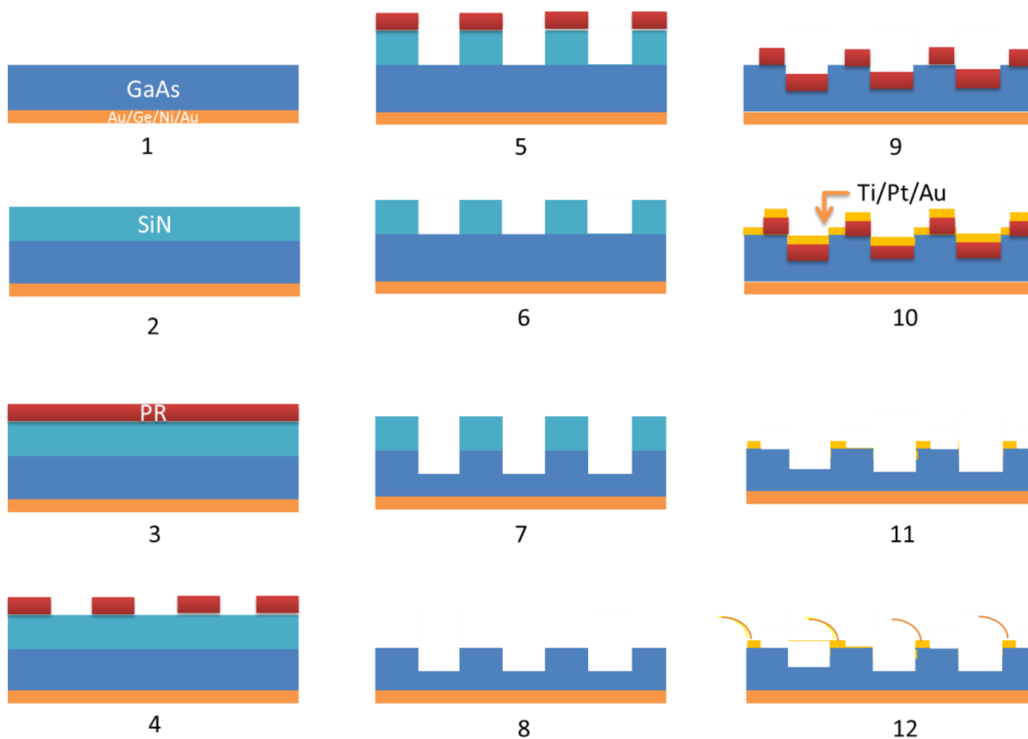

Figure 2-11: Illustration of the process flow of GaAs device.

5. After Si_3N_4 etching, clean the residual PR on the device. The surface needs to be absolutely clean since any residual PR would affect the following Chlorine-ICP etching into GaAs. I generally use an ultra-sonic cleaning in

Acetone for one minute. Heat the solution up if needed. Use optical Microscopes to inspect the surface cleanliness before proceeding to the next step.

6. Load the sample into chlorine-based ICP etcher. It is used primarily to etch III-V materials. Run a pre-run to ensure chamber cleanness and the consistency of etching rate. For each device structure, make sure that the resulting etched depth is slightly deeper than the active region so that each device is electrically isolated and also exposed to ion bombardment for a minimum time. Cl-ICP etches into Si_3N_4 mask as well with a relatively slow etching rate. A pre-run to calibrate the Si_3N_4 etching rate in Cl-ICP is preferred before this step. The Si_3N_4 mask needs to be thick enough to last through the etching process and protect the top P-GaAs layer.
7. Use F-ICP etcher to remove the residual Si_3N_4. After this step, the mesa area of each device is defined.
8. Pattern the top mesa area with reversed PR for the following lift-off process. After the PR patterning, rinse the device in NH_4OH:DI water=1:10 for 30 seconds and then rinse in DI water for 30 second. This makes sure that the open area (the area for the electrode to attach) is clean and free of organic residue. Diluted NH_4OH is perfect to remove a thin layer of organic grease on GaAs material. Without this step, during wire-bonding, the gold wire would pull the contact area off the device because of the bad adhesion between deposited metal and GaAs surface.

9. Load the device into the e-beam deposition chamber immediately after patterning to avoid further surface oxidation. Deposit Ti/Pt/Au = 30/80/100 nm for p-type electrode. Make sure the chamber pressure is as low as of order 10^{-7} Torr. Keep substrate shutter shut and heat up Ti crucible. Ti will bond with Oxygen in the chamber and attach onto the chamber wall. The chamber pressure will increase due to heating and then start decreasing at a certain point. Then it is time to open the shutter and start deposition.
10. Lift off process. Immerse the device into acetone. If the PR had been properly and freshly patterned before loading into the chamber, the lift-off process should be fairly easy. The pattern will show immediately. If the PR doesn't get off especially in some small feature patterns, immerse the device into heated acetone with ultra-sonic cleaning.
11. Wire bonding. Please refer to the manual of the wire bonder and adjust to the proper power for the first and second contact point. The second one needs a higher power so that the wire would break there. Use a Voltmeter to check the connection. An open circuit voltage of bulk GaAs solar cell under ambient light of each device is around 0.5 V.

3 Major characterization techniques and bulk GaAs solar cell characterization

3.1 Solar cell parameters and major characterization methods

3.1.1 Current-voltage characterization

A semiconductor PN/PIN junction is the most common form of a solar cell. In the dark condition, a semiconductor junction exhibits a typical diode curve. A very small amount of current flows from n side to p side under reverse bias. The junction reaches an equilibrium condition with zero bias. When the biasing voltage is increased to positive values, the current increases exponentially until it is limited by the series resistant in the circuit.

Light-generated current flows in the opposite direction of the diode current. Assuming no light assisted change in the solar cell's radiative/non-radiative recombination rates, a cell's IV curve under illumination is simply a constant Jsc which is added to the dark IV curve. The equation can be expressed as:

$$J = J_0 \left[\exp\left(\frac{qV}{nkT}\right) - 1 \right] - J_{sc} \qquad 3.1$$

Besides Jsc, some other very important parameters that have been used to characterize the performance of solar cells can also been determined from the light IV curve such as the open-circuit voltage (Voc), the fill factor (FF) and the overall conversion efficiency (Ƞ). Under a relatively higher positive bias, the IV

curve starts to show a linear relationship. It is because the current is now restricted by the series resistance, which can be estimated as 1/ (slope at high positive bias region). For a good solar device with few leakage paths, the cell should exhibit an almost flat region around zero bias. The shunt resistance of the device can be estimated by 1/ (the slope around zero bias region).

We use the solar simulator from Newport in the Fablab for measuring the light IV characteristics. An Air Mass Global 1.5 filter is used for matching the light source with the solar spectrum.

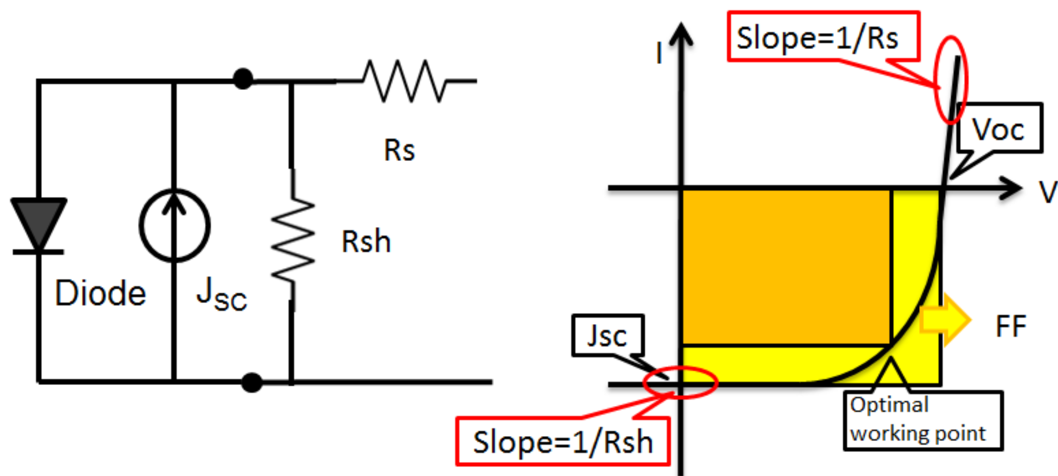

Figure 3-1: Simplified solar cell diode model

For the dark measurement, besides turning off all the ambient light when measuring, proper device shielding is required. The device needs to be enclosed in a metal box to shield the signal from E&M noise. The n-base of the device is connected with the metal box while the metal box is properly grounded. The reverse dark saturation current can be extracted experimentally from the dark IV

data. Sometimes light-IV is used to extract the dark current based on Equation 3.1. But it is based on the assumption that the carrier lifetime stay unchanged under illumination and that the emission condition is unchanged. In some cases such as cells with light induced trapping centers, the condition obviously does not hold any more.

Here we show the dark IV characteristics of a GaAs solar cell (M1215). The data was obtained with the Newport 6478 Picoamp meter which is programed with Labview.

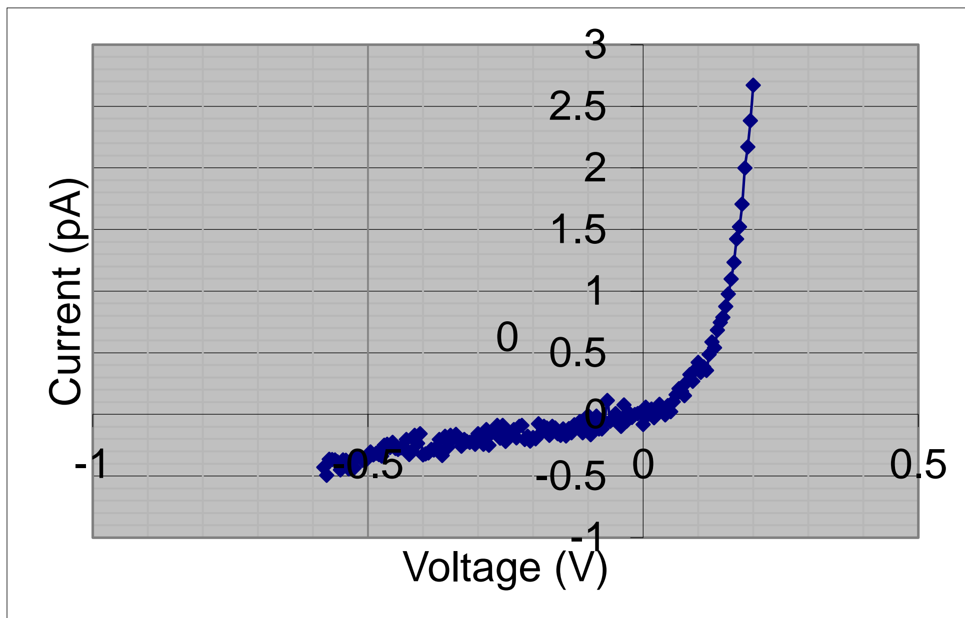

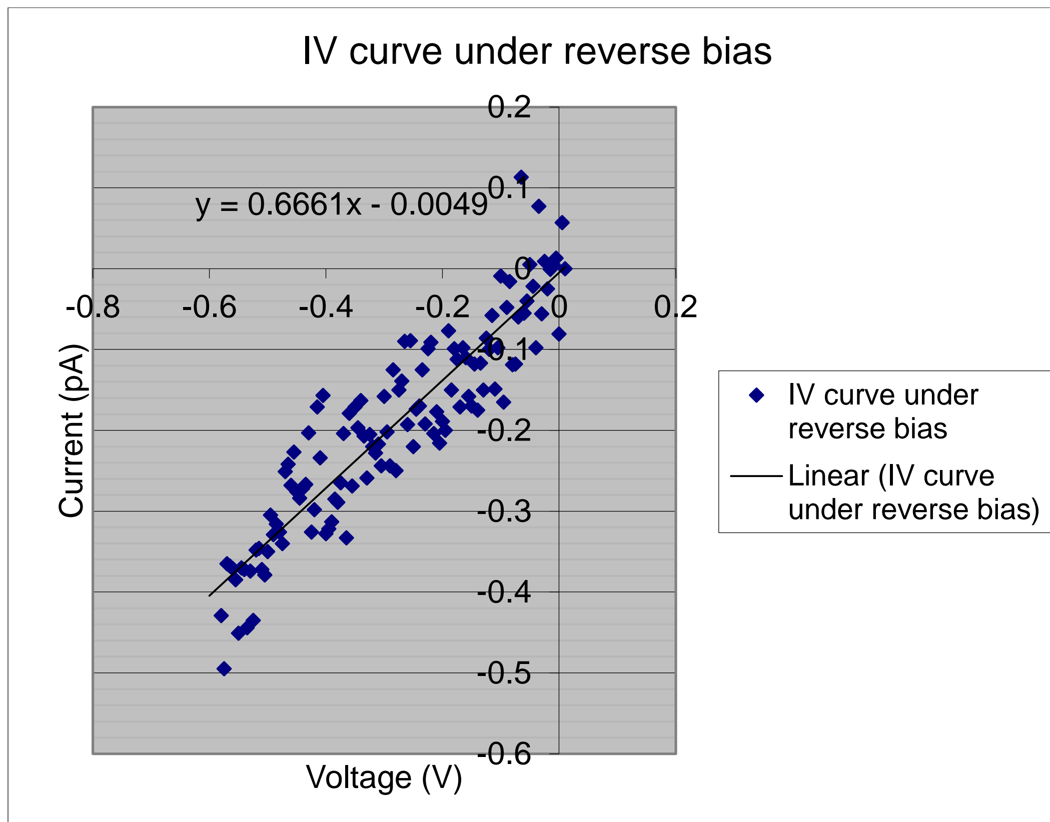

Figure 3-2: (a) The dark IV characteristics for the bulk GaAs solar cell M1215. (b) From a fitting under reserve bias, the dark saturation current can be estimated.

3.1.2 External quantum efficiency characterization

Quantum efficiency measurement (EQE) is one of the most important methods to probe the spectral response of the solar device. The external quantum efficiency is defined as the number of electrons extracted divided by the number of photons incident on the solar cell. The internal quantum efficiency is the number of electrons extracted divided by the number of photons absorbed. Below is the typical setup used during an external quantum efficiency measurement.

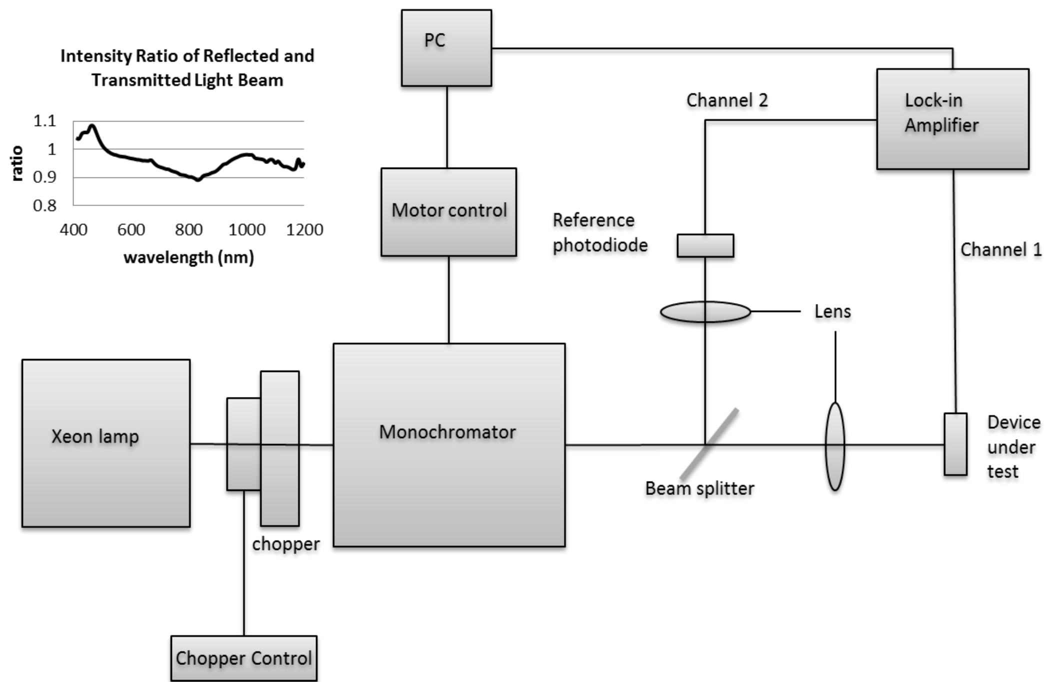

Figure 3-3: External quantum efficiency setup

The EQE data reveals a wealth of information about the different physical processes. The shape of the spectrum is a measure of the distribution of states. For the first time, we have used the EQE set up to probe the transition energy between the valance band to the InAs/GaAs QD states, and to measure the below-bandgap tailing density of states distribution. The experimental results are in good agreement with our theoretical model and the results from others' reports. The detailed experimental results can be found in Chapter 4.

3.1.3 Photoluminescence /Electroluminescence measurement

Luminescence process results form a nonequilibrium situation where carriers tend to relax to the lowest available energy states, such as band edge, or other lower

energy states within the forbidden band, given the existence of a carrier relaxation pathway. We have used photoluminescence (PL) measurement to investigate the carrier relaxation and carriers distribution in the QD device, which we will present in great details in Chapter 4.

We have used a halogen lamp as the light source with a 650 nm short pass filter. The spot size of the illumination spot is around 2 mm. The illuminated light from the sample is then collected via a 2 inch lens and then goes through the spectrometer. In order to reduce the shadowing effect for the light collection, the input illumination angle is slightly tilted as shown in the figure below. For the electroluminescence (EL) measurement, the device will be injected with electrons and holes via applied voltage. The electron-hole pairs relax to the lowest energy states and recombine radiatively, which we measure with spectrometer.

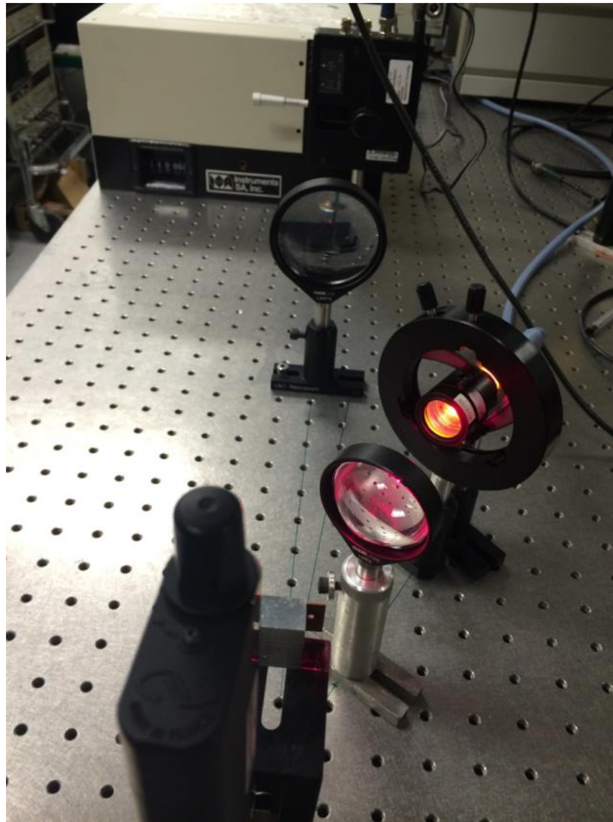

Figure 3-4: Photoluminensence setup with halogen lamp as light source. A 700 nm short pass filter is inserted (GaAs bandgap is around 880 nm)

Electroluminensence has also frequently been used to inspect the solar cell to find non-unifomities, crackings and defects. Figure 3-5 is a camera view of a bulk GaAs device under forward bias. The device is wired bonded. The area surrounding the bonded electrode bar is brighter because the diode current density is higher close to the wired electrode bar. The efficiency of current spreading depends on the electrode shape and the top layer's planar resistance.

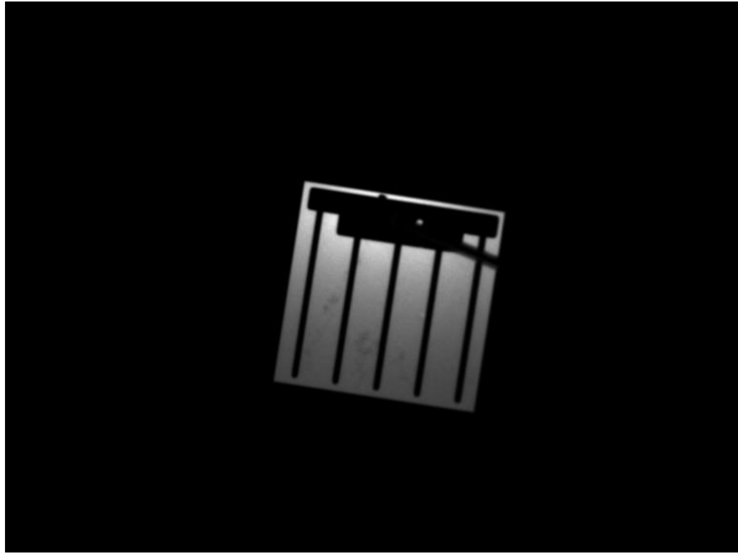

(a)

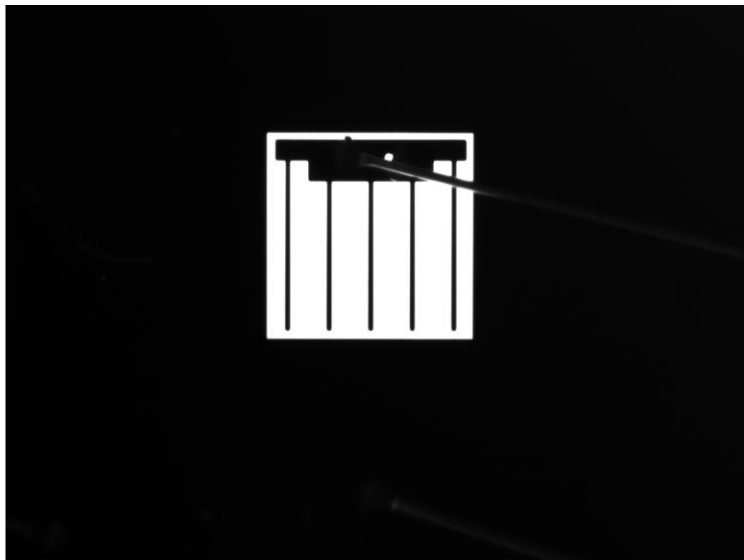

(b)

Figure 3-5: A $(500\ \mu m)^2$ bulk GaAs device illuminating under (a) 0.7 V and (b) 1 V bias. The area close to the wired electrode bar is brighter due to a higher generated current density.

3.1.4 Doping profile characterization with Hall measurement and Capacitance-Voltage measurement

Hall measurement is widely used to characterize the carrier density, the carrier type and the carrier mobility of a given semiconductor. The measurement is very simple. We have used the Hall Effect measurement system from Ecopia Corp HMS-5000 in the Fablab of the UMD Nanocenter. Ohmic contacts are required for four corners of the device. In order to ensure measurement accuracy, a current-voltage scan in between each two of the four electrodes is recommended. A linear I-V curve should be observed before loading the sample for Hall measurement.

The Hall Effect characterizes the surface layer, especially if the surface layer has been heavily doped. In order to gain an understanding of the doping profile along the thickness of the sample, other electrical methods are commonly used such as Secondary ion mass spectrometry and Capacitance-Voltage (CV) measurement. The C-V profiling technique requires a Schottky diode with metal contact. It relies on the fact that the space charge layer thickness varies with applied voltage. By fitting the measured differential capacitance at a certain voltage, the doping density can be estimated at the edge of the space charge region. The method is sometimes referred to as the *Hilibrand and Gold method* and it has an error bar of kT/q due to thermal excitation.

We have used the above described method to characterize the p-GaN doping profile. The device is patterned according to Figure 3-6.

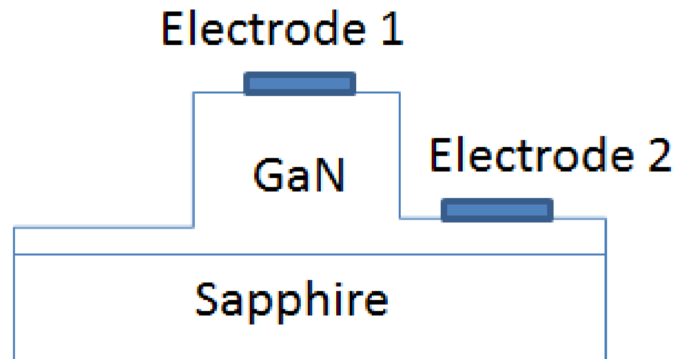

Figure 3-6: The device configuration for Capacitance-voltage profiling technique

The device preparation steps are as follows:

1. Use PECVD to deposit Si_3N_4 hard mask. A duration of 60 min results in a thickness of 1040 nm.

2. Pattern the mesa area.

3. Use F-ICP to etch Si_3N_4 for 2 min 30 sec, resulting in a 1 μm step (recipe name: Mario Si_3N_4 etch).

4. Clean PR.

5. Use Cl-ICP 8 min 30 sec. A step of 2.85 μm of GaN sample was formed (recipe name: Mario GaAs etch).

6. Use F-ICP to clean Si_3N_4 mask.

7. Pattern bottom electrode (Use AZ 5214 for image reverse patterning). Use HCl : DI Water=1:10 to clean GaN surface for 30 sec before pattern (Ti/Al/Ni/Au=10/200/20/200 nm).
8. Pattern top electrode using the same method.
9. Connect device to Agilent spectrum analyzer and calibrated LCR meter E3649A with proper adapter (Pomona 5299).
10. DC power bias is supplied by E3649A, controlled with Labview. Capacitance-Voltage is measured with LCR meter, plotted with Labview. Based on the Hilibrand and Gold C-V formula, charge concentration profile is derived and plotted.

The Hilibrand and Gold C-V formula is as follows:

$$x = \frac{\varepsilon}{C}$$

$$dx = -\frac{\varepsilon}{C^2}dC$$

$$dV = \frac{dQ}{C} = \frac{qN_A(x)dx}{C} = \frac{qN_A(x)\left(-\frac{\varepsilon}{C^2}dC\right)}{C} = -qN_A(x)\frac{\varepsilon}{C^3}dC$$

$$N_A(x) = {}^{-(C^3/q\varepsilon)}\Big/_{dC/dV} = {}^{(2/q\varepsilon)}\Big/_{\left[d\left(\frac{1}{C^2}\right)/dV\right]} \qquad 3.2$$

In the above formula, x is the depletion layer thickness under certain bias, C is the measured capacitance and V is the applied Voltage. N_A is the doping density.

An example of the as measured CV curve and the derived doping profile according to equation 3.2 for a Fe-doped GaN sample is shown in Figure 3-7.

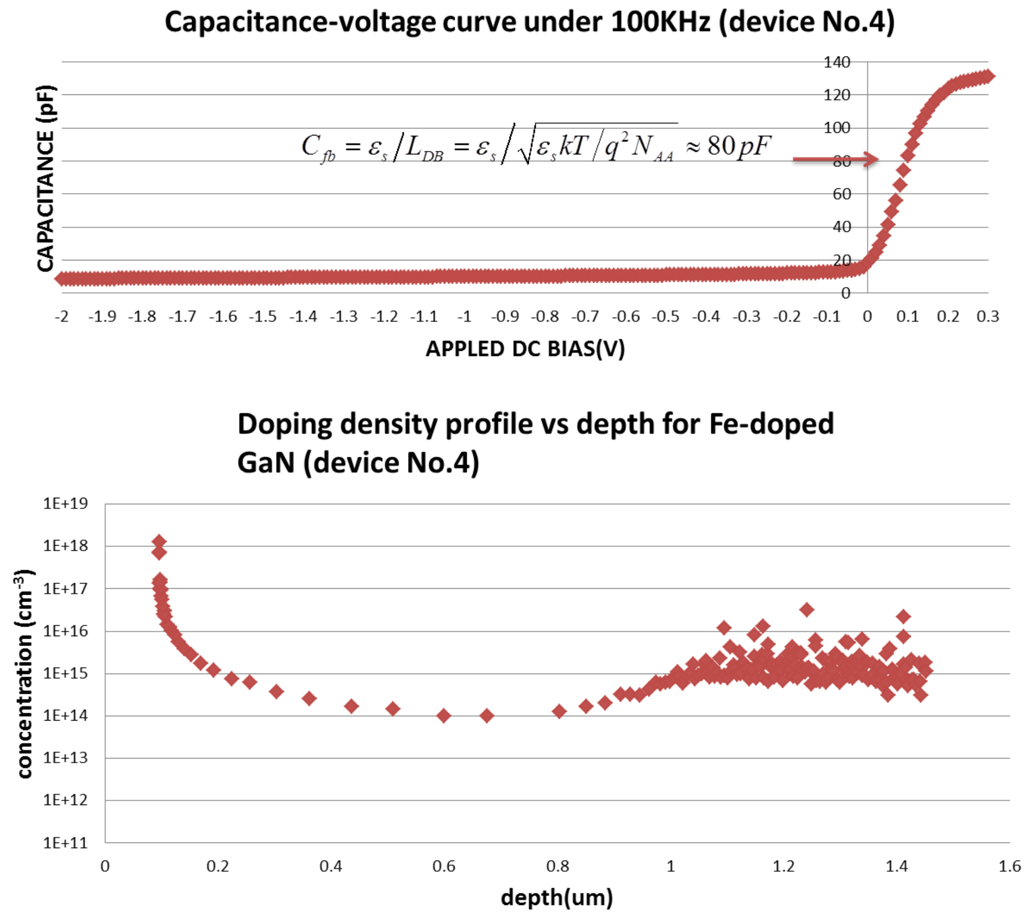

Figure 3-7: Measured CV curve and the derived doping profile for a Fe-doped GaN sample patterned with Ti/Al/Ni/Au electrodes

3.2 Comparison between different bulk GaAs solar cells

The different GaAs semiconductor structures that we have received from different collaborators will be discussed here.

3.2.1 The effect of absorption layer doping level

First we have investigated the effect of the doping level in the main absorption layer. In the later study of the QD devices, the multiple layer of QDs needs to be inserted into the main absorption layer. There has been plenty of discussion on the effects of doping level within the QD region. We believe that the effect of the overall doping-induced band diagram change needs to be clarified before we investigate the role of QD doping. We have compared two structures M1091 and M1215. Both of these structures have a main absorption layer thickness of around 2 μm while for the M1091 sample, the main absorption layer is the un-doped layer and for the M1215 sample, it is the n-base layer.

The active region of a solar cell is the depletion region and the electron and hole diffusion region. For M1091, the depletion region is mainly the 1 μm intrinsic region. For M1215, the depletion region is much thinner, thus the active region is much thinner. More photons will be absorbed in the active region in M1091 so that it shows a high light-generated current density. From the measured one sun IV curve, M1091 shows a current density of 22.20 mA/cm^2 while M1215 shows a current density of 18.36 mA/cm^2. Meanwhile, with a thicker depletion

region, a much higher J_{02} is expected, since J_{02} is related to the recombination process within the depletion region. A higher dark current will result in a lower Voc. M1091 shows a Voc of 0.850V which is much lower than 0.949 V for the M1215 sample.

Table 3-1: Structure comparison between M1091 and M1215

Sample Number	M1091	M1215
p-GaAs	20 nm/5 $\times 10^{18}$	20 nm/2 $\times 10^{19}$
p-$Al_{0.8}Ga_{0.2}As$	30 nm/5 $\times 10^{18}$	30 nm/5 $\times 10^{18}$
p-GaAs	400 nm/1 $\times 10^{18}$	40 nm/5 $\times 10^{18}$
i-GaAs	**1000 nm/undoped**	100 nm/undoped
n-GaAs	300 nm/3 $\times 10^{16}$	**1000 nm/2 $\times 10^{17}$**
n-$Al_{0.8}Ga_{0.2}As$	100 nm/3 $\times 10^{18}$	30 nm/5 $\times 10^{18}$
n-GaAs substrate	N+	N+

Table 3-2: The performance comparison between M1091 and M1215

Main absorption layer	Voc (V)	Jsc (mA/cm^2)	Efficiency
M1215_with 1000 nm base layer	0.949	18.36	12.90 %
M1091_with 1000 nm intrinsic layer	0.850	22.20	13.74 %

3.2.2 The effect of absorption layer thickness

We have also showed a comparison between structures with different n-base layer thickness. We have three structures M1215, M1216 and M1217 with all the other layers exactly the same except for the n-base layer. M1215, M1216 and M1217 have an n-base layer thickness of 1000 nm, 2000 nm and 3000 nm respectively. Their detailed structure details are shown in Table 3-3.

With a thicker n-base layer, more photons can be absorbed. However, thicker n-base layer means a longer pathway before the carriers are collected. A larger dark saturation current density is expected which will leads to a slightly reduced Voc.

Table 3-3: Structure comparison between M1215/M1216/M1217

M1215/M1216/M1217	Doping Level (cm^{-3})	Thickness (nm)
p-GaAs	2×10^{19}	20
p-$Al_{0.8}Ga_{0.2}As$	5×10^{18}	30
p-GaAs	5×10^{18}	40
i-GaAs	undoped	100
n-GaAs	2×10^{17}	1000/2000/3000
n-$Al_{0.8}Ga_{0.2}As$	5×10^{18}	30
n-GaAs(buffer layer)	5×10^{18}	200
GaAs substrate	n-type	n-type

From the IV data of the three structures, we can see that the Voc has been reduced from 0.949 V to 0.945 V while the Jsc has increased from 18.36 mA/cm^2 to 20.70 mA/cm^2 when the n-base layer thickness increases from 1000 nm to 3000 nm. It is worth noting here that during fabrication, in order to minimize the fabrication induced difference, the three structures had exactly the same mesa height during ICP etching process. This means that they have been through

exactly the same etching time so that their sidewall quality should be similar. Sidewall quality of the mesa wall is critical. The surface recombination rate of GaAs is extremely high. A slightly higher surface state density will degrade the performance greatly. Generally the sidewall and the top surface quality can be restored partially via the passivation process. We have usually fabricated our solar devices of the area of 300 μm by 300 μm, 400 μm by 400 μm and 500 μm by 500 μm. By a careful measurement of a large number of devices of a particular size, we have found that the device's Voc is generally lower for smaller size devices compared with larger size devices. Even though it is very hard to eliminate all the non-radiative surface recombination, a good passivation and a good structure design will help minimize the performance differences of difference area devices.

Table 3-4: Performance comparison of M1215, M1216, and M1217 before passivation and Anti-Reflection Coating

main absorption layer (n-GaAs) thickness (μm)	Voc (V)	Jsc (mA/cm^2)	Efficiency
1 μm (M1215)	0.949	18.36	12.90 %
2 μm (M1216)	0.947	19.57	14.52 %
3 μm (M1217)	0.945	20.70	14.96 %

4 Quantum dot solar cells

4.1 InAs/GaAs quantum dot solar cell

To investigate if QDs facilitate long wavelength photon absorption, we have used a reference structure (M1158) with 2000 nm intrinsic region as the main absorption region. The 40 layers of QDs with an interspacing of 50 nm are inserted into the intrinsic region. The build-in electric field helps to extract QD region generated carriers and sweep them to the electrodes. InAs dots were grown on GaAs using the Stranski-Krastanov approach by first depositing 2.0 monolayers of InAs. Due to accumulated stress, quantum dots are formed and a wetting layer is left forming a thin quantum well layer. The backside electrode is made up of the following layers Au/Ge/Ni/Au 5 nm/30 nm/20 nm/150 nm and forms the n-side contact. The metal layers are deposited with an e-beam evaporator, followed by a programed one-minute rapid thermal annealing at 400 ℃ in Nitrogen atmosphere. A p-type Ti/Pt/Au 30 nm/50 nm/150 nm contact layer was thermally deposited on top of the 50 nm p-type GaAs contact layer. This thin GaAs layer is etched away after electrode deposition to maximize the quantum yield. Each device is electrically isolated via induced coupled plasma etching. A mesa area of 500 μm by 500 μm is formed after etching into the n-base layer. PECVD deposited Si_3N_4 is used as the hard mask during the etching process. The

devices were subsequently passivated with a thin layer of sulfur and were immediately encapsulated by a 55 nm PECVD deposited Si_3N_4 for long term protection. Besides its role as an encapsulation layer, Si_3N_4 can also function as an AR-coating layer. In order to further reduce the reflectivity of the GaAs surface, Al_2O_3 and SiO_2 were also deposited on the sample. Our process recipes have been calibrated carefully to insure process repeatability. The average reflectivity over the wavelength of the GaAs solar cell was reduced to about 8%. An in-plane quantum-dot density of ~3.8 x 10^{10} cm^{-2} is shown in the Atomic force microscopy image below. The quantum dots are exposed after a selective etching of the GaAs capping layer.

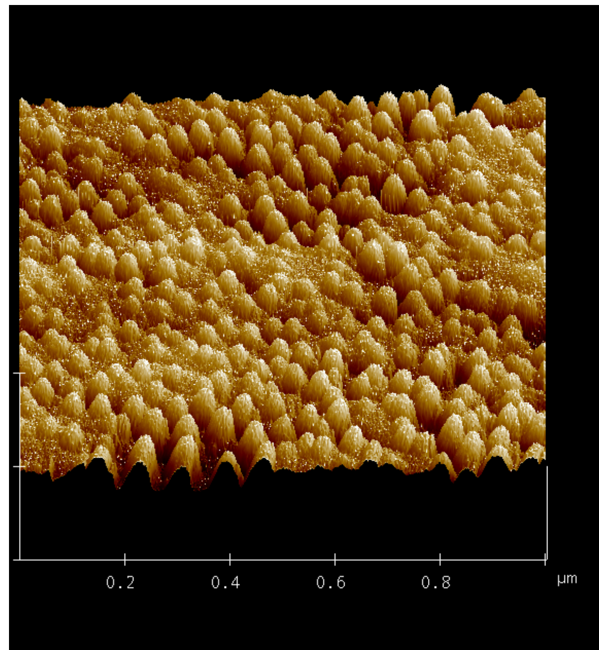

(a)

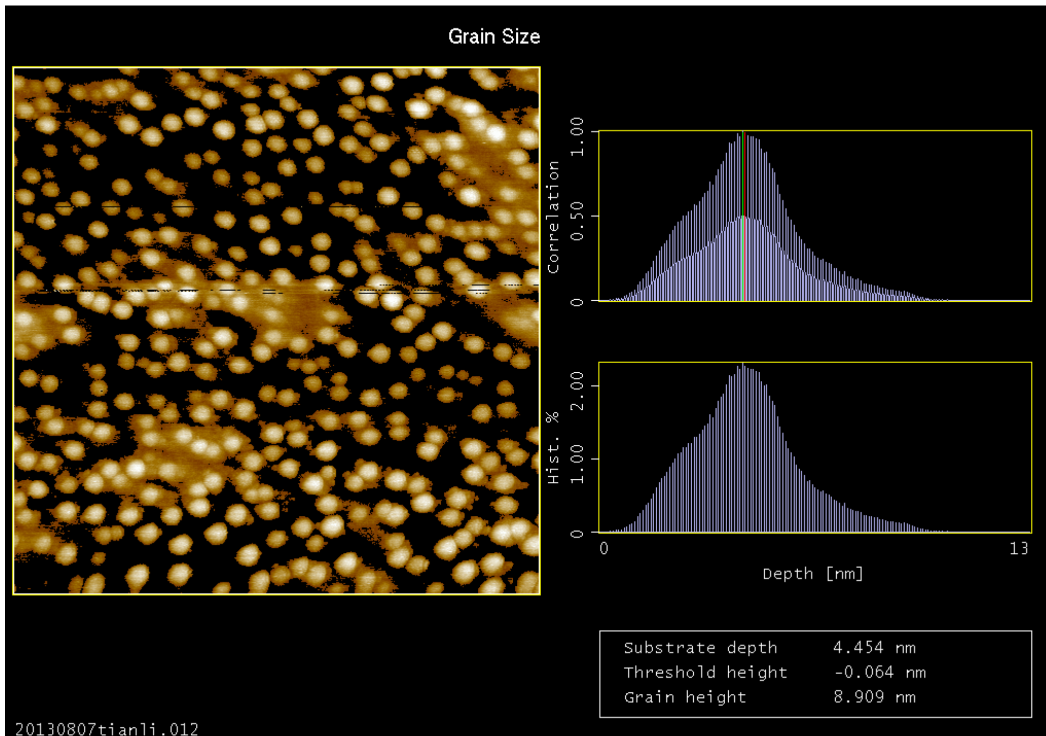

(b)

Figure 4-1: 1×1 μm^2 atomic force microscopy image of QDs, showing a sheet density of around $\mathbf{3.8 \times 10^{10}/cm^2}$. The QDs are incorporated using the self-assembled method.

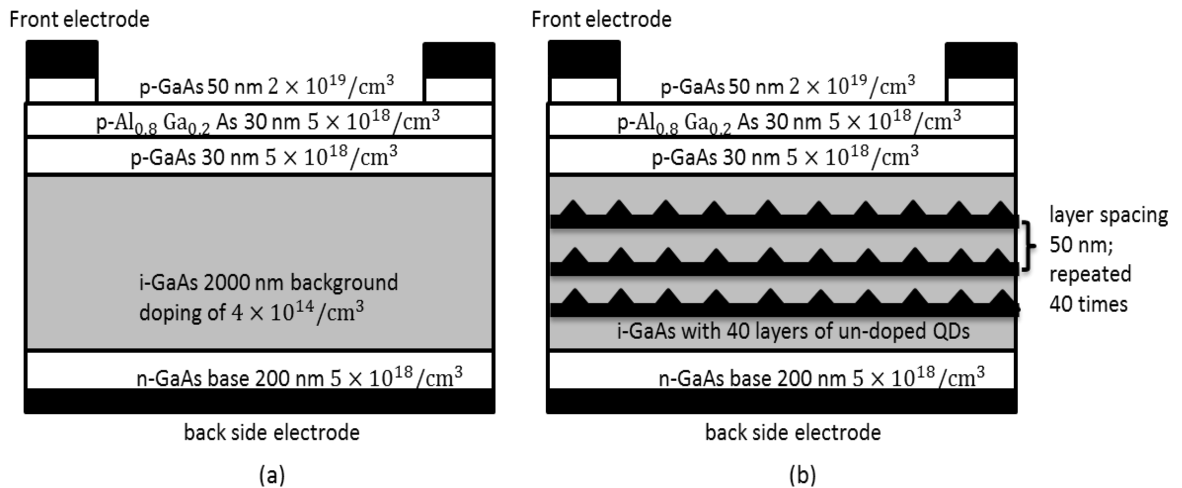

Figure 4-2: (a) Layer diagram for bulk device (b) Layer diagram for quantum dot device.

4.2 The current-voltage characteristics of QD solar cell

To investigate the contribution of the ensemble of InAs/GaAs quantum dots to the number of photogenerated carriers, we have measured the photo response under one sun illumination for both sets of wafers. Before coating with Si_3N_4, the QD sample has a current density of 24.8 mA/cm^2, compared with 23.2 mA/cm^2 for the reference structure. Clearly, we generate a higher short circuit current in our quantum dot devices as compared to the bulk solar cell. After depositing an AR coating, we measured a short circuit current of 29.9 mA/cm^2 (record) for the quantum dot sample (Figure 4-3), with an open circuit voltage of 0.77 V, lower than that of the reference GaAs sample which had an open circuit voltage of 0.92 V. The overall efficiency η for our quantum dot solar cell is 17.8 % (near record), when the V_{oc} has been reduced by about 157 mV as compared to our bulk sample(Li and Dagenais., Sept.2013; Dagenais et al., 2013; Li and Dagenais, Sept.2013).

The current-voltage characteristics of both the bulk and quantum dot devices, shown in Figure 4-3, were simulated according to the following model, which include both the diffusion part of the current (Js1) and the Shockley-Read-Hall recombination at impurities levels in the depletion layer (Js2):

$$J = J_L - J_{s1}\left[\exp\left(\frac{eV}{kT}\right) - 1\right] - J_{s2}\left[\exp\left(\frac{eV}{2kT}\right) - 1\right] \quad (1)$$

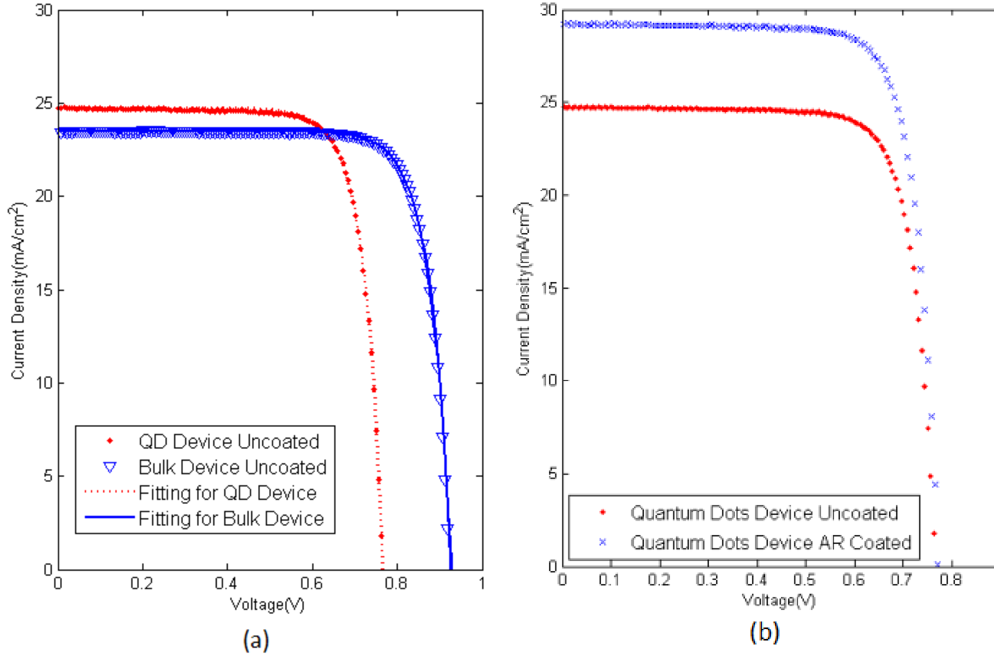

Figure 4-3: (a) Measured and fitted current-voltage characteristics for bulk and QD sample before anti-reflection coating (b) Current-voltage characteristics for quantum dot sample before and after anti-reflection coating.

In this expression, J_L represents the photocurrent density at standard 1-sun illumination. A perfect fit to the data is obtained for the following set of parameters shown in Table I, with the fitting curves shown in Figure 4-3. The diffusion constant J_{s1} for quantum dots is 1500 times larger than the bulk. The Shockley, Read, and Hall recombination coefficient J_{s2} is 19 times larger for the quantum dot sample as compared to the bulk sample. Most of the observed

change of V_{oc} is due to the change of the Shockley, Read, and Hall recombination coefficient Js2. For instance, if J_{s2} is further increased by a factor of 10 to Js2 = 6.5 x 10^{-5} keeping J_{s1} the same, this leads to a decrease of V_{oc} from 0.77 V to 0.66 V and increasing J_{s2} by another factor of 10 decreases V_{oc} to 0.54 V. This indicates the extreme sensitivity of V_{oc} to impurity and defects in the depletion region where QDs are inserted.

Table 4-1: Fitted parameters based on two diode model before anti-reflection coating (Illuminated area is used to calculate current density)

Device	J_L (mA/cm^2)	Voc (V)	Fill Factor (%)	J_{s1} (mA/cm^2)	J_{s2} (mA/cm^2)
QD	24.7	0.765	78.0	9.0×10^{-13}	6.5×10^{-6}
Bulk	23.4	0.922	80.1	6.0×10^{-16}	3.4×10^{-7}

Quantum dots have widely been employed for the realization of Intermediate band solar cells. The confined energy levels, especially ground energy levels in an ensemble of quantum dots act as additional energy levels within the forbidden

band. The states within the hole quantum dot potential near to the valence band are very closely spaced and, at room temperature, they behave as to increase the valence band maximum. The lower states within the quantum dot potential on the conduction band side are separated by energy larger than the phonon energy and should not directly contribute electrons to the conduction band (phonon assisted transition). On the other hand, electrons excited to some excited state within the electron quantum dot potential can relax to the ground state. A photon will take an electron from the top of the valence band to some intermediate state within the electron quantum dot potential. A second photon will be absorbed to take the electron which might have relaxed within the quantum dot potential into the conduction band.

4.3 The existence of an extended Urbach tail

When the density of the quantum dots is high enough, the wavefunctions of carriers overlap and form a band. This particular case happens with a spacing between QD layers of less than 10 nm. While the intermediate band formation is an obvious consequence of increased quantum dots concentration, we believe that another less desirable effect occurs: a perturbation of the band edge by the deformation potential and defect centers created at the QDs interface. Thus, a tail of states extending from the band edge into the energy band gap comes into being in the InAs/GaAs QDs device, superposed with confined quantum states in the WL and the QDs. This aspect, which has been overlooked, is almost *unavoidable.*

This extended tailing energy states in effect creates an "unblocked" path for electrons from the QDs states directly into the GaAs effectively lowered conduction band. Ever since the concept has been proposed, many experiments have been carried out to evaluate the role of inserted quantum dots to the performance of a solar cell. An increased short circuit current density and a reduced Voc have been repeatedly observed.

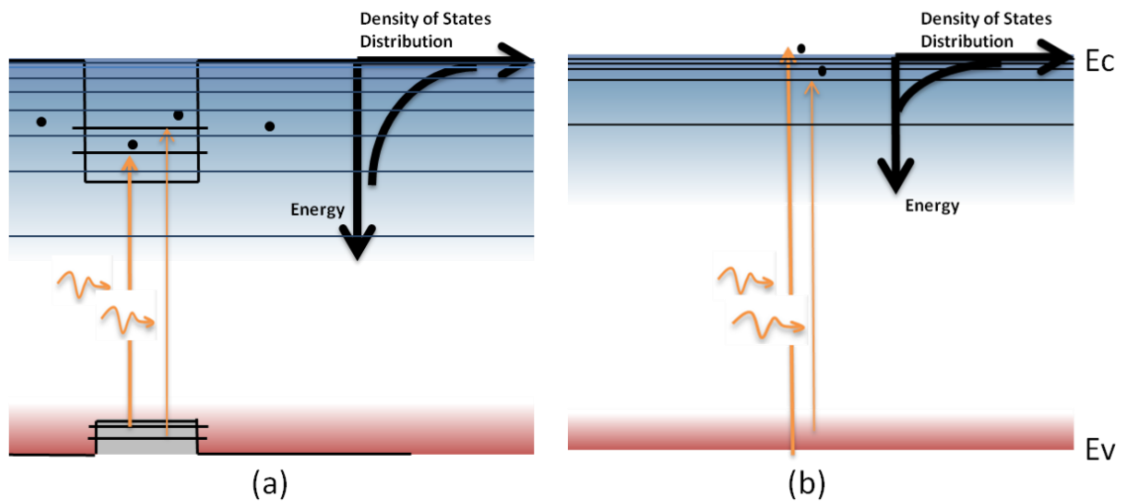

Figure 4-4: Energy diagram illustrating exponential distribution of tailing density of states for (a) an InAs quantum dot inserted region and (b) a bulk GaAs layer.

Technically, the band tails are formed at both the conduction band edge and valance band edge due to the deformation potential at the InAs/GaAs interface. Since the valance band offset is very small between strained InAs and GaAs, the quantum dots energy levels at the valance band edge are thermally connected with the band edge of GaAs. Equivalently, the valence band edge is lowered. While around the edge of the conduction band, an extended density of states distribution

is in superposition with quantum dots transition levels, as shown below in the density of states diagram (Figure 4-5).

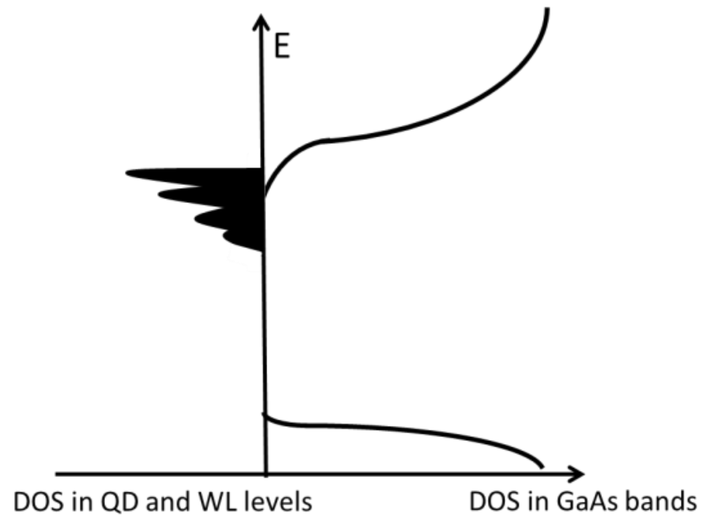

Figure 4-5: Density of states distribution diagram of the tailing states superposed with the quantum dots and wetting layer energy states

4.4 The effect of Urbach tail on below band-gap absorption and the derivation of Urbach energy

Before anti-reflection coating, a short circuit current density of 24.8 mA/cm^2 is measured for the quantum dots device and 23.5 mA/cm^2 for the reference bulk device under one sun condition. We extract a 5.5% of improvement in the short circuit current density in the quantum dots solar cell as compared to a bulk solar cell that we attribute to below bandgap absorption. As we will detail here, the origin of the longer wavelength photons absorption come not only from the transitions via quantum dots and wetting layer energy states, but also from an extended tailing density of states near the band edge.

The most straightforward verification of sub-bandgap photocurrent generation is by performing an external quantum efficiency measurement. By integration of the spectral photon flux under 1 sun condition and assuming a near 100% internal quantum efficiency, both above- and below- bandgap contributed photocurrents can be accurately obtained. Taking a typical InAs quantum dot cell for example, the total photon flux above GaAs bandgap is roughly 2.47×10^{21} photons/s while the total photon flux measured between the quantum dot ground state (assume to be at 1.1 eV) and the bulk bandgap energy is roughly 6.47×10^{20} photons/s. Given the fact that the above bandgap EQE is generally much larger, the contribution of below bandgap photocurrent to the overall Jsc is expected to be *much* less than 20%.

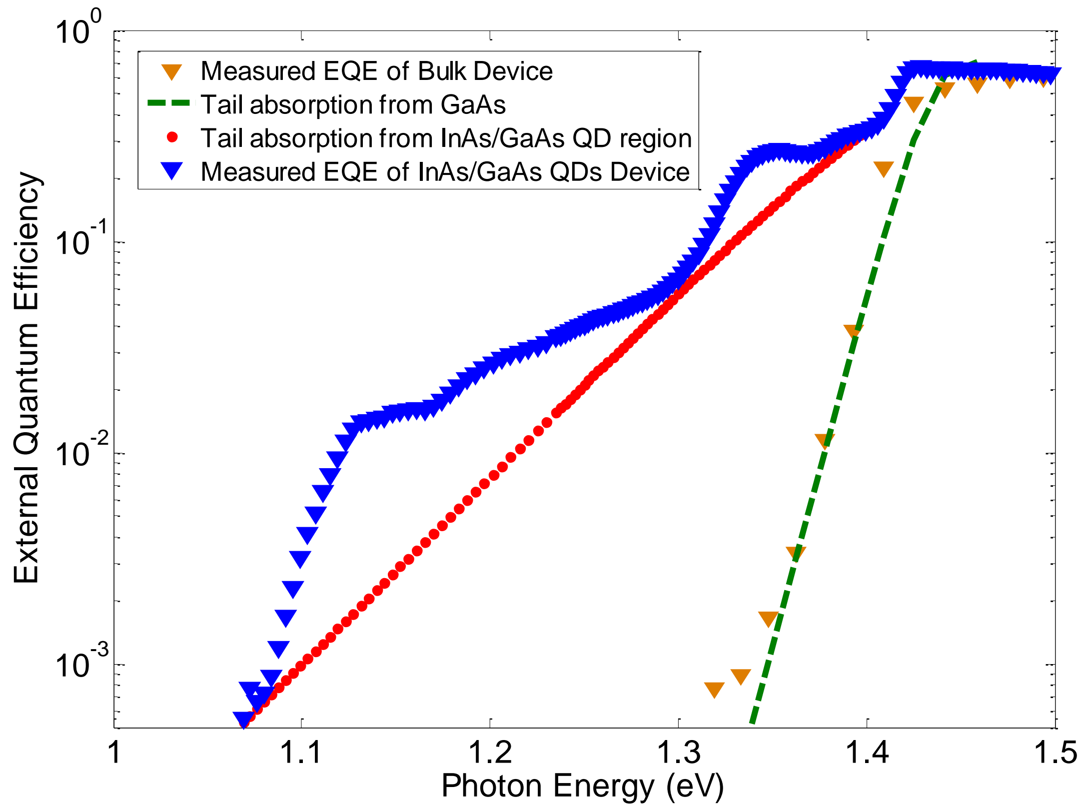

Figure 4-6: (a) Schematics of proposed interdot carrier transfer mechanism through continuum density of states due to Urbach tail absorption in the GaAs matrix in intrinsic layer and (b) External quantum efficiency of GaAs/InAs quantum dot sample with no anti-reflection coating. The Urbach tail contributions for both devices are shown by the dotted lines. Note that the Urbach tail arising from the QD region has a much smaller slope, meaning a much higher characteristic width E1 for the absorption edge. Absorption peaks corresponding to different size QDs or QD transition energies are observed.

In this work, we have used the external quantum efficiency measurement to extract the absorption coefficient over a wide wavelength range below the GaAs bandgap in order to elucidate the different absorption mechanisms not previously measured in detail for InAs QDs embedded in GaAs. The external quantum efficiency measurement is performed with a halogen lamp and a 650 nm long pass filter is used to filter out the grating second order contribution to the transmitted light. A low noise current preamplifier SR 570 from Stanford Research Systems is connected to the external circuit of the device prior to the EG&G 5210 lock-in amplifier. The chopping frequency has been set at 283 Hz.

4.5 Derivation of band tail absorption width

In crystalline GaAs, the extended energy states near the band edge, which facilitate the below band gap absorption, are described by an Urbach tail (Urbach, 1953; Pankove, 1975), and are the consequence of a break from a perfect lattice periodicity of the crystal. This exponential distribution of states below the band gap leads to an absorption coefficient that varies with energy according to the following expression:

$$\alpha_{Urbach} = \alpha_0 \, e^{-\frac{E_g - \hbar\omega}{E_U}} \qquad 4.1$$

where E_U is the characteristic width of the Urbach absorption edge, and α_0 is a scaling parameter in units of cm^{-1} which is proportional to the amount of absorption at a certain detuning below the gap. Studies of the Urbach tail are

critical since it seems almost inescapable that the presence of InAs/GaAs QDs greatly disturb the perfect lattice periodicity of the GaAs, and thus lead to a broadening of the GaAs band edge.

In general, for photon energies smaller than the band gap, the absorption process happens throughout the entire region where one can integrate the generation rate over the film thickness, and derive an equation relating the external quantum efficiency with the absorption coefficient (Chuang, 2009):

$$\eta_{ext} = (1 - R)(1 - e^{-\alpha L})\eta_{int} \qquad 4.2$$

where η_{ext} is the external quantum efficiency, η_{int} is the internal quantum efficiency, L is the layer thickness, R is the surface reflectivity, taken to be 0.3. When the absorption coefficient is sufficiently small, the above equation can be further simplified to:

$$\eta_{ext} = (1 - R)(\alpha L)\eta_{int} \qquad 4.3$$

Equation (4) describes the linear dependence of the external quantum efficiency on the absorption coefficient for below bandgap absorption, under the assumption that the internal quantum efficiency is wavelength independent within this region of interest. Hence the width of a device's absorption tail can be determined by a measurement of below bandgap EQE.

We find it much more visual to plot the bandtail carrier generation efficiency semilogarithmically, as shown in Fig. 6. For a crystalline GaAs bulk device, the

energy states within the band mainly come from the intrinsic lattice disorder introduced by dopants. According to the analysis above, the external quantum efficiency measurement below the gap follows a similar exponential dependence on energy as the absorption coefficient. As shown by a green (color on-line) dashed line in Fig. 6, the measured data can be fit with:

$$\eta_{ext} = 0.037\exp[-(1.39 - \hbar\omega)/0.013] \quad 4.4$$

The above measured bulk GaAs device has a 400 nm 2 x 10^{17}/cm^3 doped p-region on top, followed by a 100 nm i-region, and a 2000 nm 5 x 10^{18}/cm^3 doped n-region. Since the EQE and absorption share the same energy dependence in the small absorption bandtail region, an absorption width of 13 meV can be determined. This is consistent with previous measurements of p-type GaAs (Greeff and Glyde, 1995a; Johnson and Tiedje, 1995). Typically a p-type GaAs layer has a higher absorption width than that of an intrinsic GaAs (~7 meV). When light is incident on top of the device, the p-GaAs emitter layer functions as the dominant layer for below-bandgap photon absorption. Experimentally, the fit yields an absorption width of 13 meV and a band edge of 1.39 eV, which are very typical for p-GaAs. This good agreement encourages us to adopt this model to describe a tailing density of states in a QD device.

For a QD device, the absorption coefficient is affected by the QD and WL energy states along with the exponential distribution of tailing energy states. In

other words, the below-bandgap photo-generated carriers result from these three sources: the Urbach tail absorption and both the QD and WL absorption:

$$\eta_t = \eta_{Urbach} + \eta_{QD\&WL} \qquad 4.5$$

η_t denotes the total measured external quantum efficiency, which consists of the external quantum efficiency contributed via Urbach tail absorption (η_{Urbach}) and the external quantum efficiency contributed via QDs and WL absorption ($\eta_{QD\&WL}$). One can use a similar form as Equation 4.2 to relate the Urbach tail absorption coefficient (α_{Urbach}) and the carrier generation efficiency:

$$\eta_{Urbach} = (1 - R)(1 - e^{-\alpha_{Urbach} L})\eta_{int} \qquad 4.6$$

When the incident photons have a lower energy than the lowest quantum dot ground state energies, they can only be absorbed via the tailing states that extend further into the mid gap. We have therefore fitted the Urbach tail to go through the measured EQE data from 1.065 eV to 1.085 eV. The measurement of the tailing behavior to deep energy levels is limited by the sensitivity of the EQE system. The blue (color on-line) dashed curve connecting the reading from 1.08 eV to the band edge denotes the contribution of the Urbach tail in the semilogarithmic plot of Fig. 4.6. The curve is generated by Equation 4.5 with the fitted Urbach tail absorption coefficient in the form shown below:

$$\alpha_{Urbach} L = -0.4 \times e^{-(1.424 - \hbar\omega)/0.050} \qquad 4.7$$

From the fit, the Urbach tail absorption width is found to be 50 meV, which is much larger than that of a bulk GaAs film.

The broadening of the absorption tail results from the QD perturbation of the band edge. InAs has a larger lattice constant (6.05 A) than that of GaAs (5.65 A). The built-in strain of InAs QDs disrupts the lattice and creates fluctuations of the internal field. A tail absorption width of 50 meV is obtained according to the fit, which is understandably much larger than that of a GaAs film. It is worthwhile to note that 50 meV is an average value of the local broadening created by InAs QDs, under the condition that the QDs are uniformly distributed in the 2000 nm intrinsic region of the host material.

4.6 Derivation of Quantum dot and wetting layer absorption coefficient

A better understanding of the tailing density of states distribution around the band edge of QD device enables us to quantitatively evaluate the QD and WL oscillation strength. According to Equation 4.6, one can obtain the carrier generation efficiency via the QD and the WL transition levels ($\eta_{QD\&WL}$) by subtracting η_{Urbach} from the measured η_t. In Figure 4-7 the contribution of the wetting layer and quantum dots are plotted separately based on their transition energies. The absorption coefficient contribution of the QD and WL to $\eta_{QD\&WL}$ is given by the following expression:

$$\eta_{QD\&WL} = (1-R)(1-e^{-\alpha_{QD\&WL}L})\eta_{int} \qquad 4.8$$

By making the assumption that the internal quantum efficiency is 100% through the energy range of interest, the dependence of $\alpha_{QD\&WL}$ in energy can then be plotted. This is shown in Figure 4-7(b). The integration of QD absorbance (from 1.05 eV to 1.30 eV) from this experimentally derived curve is around $4.7 \times 10^{15}/cm \cdot s$.

In theory, the integral of the absorption coefficient over frequency for the ground level transition of QDs is directly related to the spontaneous lifetime in quantum dots via the following expression (Alén et al., 2003; Birkedal et al., 2000)

$$\int \alpha_{QD_{ground}transition}\, dv = \frac{3N\lambda^2}{8\pi n^2 \tau_{sp}} \tag{4.9}$$

where we take $\tau_{sp} = 1\ ns$ (Harbord et al., 2009) and n is the index of refraction. N is the density of QD ground states in the absorber and is twice the QD density, which is $1.5 \times 10^{16}/cm^3$. The theoretically integrated absorbance via QD ground states is therefore $1.5 \times 10^{15}/cm \cdot s$ according to Equation 4.10, which is in reasonable agreement of the experimentally derived value $4.7 \times 10^{15}/cm \cdot s$.

The measured and derived integrated QD absorption is close to the theoretical calculated number. Two potential sources for the difference include the assumption we have made in the derivation of the absorption curve, and the fact that the theoretical expression only accounts for the direct transition to the ground state of QDs. Also, since the indium flux can be non-uniform during wafer growth, we expect that the density can vary significantly over a region of 3 mm

diameter as the one probed by an optical beam. While a QD sheet density of $3.8 \times 10^{10}/cm^2$ was obtained with an 1 μm² AFM image (Li and Dagenais, 2013), the image was taken at a different spot on the wafer than the one that was used for the tested device.

To account for different quantum dot transitions, the overall absorption curve is fitted with Gaussian lineshapes centered at different wavelengths. For QD transitions, the local minima for the 1st derivative was used to identify the centroid of three main peaks centered at 1.130 eV, 1.200 eV and 1.253 eV. The other three Gaussians with smaller amplitudes were fitted to ensure the best fit to the experimental results. A fit of high accuracy to the overall absorbance is given by the following equation:

$$\alpha_{QD\&WL}L = 0.0075e^{-\left(\frac{x-1.130}{0.025}\right)^2} + 0.005e^{-\left(\frac{x-1.158}{0.020}\right)^2} + 0.013e^{-\left(\frac{x-1.200}{0.030}\right)^2} + 0.005e^{-\left(\frac{x-1.230}{0.020}\right)^2} + 0.011e^{-\left(\frac{x-1.253}{0.025}\right)^2} + 0.007e^{-\left(\frac{x-1.285}{0.025}\right)^2} + 0.125e^{-\left(\frac{x-1.347}{0.025}\right)^2} + 0.030e^{-\left(\frac{x-1.387}{0.013}\right)^2} \qquad 4.10$$

All fitted lineshape functions have a width (1/e) of about 25 meV and corresponds to an inhomogeneous linewidth reflecting a distribution of sizes of QDs. From the fit, three main quantum dots transitions are observed and might be due to ground or excited state conduction band transitions to the many confined electron states, with their respective transition energies centered at 1.130 eV, 1.200 eV and 1.253 eV. Our method provides a simple way to probe transition

levels below the gap. The fitted transitions involve, of course, both QD transition levels and WL transition levels. The transition centered at 1.347 eV and 1.387 eV can be attributed to the WL ground and excited state transitions.

Table 4-2: Fit transition states of QD absorption, compared with results measured by photo reflectance. Unit: eV

Transitions	QD1	QD2	QD3	QD4	QD5	QD6	QD7	WL1	WL2
Cánovas(Cánovas et al., 2008)	**1.065**		**1.150**	**1.187**	**1.227**			**1.327**	**1.362**
Aigouy(Aigouy et al., 1997)			1.140		1.219	1.260		1.337	1.373
this work		1.130	1.158	1.200	1.230	1.253	1.285	1.347	1.387

This is the first time that a measurement of external quantum efficiency at room temperature is used to derive the spectral dependence of the QD absorption. More commonly, people have used photoluminescence, photoreflectance, electroluminescence, and differential transmission measurements. As shown in Table I, our fitted results are in good agreement with the results obtained via other methods (Aigouy et al., 1997; Ding et al., 2011; Gardner et al., 2009). One advantages of our method is that it gives the absorption strength of all QDs transition levels directly. Potentially an even higher resolution can be obtained by taking the measurement at lower temperatures.

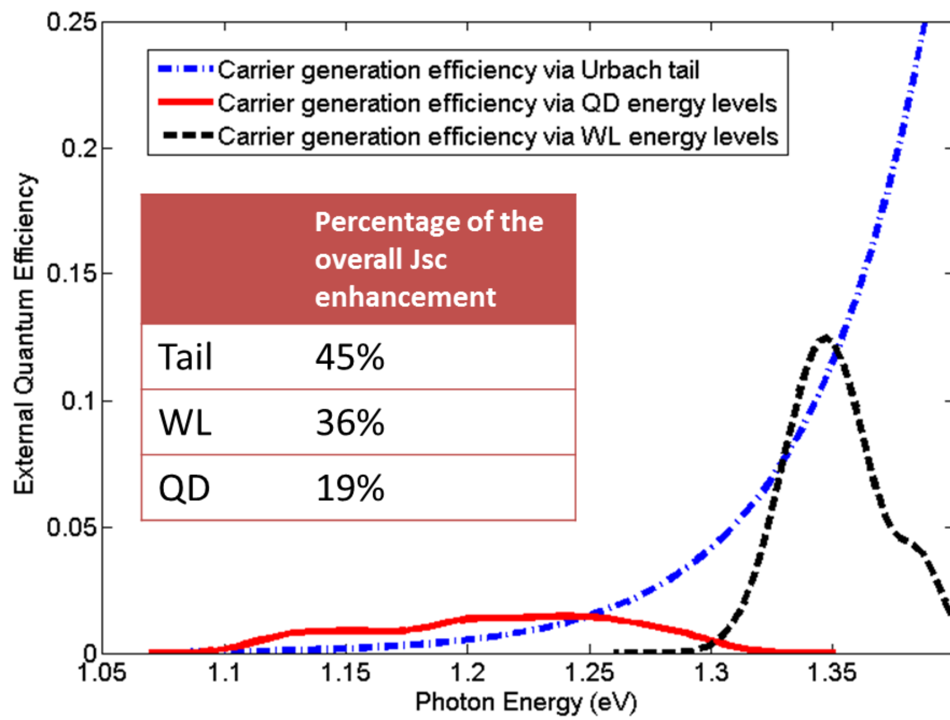

	Percentage of the overall Jsc enhancement
Tail	45%
WL	36%
QD	19%

(a)

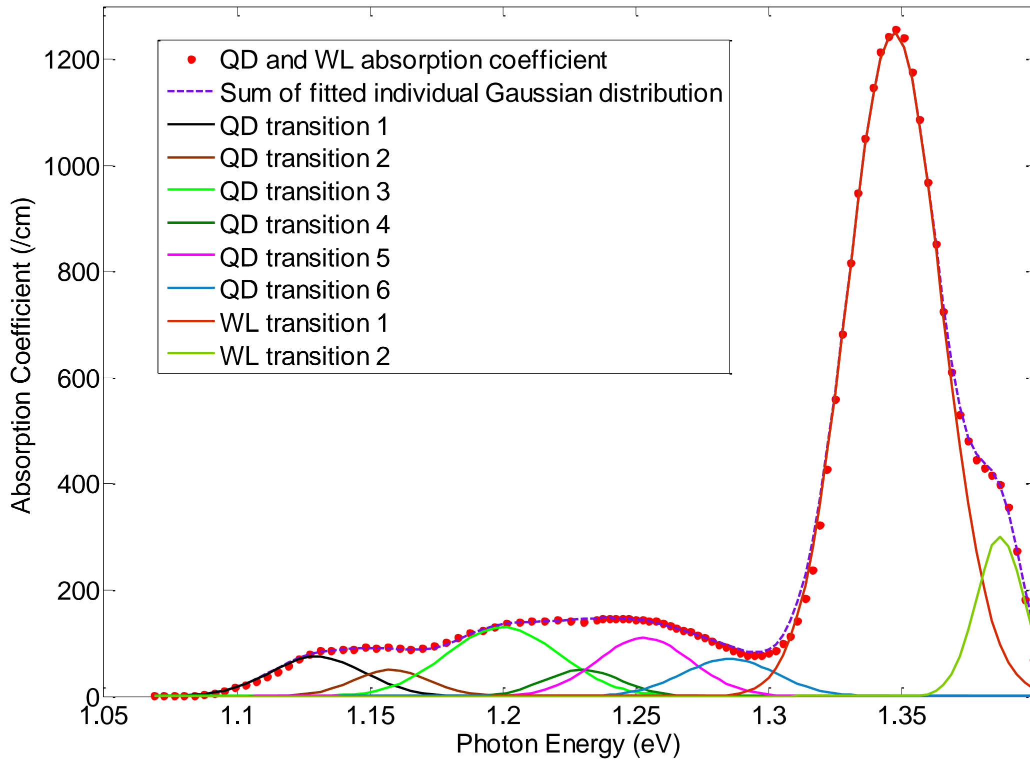

(b)

Figure 4-7: (a) External quantum efficiency due to carrier generation via the Urbach tail, the QD and the WL energy levels (b) derived quantum dot and wetting layer absorption coefficient and the Gaussian lineshape fitting for multiple transitions

Before anti-reflection coating, a short circuit current density of 24.8 mA/cm^2 was measured for the QD device and 23.5 mA/cm^2 for its reference device under Global AM 1.5 illumination. Their respective open circuit voltages are 0.77 V and 0.92 V, resulting in a conversion efficiency of 14.8% and 17.8%. Experimentally, we discovered a 5.5% improvement in the short circuit current density after

quantum dots were inserted into the 2000 nm intrinsic GaAs region. If we integrate the above derived $\eta_{QD\&WL}$ and η_{Urbach} with Global AM 1.5 illumination solar spectrum, in the below-bandgap region, one can find that the ensemble of QDs absorbs approximately $1.25 \times 10^{15}/cm^2$ photons, the wetting layer of InGaAs quantum well absorbs $2.43 \times 10^{15}/cm^2$ photons, while the extended Urbach tailing energy states absorb around $2.99 \times 10^{15}/cm^2$ photons. For comparison, a bare surface of bulk GaAs device absorbs around 70% of above bandgap photons ($2.12 \times 10^{17}/cm^2$). Hence the number of the absorbed below-bandgap photons in QD device is around 4.5% of the total number of above bandgap photons, in good agreement with the measured improvement of photocurrent in QD solar cell. However, the increase in the photo-generated current density from the tail absorption comes at the expense of a smaller Voc due to the corresponding conduction band edge lowering of the GaAs QDs region (Ding et al., 2011).

We have extracted the Urbach tail contribution from an EQE measurement for both QD and bulk devices under room temperature. The impact of extended Urbach tail absorption in an InAs/GaAs quantum dots solar cell was discussed and the characteristic width of the Urbach edge was derived for the first time. For bulk GaAs devices, the Urbach tail width is mainly determined by the doping level of the main absorption layer. In our case, p-type GaAs is the dominant absorption layer. The derived Urbach energy is 13 meV, which is in agreement with typical values for p-type GaAs. For the QD devices, the built-up strain

creates disruption to the lattice, which is characterized by a much larger Urbach energy broadening of 50 meV. We believe that this continuum tailing density of states has provided a competing path for the carriers on the intermediate states to be directly collected. The two-photon absorption cross section, which is key to the concept of IBSC, is therefore appreciably reduced. From the detailed line shape fit we have also accurately determined the energy states of QDs and WL with their respective absorption strengths. We have made the first measurement of the absorption strength of QDs states for an ensemble of quantum dots through a simple analysis of the EQE measurement. In fact, we have demonstrated that our measurement technique can be generally applicable to analysis of below-bandgap absorption and to quantitatively determine the transition energies in quantum dots and in a wetting layer.

4.7 The effect of Urbach tail on the QD device's EQE, IV, and PL results

An intrinsically formed extended tailing density of states surrounding the confined quantum states can function as an efficient relaxation and collection pathway in a quantum dot (QD) device. To investigate the carrier dynamics in the presence of the tailing states in a QD solar cell, we have carefully characterized two sets of devices with different tail widths. A non-equilibrium photoluminescence (PL) measurement and the current-voltage (IV) characteristic are used to evaluate the coupling effect between background tailing states and

confined quantum states. We show that the presence of the extended tailing states greatly affects the non-equilibrium carrier relaxation process in a QD solar cell, thus greatly affecting the solar cell performance.

The extended tailing states superposed with QD and wetting layer (WL) energy states within the forbidden gap of GaAs might greatly affect the carrier dynamics including carrier relaxation and collection. We believe that the intrinsically formed extended tailing states also provide a way to bypass the phonon bottleneck predicted by the zero dimensionality of QDs. The degradation of the open circuit voltage (Voc) is a good indicator of the broadening of the tail. We have carefully analyzed the performance of several sets of QD solar cells. The PL measurement has been used to reveal the non-equilibrium process of carrier relaxation.

The first set of devices is an $In_{0.5}Ga_{0.5}As$/GaAs QD solar cell grown by MOCVD. The planar density is around $4 \times 10^{10}/cm^2$ with a layer interspacing of 50 nm. The second set is made up of InAs/GaAs QDs. It has a similar planar density and the same interspacing of GaAs between each QDs layers. Both samples have the QDs incorporated in the intrinsic region. Both samples were fabricated with Ti//Pt/Au p-type and Au/Ge/Ni/Au n-type ohmic contacts. After metallization, the top p^+ GaAs contact layer was carefully mostly removed with citric acid and hydrogen peroxide solution and a 5 nm thickness was left behind for the protection of the AlGaAs window layer from oxidizing. Devices were characterized without sulfur passivation and anti-reflection coatings to ensure the

accuracy of the spectral response. The devices with a size of 500 μm×500 μm were formed with an illuminated area of $1.6 \times 10^{-3} cm^2$. Each device is electrically isolated by the formation of mesas using an Inductively Coupled Plasma (ICP) to etch into the n^+-substrate layer protected by a PECVD-deposited Si_3N_4 hard mask. Our recipes have been carefully calibrated to ensure uniform device performance.

A current-voltage measurement with a Newport Solar Simulator was performed to show the IV performance of the solar devices. We have associated the measured Voc degradation with the broadened tailing density of states whose width is quantified by an external quantum efficiency measurement (EQE) semilog plot. The position of the PL peaks indicates the energy separating the levels between which a strong interaction occurs.

4.8 The analysis of Voc degradation and Jsc enhancement from a modified Shockley-Queisser model

In this section, the fundamental limits that affect the conversion efficiency of quantum dot solar cells is discussed. Using a modified detailed balance analysis, we demonstrate that the existence of an extended tailing density of states fundamentally enhances the dark saturation current density and leads to a degradation of the open circuit voltage. We predict how the open circuit voltage (Voc) changes with the tail width and find agreement with the general trend

observed experimentally. In practice, the existence of non-radiative recombination would further reduce Voc.

From an intuitive understanding, a higher degree of inhomogeneity at the band edge results in a corresponding fluctuation of the chemical potential of electrons and holes. Under illumination, the electron-hole-quasi-Fermi-level splitting determines the output voltage. Electrons and holes tend to relax to their respective energy minimum in a fluctuating potential and then recombine. As a result, the output voltage is reduced correspondingly.

According to the blackbody distribution, semiconductors with lower energy gap have a larger emission current. Therefore, the enlarged emission current, which is in the opposite flow direction as compared to the photon generated current, will give rise to a reduced open circuit voltage, as illustrated in the figure below.

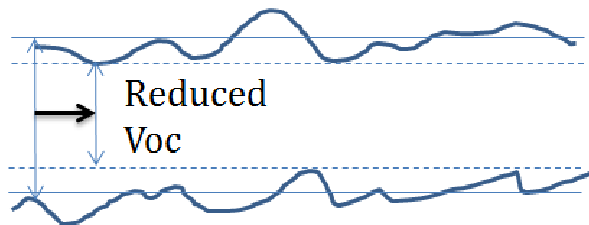

(a)

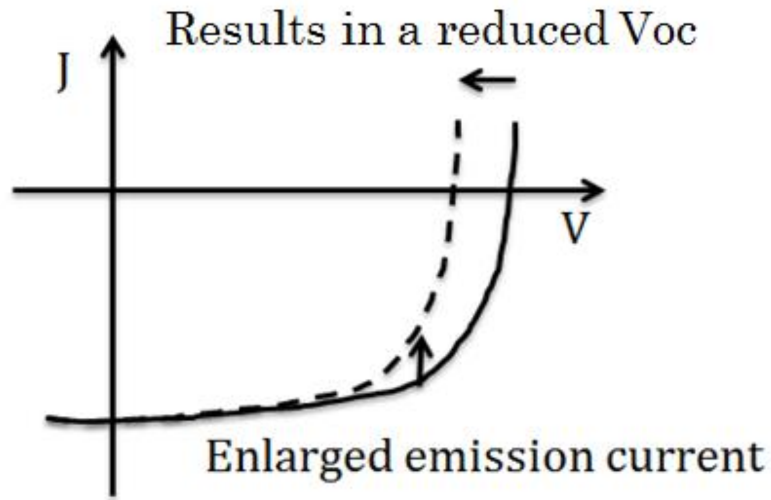

(b)

Figure 4-8: (a) The perturbation of the band edges by Coulomb interaction with inhomogeneously distributed impurities (Pankove, 1975). This leads to (b) the reduction between the separation of electron chemical potential and hole chemical potential, which will yield a reduction in Voc.

The dark current density serves as an important measure of the performance of solar cell. The open circuit voltage is associated to the dark saturation current density by the following expression:

$$Voc = \frac{k_B T_C}{q} \ln \frac{J_{SC}}{J_0} \qquad 4.11$$

Assuming such a cell in thermal equilibrium with no external light and no applied voltage, an ideal cell will be emitting black-body radiation with photon energy above the bandgap. By attributing all this radiation for energies above the semiconductor's bandgap to band-to-band recombination, the lowest possible

value of dark saturation current can be calculated, corresponding to the limiting efficiency of the solar cells. This is given by an integration of the hemispherical black-body emission under the current device temperature.

$$J_0 = q\frac{\pi}{2}[1 - cos\, 2\theta_E]\int_0^{\infty}\frac{2}{h^3c^2}\frac{E^2}{e^{E/k_BT_C-1}}f_E\, dE \qquad 4.12$$

where f_E is the emission function. In the paper by Shockley and Queisser, f_E is assumed to be a step-like function as the green curve in Figure 1. However, just like the bandgap value, the tailing width is another intrinsic material parameter which should be taken into consideration which will yield an emission function shown in red for bulk GaAs and blue for QD device. The curves are plotted with the parameters derived in our previous publication (Li and Dagenais, 2014). The bulk device has a tail width around 13 meV while the number increases to around 50 meV in a QD device.

By simulating an ideal solar cell as a perfect black-body radiator, its dark current density can be obtained by integrating between the black body radiation at 300 K and its corresponding emission function. To further clarify our calculation, semilog plots with blackbody radiation at 300K and log(emission) function are shown respectively with or without consideration of exponentially decaying emission function in Figure 4-9. As can been seen visually, the integration with tailing emission function generally ends up with a much larger dark current density than that with a step-like function, which leads to a degraded Voc according to the expression

$$Voc = \frac{k_B T_C}{q} \ln \frac{J_{SC}}{J_0} \qquad 4.13$$

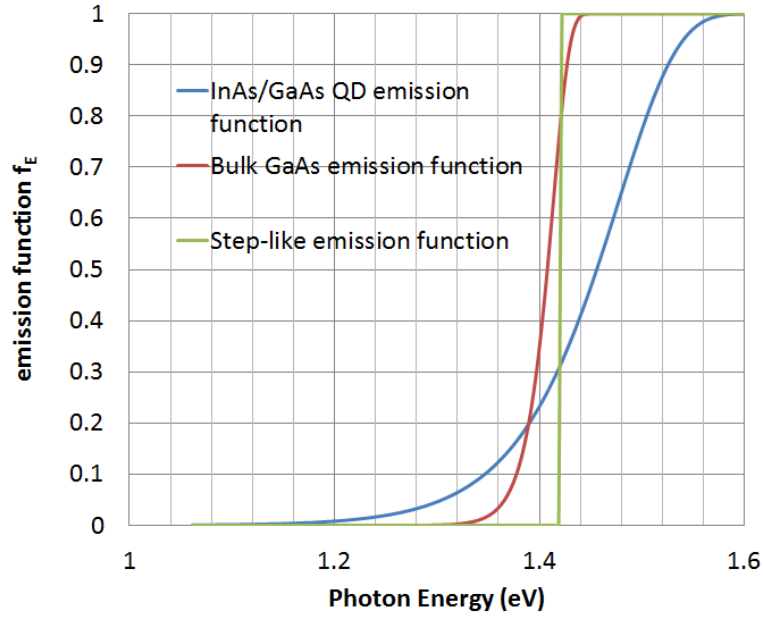

Figure 4-9: The emission functions for SQ model assumption, GaAs bulk device and InAs/GaAs QD device respectively.

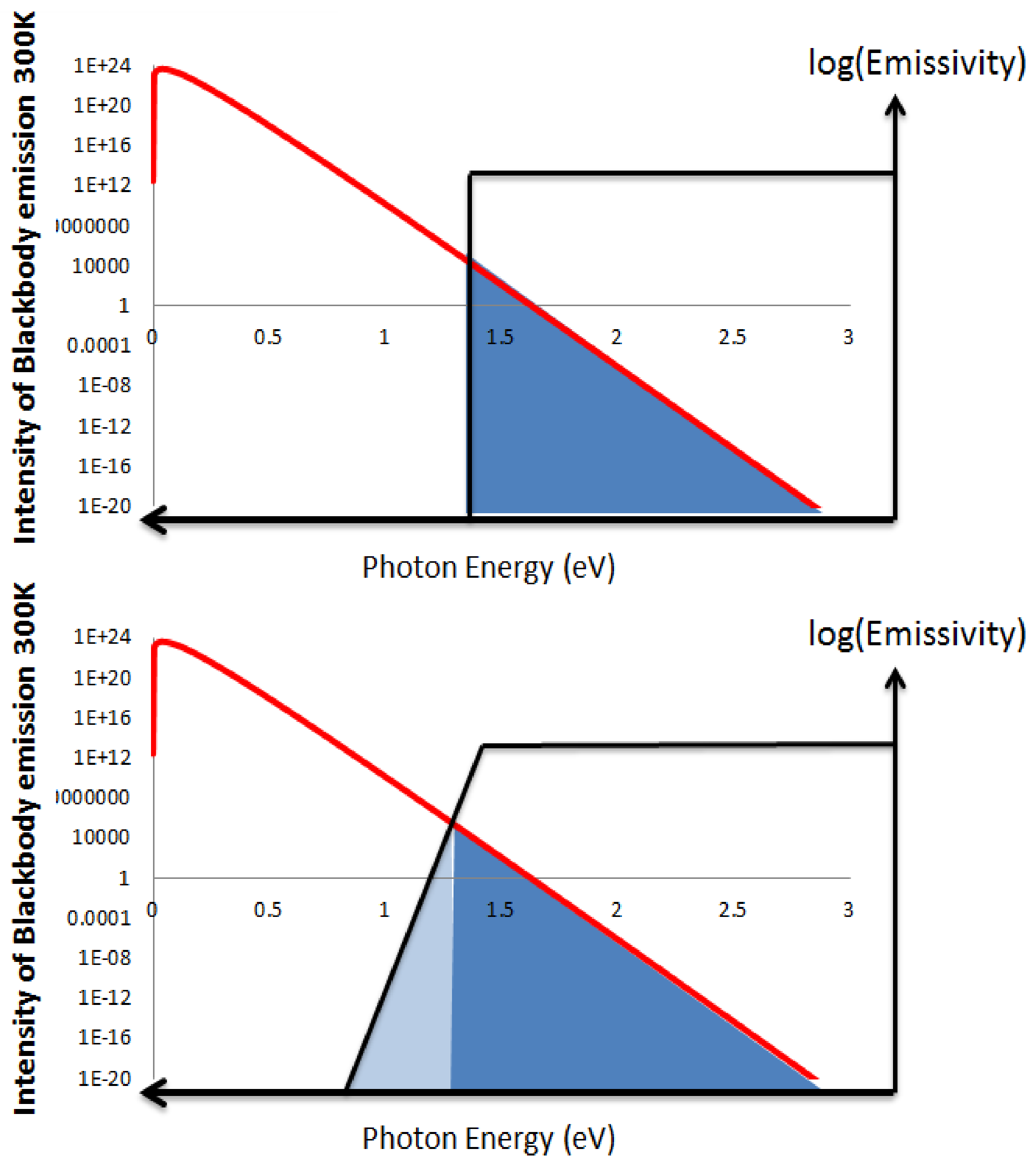

Figure 4-10: Integration of black-body radiation and emissivity that yields dark saturation current density with 1) steeply rising emission edge and 2) exponential rising emission edge

By taking into consideration an emission function with the material's tail width, we have predicted a much larger dark saturation current J_0 for QD device (E_U=50

meV) compared with bulk GaAs (E_U=13 meV). The results are summarized in Table 4-3. Voc can be even higher than what the SQ theory predicts if photon recycling is introduced. For materials with a small tail width such as GaAs, the limiting efficiency is very close to that predicted by the SQ model. However, for QD devices, our model with the band tail effect is a better assessment of the conversion efficiency. For other materials such as CIGS and Si, poly-Si and so on, the tail width is an intrinsic parameter just like the value of the material. Our proposed model serves as a better guidance for practical implementation of solar cells with new materials.

To include the effect of both the wetting layer and the QDs on the device's emissivity, we have integrated our previously derived absorption coefficient curve with a 300K blackbody radiation spectrum. By making the radiative limit assumption, we have obtained a Voc around 1.006V. In a QD device, due to an important non-radiative recombination contribution, the Voc will be further reduced.

The tail also affects the overall generated photocurrent since it changes the spectral response of the device to the solar radiation. By modeling the solar radiation as a black-body radiator operating at 6000K, we can compare the theoretical value of the predicted photocurrent under 1 sun condition with or without the intrinsic bandtail. The semilog plots with 6000K blackbody radiation are shown in **Error! Reference source not found.** for clarification purpose. As an been seen, a slight enhancement of photocurrent is expected.

Table 4-3: Summary of the devices with step-like absorption edge, a 13 meV tailing width and a 50 meV tail width.

Devices	Width of tailing states (E_U) (meV)	Calculated Voc (V)	Experimental-best Voc (V)
Device with step-like absorption	0	1.160	NA
Best Bulk GaAs device	13	1.155	1.120 (Green et al., 2014)
QD device	50	1.006	0.780 [2]

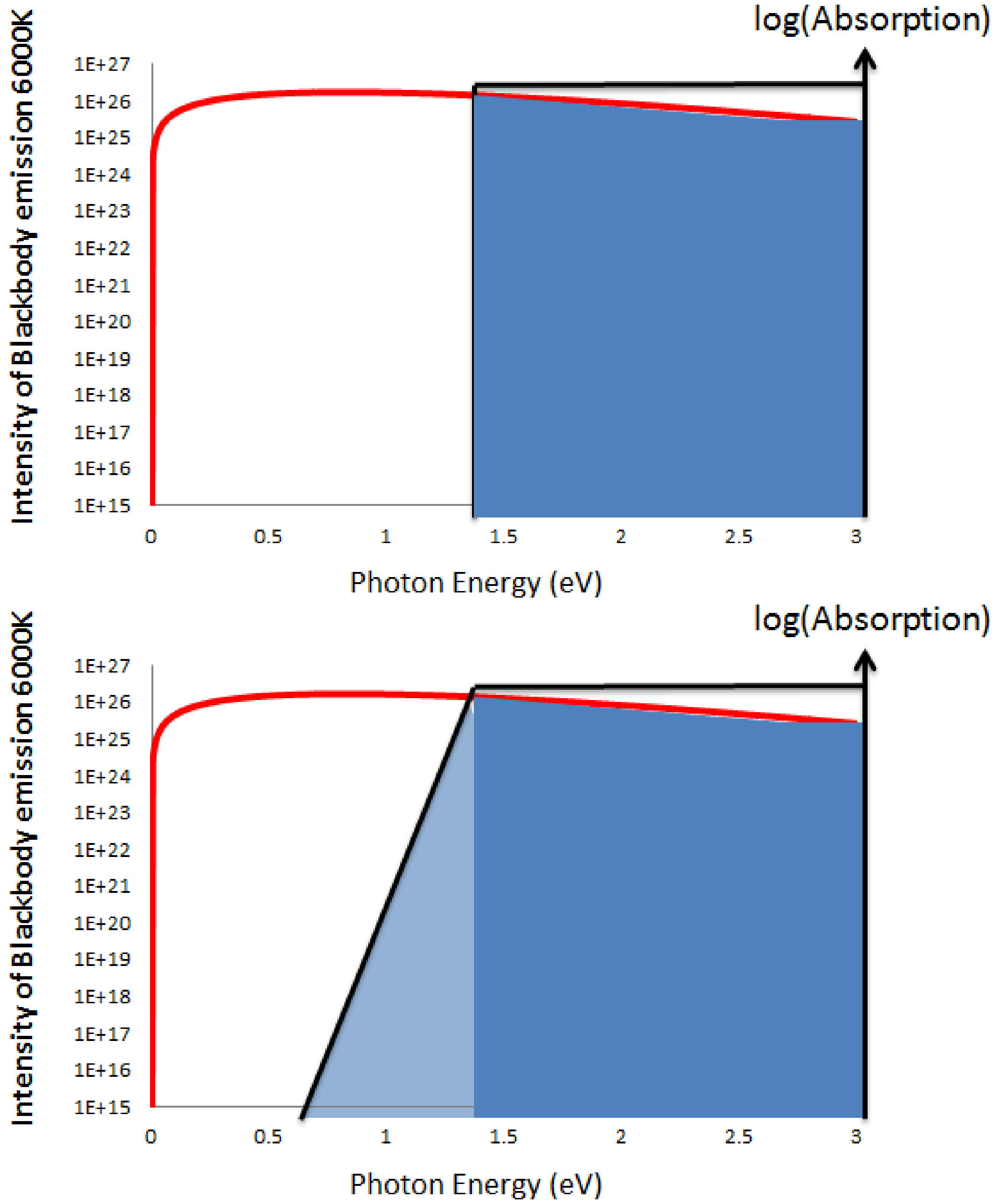

Figure 4-11: Integration of black-body radiation of the sun and absorptivity that yields light-generated current density with 1) steeply rising absorption edge and 2) exponential rising absorption edge.

Experimentally, we have measured a photocurrent density of around 24.6 mA/cm^2 for a QD sample with a tail width of 50 meV compared with 23.4 mA/cm^2 for a bulk sample with a tail of 13 meV. There is an enhancement of 5%. Most of this measured Jsc enhancement comes from the enlarged integration area with a more extended tail, via a one-photon absorption process, with the rest contributed by the wetting layer and the QD absorption.

To conclude, we have developed a modified Shockley-Queisser model that includes the material's intrinsic tail width to predict the solar cell's open circuit voltage and short circuit current. The existence of extended tailing states contributes to an enhancement of the dark saturation current and leads to a fundamentally reduced Voc.

4.8.1 Comparison of the width of the tailing states from an EQE measurement between InAs/GaAs QDs and $In_{0.5}Ga_{0.5}As$/GaAs QDs

We have used two sets of QD devices. One is the InAs/GaAs QDs and the other is the $In_{0.5}Ga_{0.5}As$/GaAs QD device. Their QD densities are similar. The most distinctive difference between these two samples is the composition of the QDs. The lattice constant difference at the interface of InAs/GaAs quantum dots is 5.6%, while at the interface of $In_{0.5}Ga_{0.5}As$/GaAs it is obviously less. Consequently, the InAs/GaAs QDs creates more disruption to the crystal potential

of the matrix material, and should induce a much more extended Urbach tail compared with $In_{0.5}Ga_{0.5}As$/GaAs QDs. To suppress the width of the tail, many other techniques can be used including incorporating a strain compensation layer. We will discuss the results of the samples reported by others later.

We have used an EQE measurement to reveal the distribution of the tailing states with respect to the position of the QD and WL transitions. It reveals the process of optical absorption from the valance band to the QD states and the sequential carrier extraction process to the external circuit. From a careful fitting to the below bandgap absorption, we have derived a tail width around 50 meV for InAs/GaAs QDs and round 30 meV for $In_{0.5}Ga_{0.5}As$/GaAs QDs, shown respectively with the doted curves in Figure 4-12.

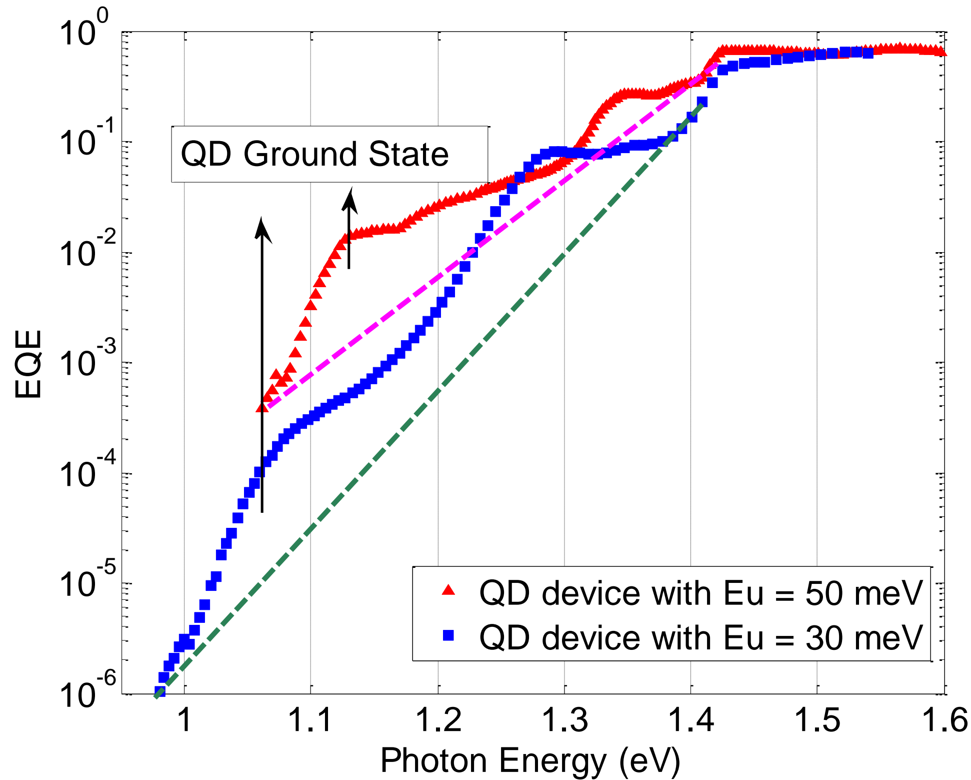

Figure 4-12: Semilog EQE plot to extract Urbach energy for InAs/GaAs QD device and $In_{0.5}Ga_{0.5}As$/GaAs QD device

4.8.2 The effect of tailing states on the carrier relaxation process

With a more broadened tail, the device's Voc will be more severely degraded. An absorption tail is at the same time an emission tail. The dark current density can be expressed as an integration of 300K blackbody radiation spectrum and the device's emission function. A larger emission tail would increase the integration area and result in a larger dark current density. Voc is reversed correlated with dark current. Consequently, a lower Voc should be expected with devices of a

wider tail. More details in the derivation can be found here. Experimentally, we have measured a Voc of 0.78 V for QD device with Eu = 50 meV and 0.89 V for the QD device with Eu = 30 meV.

Carriers can relax through a continuum background, the mechanism of which was first observed by Toda(Toda et al., 1999). When the tail is greatly extended in the case of InAs/GaAs QD device, the carriers can relax to the lowest level of QDs quickly before they recombine. Thus only one peak in PL that is centered around the QD ground level is observed, and is shown in Figure 4-13. For $In_{0.5}Ga_{0.5}As$/GaAs QD device, the tail itself is much narrower. The background continuum states have a much lower density around the QD energy levels, which greatly affect the carrier relaxation process to the QD states. As can be seen in Figure 4-13, the PL shows two peaks in the $In_{0.5}Ga_{0.5}As$/GaAs QD device. The carriers generated above bandgap relax much more slowly due to a lack of an efficient carrier relaxation pathway. Consequently, at room temperature, carriers partially recombine at the wetting layer energy states and partially relax to the QD ground states and then recombine. Many have reported on the difficulties of observing photon bottleneck in a QD device under cryogenic temperature, we suggest that it might be attributed to the coupling effect between the background continuum states and the quantum confined states.

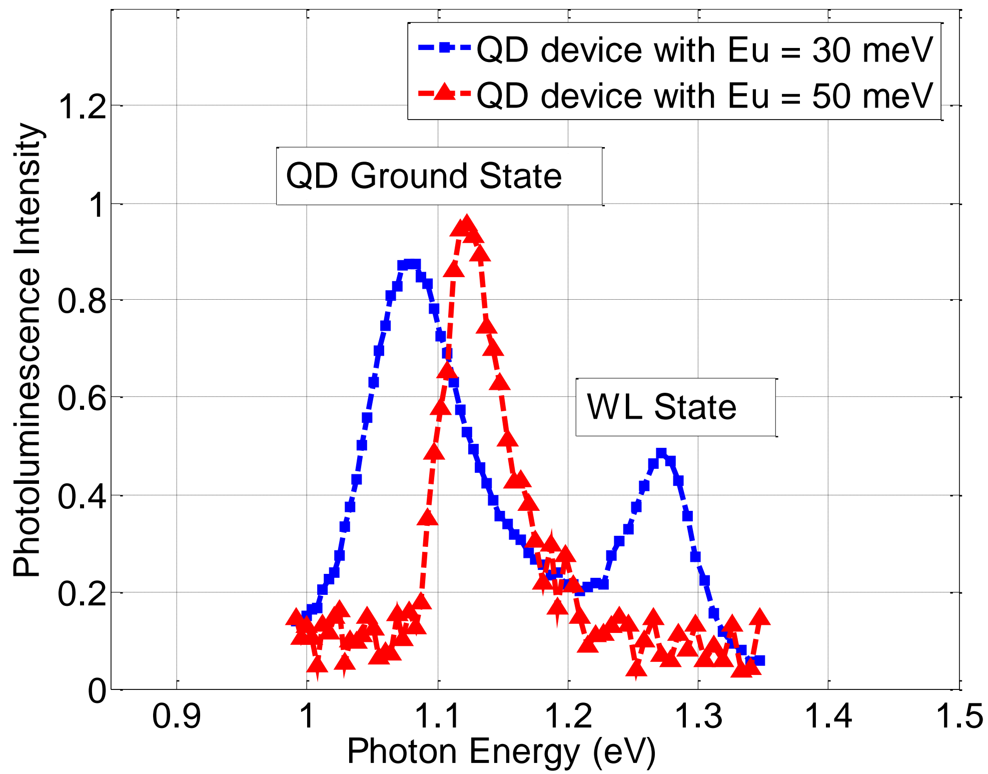

Figure 4-13: Photoluminescence measurements for InAs/GaAs QD device and $In_{0.5}Ga_{0.5}As/GaAs$ QD device

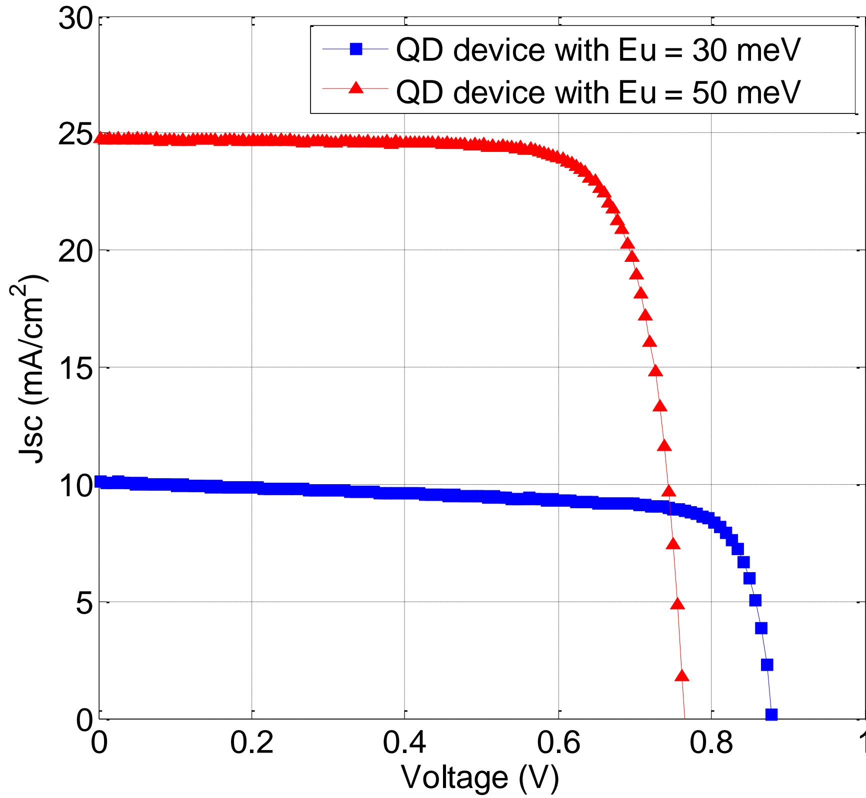

Figure 4-14: IV performance comparison for InAs/GaAs QD device and $In_{0.5}Ga_{0.5}As$/GaAs QD device

In order to verify the correlation between PL results and the tail width, we have also compared the performance of the QD devices reported by others. The results are summarized in Table 4-4. As can be seen, for QD devices with 2 PL peaks, the Voc is generally high ranging from 0.84 V to 0.99 V. For QD devices with only 1 PL peak centered around the lowest QD level, Voc is generally much lower ranging from 0.616 V to 0.78 V. It is worthwhile noting that fabrication

error exists when comparing results from different groups. However, the general trend can be clearly observed for sure that 2 peaks in PL correspond to a higher Voc. Even the respective peak intensity ratio at the wetting layer and the QD ground state should indicate a slight difference in Voc. By looking closely at the devices reported by Bailey et al, for device with the main peak at QD state, the Voc is 0.88 V. For devices where the main peak is centered at the wetting layer, most carriers tend to recombine at the wetting layer state before relaxing to the QD states. Voc is then much higher (0.99 V). In order to achieve a high Voc, the authors have incorporated strain compensation layers so potentially a very narrow tail width has been achieved.

Table 4-4: Performance comparison among our QD devices

	Urbach energy	Trapping effect	Voc
This work	50 meV	1, at QD ground state	0.78 V
(Laghumavarapu et al., 2007)	NA	1, at 1300 nm	0.72 V
(Sugaya et al., 2012b)	NA	1, at 1000 nm to 1020 nm	0.616 V to 0.78 V
This work	30 meV	2, main peak at QD state	0.89 V
(Bailey et al., 2011)	NA	2, main peak at QD state	0.88 V
(Bailey et al., 2011)	NA	2, main peak at wetting layer	0.99 V

4.8.3 The effect of tailing states on the carrier collection process

Besides functioning as a carrier relaxation pathway, the background continuum tailing density of states can also function as a carrier extraction pathway. We have shown in one of our papers that the QDs can function as electron traps. The band offset between InAs and GaAs is mainly at the conduction band side. Under room temperature, holes energy states can be seen as thermally connected. Thus only electrons can be effectively trapped.

When electrons are trapped in the quantum dot states, they can release their excess energy by emitting a photon. This photon is not reabsorbed since the absorption coefficient at the QD ground state energy is small (of order 100 cm^{-1} or less). The tail contribution to EQE around the $In_{0.5}Ga_{0.5}As$/GaAs QDs ground state is as low as 5×10^{-6} compared with 2×10^{-3} for the highly strained InAs/GaAs QD device. This significant difference strongly indicates that the density of states of the continuum background around the ground state energy in the $In_{0.5}Ga_{0.5}As$ QDs is much less. Thus the carrier extraction from the QD confined states is much easier for the device with a higher density of background continuum states. The QD trapping effect will be more severe since the electrons at the quantum dot states are more difficult to be collected due to a lack of an efficient collection mechanism. Experimentally, we have measured a Jsc of only 10 mA/cm^2 for $In_{0.5}Ga_{0.5}As$/GaAs QD devices that is much lower than the InAs/GaAs QD device potentially due to a more severe mobile electron trapping effect.

5 Investigation of Non-linear Sub-bandgap Photocurrent Generation and its implication in the realization of the intermediate band solar cell concept

5.1 Current status of non-linear properties in QD solar cells

The concept of Intermediate Band Solar Cell (IBSC) aims at covering a wider range of the solar spectrum by generating extra photocurrent with sub-bandgap photons. We believe a fundamental approach for realizing the enhancement of Jsc of IBSC without reducing the energy separation between electron and hole quasi Fermi levels (leading to a low Voc) is via a two photon absorption (2PA) process. However, up till now, few measurements have been made of the 2PA contributed carrier generation efficiency (Mart íet al., 2006).

The essence of the idea behind IBSC is to facilitate two sequential photon absorption so that two sub-bandgap photons can contribute to one free electron-hole pair, generating a higher short circuit current density than its bulk solar cell while maintaining the separation of the electron and hole quasi-Fermi levels. The design of a successful IBSC should be governed by the selection of a material system facilitating a two-photon absorption process. A major limitation of the

present characterization method of sub-bandgap photocurrent generation is that it cannot distinguish the 2PA current from the 1PA current via the energy states within the gap, which is also responsible for the Voc degradation. In other words, a high Jsc QDs cell is not necessary a good candidate for an IBSC working toward the realization of 63% high efficiency cell. Despite of its significance, till now, the non-linear effect of such system including the 2PA process has not been studied yet in detail.

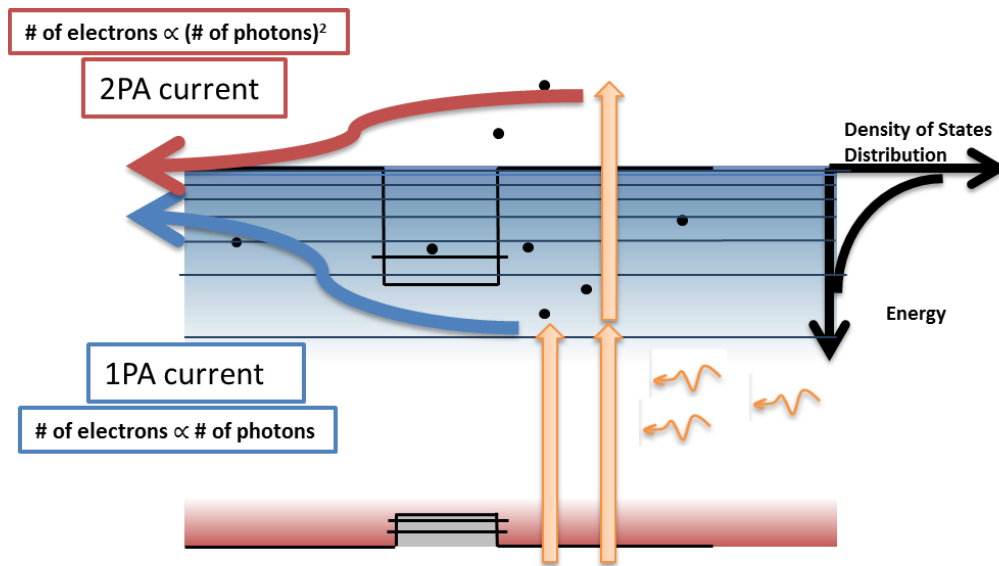

Figure 5-1: One low energy photon excites electron from the valance band to the below-bandgap tailing density of states while the tail also functions as a collection pathway so that the carriers that are generated by this 1PA process can be detected. Meanwhile, the tailing density of states can also act as an intermediate level to facilitate a two photon absorption (2PA) process. The electrons that are excited by a 2PA process leading to the generation of an electron-hole pair that

will thermalize to the bandedge and will be detected as the 2PA contributed photocurrent.

5.2 Non-linear properties in QDSC for off-resonant excitation

Here we demonstrate a method to evaluate the 2PA carrier generation efficiency and the absorption saturation effect of QDs, overcoming the limitation of the information given by the photocurrent spectral response measurement. A cleaved sample was fabricated with back side n-type Au/Ge/Ni/Au electrode and top p-type Ti/Pt/Au interdigitated figure-shaped electrode. In order to observe the nonlinear optical transitions via the intermediate states, high intensity radiation beams with different wavelengths were used. Off-resonance excitation and on-resonance excitation were studied using the single mode pigtailed laser LPS-1060-FC from Thorlabs operating at 1064 nm and 1550 nm laser from Ortel Corporation connected to an Erbium Doped Fiber Amplifier. The laser beam were first collimated and then focused tightly to a waist of 4.5 μm. The output power was calibrated with an unbiased Ge detector. The device is mounted perpendicularly to the beam on a three dimensional stage with motorized actuators from Newport. The photocurrent was read with a Newport 6487 Picoammeter. By forcing the light in the light propagation direction, the incident photon intensity on the sample changes as illustrated in Figure 5-2. The photocurrent dependence on incident photon intensity can thus be evaluated by varying the sample's position in the propagation direction.

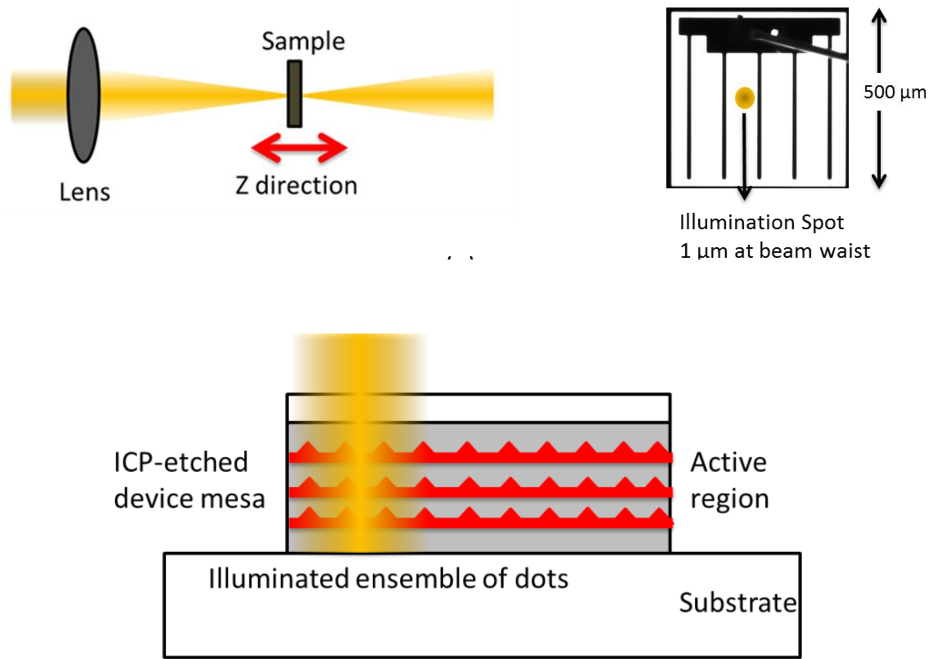

Figure 5-2: Z-scan configuration of fabricated quantum dot device

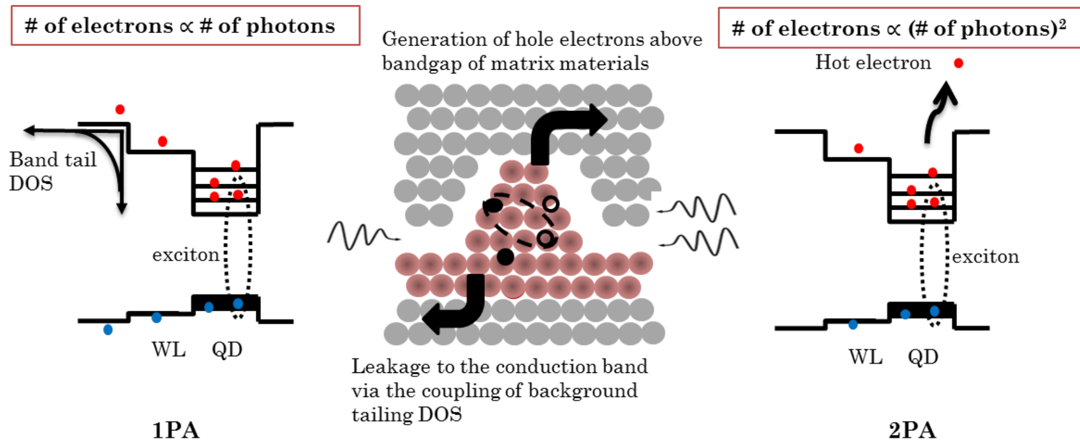

Figure 5-3: A sub-bandgap photon generates an electron on the energy states within the gap. The free electron will either leak to the matrix via a continuum tailing DOS (1PA process as shown on the LEFT side) or be excited again by a

sequential absorption of another sub-bandgap photon (2PA process as shown on the RIGHT side).

In InAs/GaAs QDs, the electrons will be pumped by a sub-bandgap photon to an intermediate state. Then it will either be extracted directly or be pumped optically to conduction band by absorbing another photon. If the carriers are directly extracted to the external circuit, they are generated via a single photon absorption process (1PA). If they are pumped again by another photon and then collected, they contribute to the overall photon-generated current by a two-photon absorption process (2PA). In order to investigate the operation of the quantum dots solar cell and understand the nonlinear effect for sub-bandgap photocurrent generation, we have constructed a 2PA model that operate at room temperature. Room temperature is the most common and applicable condition for solar cells.

To model the nonlinear optical interaction, the laser beam, with a Gaussian intensity profile, is described by the following expression:

$$I(r,z) = I_o\left[\frac{w_0}{w(z)}\right]^2 e^{-\frac{2r^2}{w(z)^2}} \qquad 5.1$$

where $\mathrm{r} = \sqrt{\mathrm{x}^2+\mathrm{y}^2}$, $\mathrm{w(z)} = \mathrm{w}_0\sqrt{1+\left(\frac{\mathrm{z}}{\mathrm{z}_0}\right)^2}$, I_0 is the intensity at $\mathrm{z} = 0$ and $\mathrm{r} = 0$. w_0 is the beam waist (1.5 μm) which is measured using a knife edge method and z_0 is given by: $z_0 = \frac{\pi {w_0}^2}{\lambda} = 4.56$ μm. The total light power is given by: $P_{total\ light\ power} = I_o\left[\frac{w_0}{w(z)}\right]^2\int_{-\infty}^{\infty} e^{-\frac{2x^2}{w^2}}dx\int_{-\infty}^{\infty} e^{-\frac{2y^2}{w^2}}dy = \frac{\pi}{2}I_0{w_0}^2$. The 1PA

is related to the available number of states and the excitation intensity. If the available state density stays constant during the measurement, the 1PA process should generate a constant number of electrons that is only dependent on the total beam power, while the 2PA process will have a quadratic dependence on light intensity. The total detected current is the sum of the single photon (1PA) and the two-photon absorption process (2PA) as expressed below:

$$i_{1PA+}i_{2PA} = i_{total} \quad 5.2$$

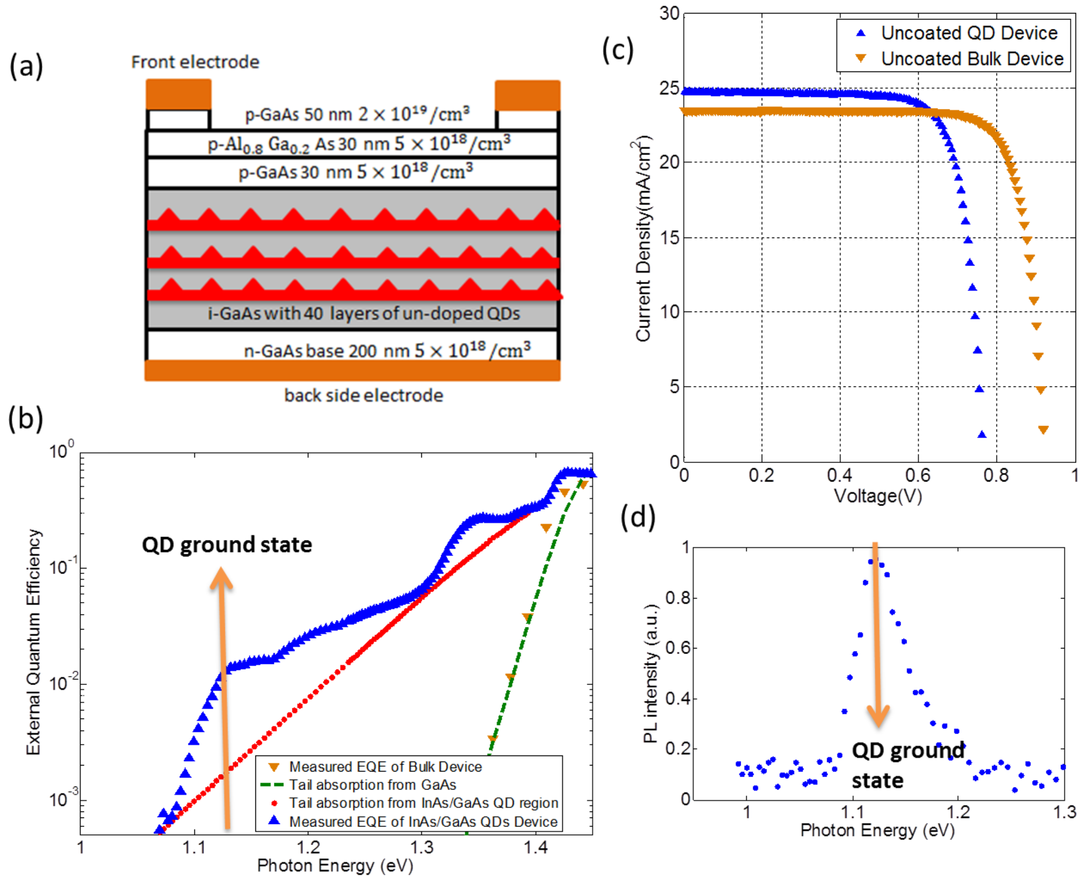

Figure 5-4: (a) Diagram of quantum dots solar cell (b) The position of the tailing states for both the QD device and the bulk GaAs device (c) Current-voltage

characteristics and (d) Photoluminescence measurement with one peak centered around QD ground state 1.12 eV.

From an external quantum efficiency measurement or a photoluminescence measurement, we have located the lowest energy level of the InAs/GaAs quantum dots to be around 1.12 eV. The photons with wavelength of 1550 nm and energy of 0.8 eV excite carriers to the states below the confined quantum states. Then electrons can be collected through the continuum tailing states or can be excited again into the conduction band. The 1PA current only depends linearly on the total beam power (assuming no heating effect) and is described by the equation below:

$$i_{1PA}(z) = a\int_0^\infty I(r,z)dA = a\int_0^\infty I_o\left[\frac{w_0}{w(z)}\right]^2 e^{-\frac{2r^2}{w(z)^2}}2\pi r dr =$$

$$aI_o\left[\frac{w_0}{w(z)}\right]^2\int_0^\infty e^{-\frac{2x^2}{w(z)^2}}dx\ \int_0^\infty e^{-\frac{2y^2}{w(z)^2}}dy = \frac{\pi}{2}aI_0{w_0}^2 \qquad 5.3$$

The coefficient ***a*** here describes the *linear responsivity* of the detection process with the wavelength of 1550 nm.

Meanwhile, the 2PA process has a quadratic dependence on the intensity. It can be described by the following expression:

$$i_{2PA} = \mathrm{b}\int_0^\infty [I(r,z)]^2 dA = \frac{\pi}{4}b\frac{{z_0}^2{I_0}^2{w_0}^2}{{z_0}^2+z^2} \qquad 5.4$$

where b is a constant value indicating the efficiency of the 2PA process. The total photocurrent i_{total} can be described as a sum of the 1PA and 2PA processes as:

$$i_{total} = \frac{\pi}{2} a I_0 {w_0}^2 + \frac{\pi}{4} b \frac{{z_0}^2 {I_0}^2 {w_0}^2}{{z_0}^2 + z^2} = \frac{\pi}{4} I_0 {w_0}^2 \left(2a + \frac{b I_0 {z_0}^2}{{z_0}^2 + z^2}\right) \qquad 5.5$$

At the beam waist, where z=0, $i_{total} = \frac{\pi}{4} I_0 {w_0}^2 (2a + bI_0)$.

A plot of the total measured photocurrent along the z axis under 1550 nm radiation is shown in Figure 5-5, and clearly exhibits a non-linear response to the incident photon intensity. The resulting photocurrent agrees perfectly well with a Lorentzian fit in the propagation direction (as described by Equation 5.4). If we plot the 2PA contributed excess photocurrent by subtracting the baseline reading from the maximum reading along with the square of the total radiation power, an exact quadratic dependence can be extracted. A slope of 0.0101 nA/mW^2 can be fitted, and a 2PA non-linear responsivity of 0.071 nA ·μm^2/mW^2 (the value of ***b***) can be extracted accordingly. From our method, the 2PA coefficient β_{2PA} can be directly derived by relating the derived ***b*** value with the introduction of the responsivity factor R for 0.8 eV

$$b = \beta_{2PA} \times L \times R \qquad 5.6$$

where L is the effective thickness of the absorption region and R describes the amount of generated electrical charges per incident photons. Taking the photon energy as 0.8 eV, and assuming an internal quantum efficiency of 100%, R can be calculated as:

$$R = \frac{e}{2\times 0.8\ eV} \eta_{int} = \frac{1.6\times 10^{-19} C}{2\times 0.8\times 1.6\times 10^{-19} J} = 6.25\times 10^5\ \frac{nA}{mW} \qquad 5.7$$

Thus β_{2PA} is extracted to be 5.7 cm/GW under 1550 nm excitation. It should be noted here that if the internal quantum efficiency is less than unity, the derived β_{2PA} shall be further inversely-proportionally increased. In comparison, for bulk GaAs device, neither the 1PA photocurrent nor 2PA photocurrent is detected with our method, meaning a much smaller 1PA and 2PA coefficient within the bulk device where the Urbach energy is as small as 13 meV(Greeff and Glyde, 1995b; Johnson and Tiedje, 1995; Li and Dagenais, 2014.). The 2PA coefficient for bulk GaAs derived by other methods such as using waveguide structure also generally shows a smaller value around 1 cm/GW(Zheng et al., 1997) (we note that the assumption of this method that the 2PA is the only non-linear effect will yield an overestimated value of the 2PA coefficient). Therefore, we conclude that the greatly broadened tailing density of states in the QD device strongly enhances both the 1PA current generation and the two-step photon absorption process by introducing the mid-gap intermediate states.

A plot of the 1PA current vs power leads to a super-linear behavior, as shown in Figure 5-5(c). A possible explanation for this deviation from the theoretically predicted linear dependence on total radiation power is probably due to a slight heating effect coming from the tightly focused laser beam. The Urbach tail energy (E_U) was found to broaden at higher temperatures(Johnson and Tiedje, 1995). When the tail extends further into the mid gap, there are more states available for low energy photon absorption. Consequentially, more generated carriers are collected via this continuum tailing density of states. The 1PA current is thus a

function of the Urbach tail width. According to the Fermi's Golden Rule, the transition rate increases as a result of an increase in the final available density of states. We note that in our method, the non-linear component of the 1PA current generation process can be explicitly distinguished from the 2PA process.

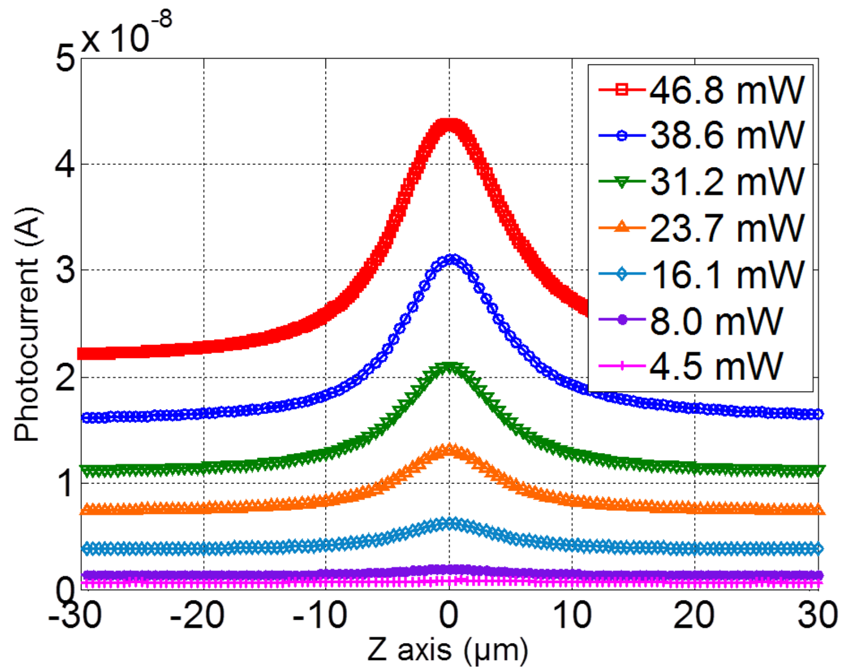

(a)

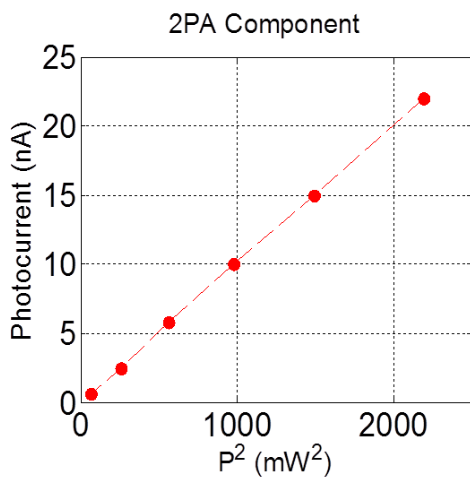

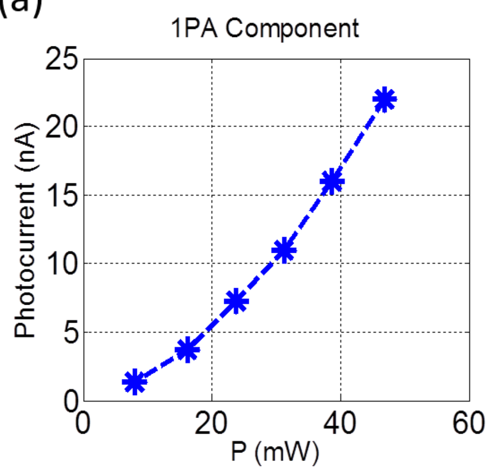

(b) (c)

Figure 5-5: (a) Photocurrent dependence along with propagation direction for ***1550 nm*** laser (b) The quadratic photocurrent plot indicating a 2PA photocurrent generation efficiency of around 0.01 nA/mW^2 (c) 1PA photocurrent generation efficiency plot with different beam power where the nonlinear component is due to local heating.

It is also interesting to study the X-Y dependence of the 1PA sub-bandgap photocurrent reading based on the carrier generation mechanism we proposed here. Using a laser beam focused to a beam waist of 1.5 um, the photocurrent is collected as we move the beam waist over the sample. We estimate the number of quantum dots contained in the beam to be around 1×10^5 dots. The 1PA reading is mostly constant when the beam moves in the X-Y plane, away from the edge of the sample. Even with uniform film quality like the devices we studied here, when the beam moves towards the edge of the device, the devices exhibit a slight enhancement of the base line reading when the beam is at the edge of the device (from 22 nA to 24 nA under an input power of 46.8 mW). This is very interesting because this technique can potentially be employed to scan the device area and generate a two-dimensional map as an indication of the Urbach energy variation (strain variation) across the device's whole active area with a spatial resolution only limited by the laser-beam radius. The derivation of the width of bandtail potentially can be used to predict the Voc degradation.

5.3 Non-linear properties in QDSC for on-resonant excitation

Since the QD ground state transition is 1.06 μm (shown in Figure 5-4 with an external quantum efficiency measurement), a single transverse mode pigtailed laser (Thorlabs LPS-1060-FC) with a wavelength of 1.06 μm is used for the on-resonance two-photon absorption measurement. The laser beam is first collimated and then focused tightly to a beam waist of 1.0 μm. The output power is calibrated with an unbiased calibrated Ge detector. The quantum dot solar cell is mounted perpendicularly to the beam on a three dimensional stage with motorized actuators from Newport Corp. The photocurrent is read with a Newport 6487 Picoammeter. With the solar cell moving along the light propagation direction, the incident intensity profile changes accordingly.

The photocurrent of the QD device comes from both 1PA and 2PA processes. The existence of an extended Urbach tail functions as an efficient carrier extraction pathway so that the sub-bandgap photons can directly contributed to the photocurrent without the aid of the second photon. This resulting photocurrent is called the 1PA contributed photocurrent. Since 1.06 μm is the transition energy from valance band to quantum dot ground states and corresponds to the on-resonant excitation, the saturation effect of quantum dots should not be neglected especially when the excitation intensity reaches a substantially high value.

The one-photon transition of the self-assembled InAs/GaAs quantum dots has an inhomogeneous linewidth because of the dot size variation. As the intensity

increases, the QD transition behaves as a saturable absorber. The dephasing time of the ground state quantum dots has previously been measured to be about 200 fs at room-temperature(Borri et al., 2001)'(Bayer and Forchel, 2002). This leads to a homogeneous linewidth of about 6 meV. Since a linewidth of 25 meV for quantum dot transition has previously been observed from our analysis of external quantum efficiency measurement, we conclude that the transition is mostly inhomogeneously broadened. As a result, the single photon absorption via quantum dots states can be expressed as an inhomogeneously broadened saturable absorbers and can be written as (Yariv, 1989):

$$i_{1PA}(z) = a\int_{-\infty}^{\infty}\frac{I(r,z)}{\sqrt{1+\frac{I(r,z)}{I_s}}}dA = a\int_{0}^{\infty} I_o\left[\frac{w_0}{w(z)}\right]^2 e^{-\frac{2r^2}{w(z)^2}} \Bigg/ \sqrt{1+\frac{I_o\left[\frac{w_0}{w(z)}\right]^2 e^{-\frac{2r^2}{w(z)^2}}}{I_s}}\, 2\pi r dr \qquad 5.8$$

The on-resonance pumping leads to absorption saturation, which can be described by a saturation intensity $\boldsymbol{I_S}$. $\boldsymbol{I_S}$ is given by $I_s = \frac{4\pi^2 n^2 hc}{\lambda^3}\Delta\nu$, where $\Delta\nu$ is the FWHM of the absorption profile And is given by $\Delta\nu = 1/\pi T_2$, where T_2 is the dephasing time.

Meanwhile, the 2PA process has a quadratic dependence on the beam intensity. It can be described by the following expression:

$$i_{2PA} = \frac{\pi}{4} b \frac{{z_0}^2 {I_0}^2 {w_0}^2}{{z_0}^2 + z^2} \qquad 5.9$$

where b is a constant value indicating the efficiency of the 2PA process.

The photocurrent plot for 1064 nm on-resonant excitation under different input beam power is shown in Figure 5-6. The photocurrent reading is a combined effect of 2PA photo-generation and absorption saturation based on an inhomogeneous broadened transition. The saturation intensity was obtained by fitting equation 5.8 to the measured photocurrent along the z direction. The fitting yields a saturation intensity $\boldsymbol{I_S}$ as high as 10 mW/µm^2, which is the intensity required in order to put half of the QD population with an electron that occupies the conduction band QD potential ground state.

Using equation 5.9, the 2PA photocurrent can be fitted with $\boldsymbol{b}$ as 45 nA ·µm^2/mW^2 under 1064 nm radiation. From our method, the 2PA coefficient β_{2PA} can be directly derived by relating the derived $\boldsymbol{b}$ value with the introduction of the responsivity factor R for 1.16 eV:

$$b = \beta_{2PA} \times L \times R \qquad 5.10$$

where L is the effective thickness of the absorption region and R describes the amount of generated electrical charges per incident photons. Taking the photon energy as 1.16 eV, and assuming an internal quantum efficiency of 100%, R can be calculated as:

$$R = \frac{e}{2\times 1.17\ eV} \eta_{int} = \frac{e}{2\times 1.17\ eV} = 4.27 \times 10^5\ \frac{nA}{mW} \qquad 5.11$$

This describes the conversion efficiency of two 1.06 µm photons generating one electron-hole pair. Consequently, β_{2PA}(1064nm) can be calculated to be 5.27 ×

10^3 cm/GW. It is **240** times larger than the reported value for bulk GaAs measured at 1.06 μm(Kadlec et al., 2004; Valley et al., 1989), which is around 22 cm/GW. Note that when the internal quantum efficiency is less than unity, the number shall further increase. Due to the existence of a continuum distribution of density of states, the two non-linear contributions were shown with different input powers in Figure 5-6 (b) (c) (d),. As can be seen, the fitting overlaps perfectly well with the measured current reading. In the Matlab program we have written, the only input variable is I_0. The prefect fittings under all input powers validate the existence of the two main non-linear components (saturation effect and 2PA component) we have considered within our QD device. Note that there might be a certain degree of non-linear thermal effect, but it is relatively small according to our fitting results.

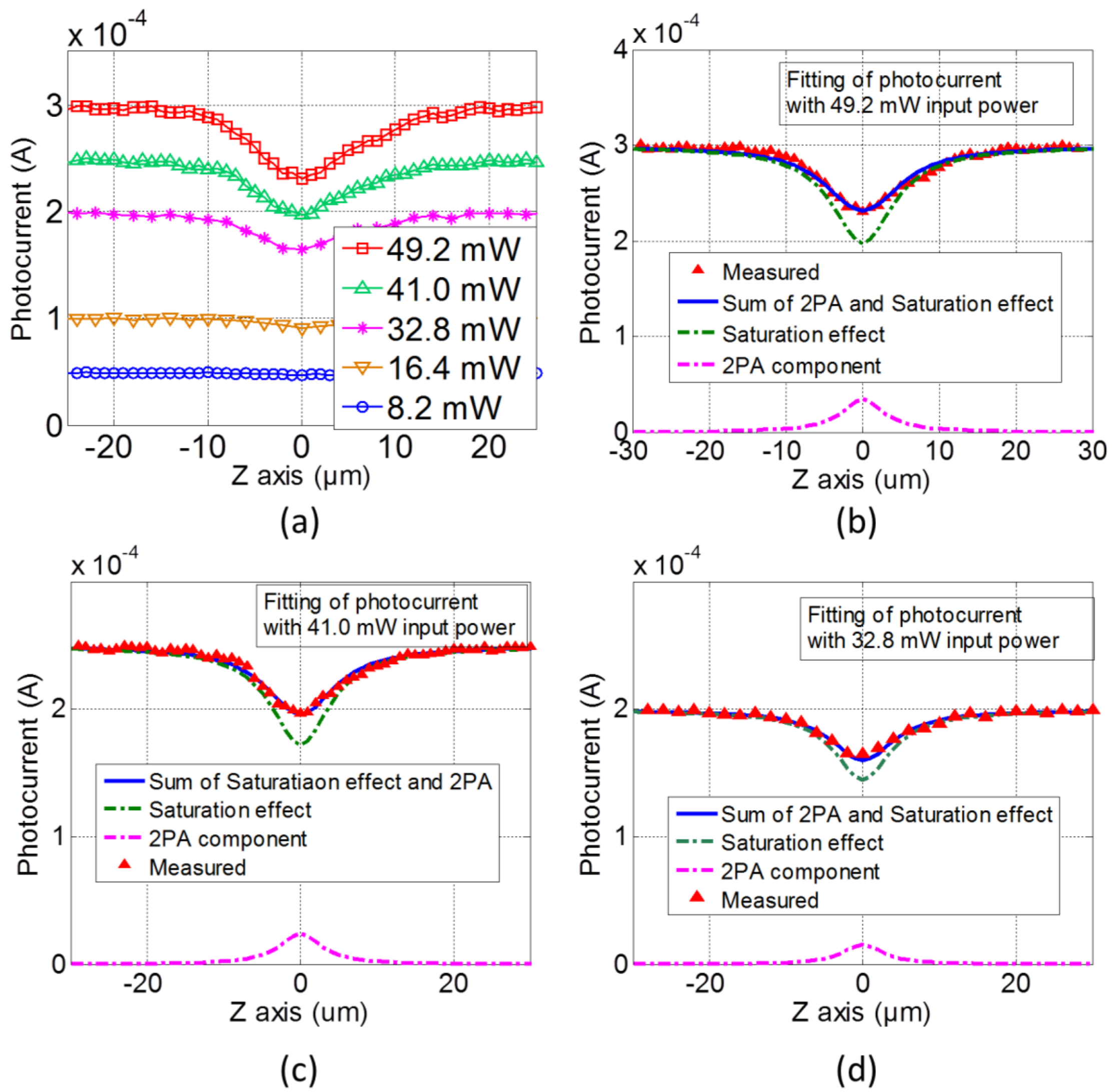

Figure 5-6: (a). QD device's response of ***1064 nm*** laser. (b)(c)(d) A comparison between fitted curve and measured data with 49.2 mW, 41.0 mW and 32.8mW input power. A saturation current density of 10 mW/ μm^2 was fitted under all input powers.

We do not think that the two-photon current component observed with on-resonance excitation is due to the confined quantum states acting as intermediate states. Due to the low density of QDs with a planar density of $4 \times 10^{10}/cm^2$and an interspacing of 50 nm, the wavefunctions of quantum dots do not overlap. Localized energy levels (bound states) are formed instead of a mini band. Because of the requirement on momentum conservation for the bound to unbound continuum states, only a small range of photon energies (generally in the range of 3 μm to 6 μm depending on the dot sizes) are allowed for the second transition to the conduction band. Due to the absence of such energy photons (the only available photons are of 1.06 μm wavelength), the associated two-1.06 μm photon absorption coefficient is expected to be small and similar to that of the bulk GaAs device. Instead, we have measured a value 240 times larger. Thus we believe that the detected two-photon absorption process mainly happens via a two-photon process involving the background tailing states. This way, the second transition is from unbound states (continuum tailing states within the gap) to unbound states (the conduction band) so that the momentum conservation rule can be satisfied. The derived high saturation intensity indicates that the intensity required to put half of the QD population with electrons in the conduction band quantum dot ground state is much higher than the solar intensity that can be generated under maximum concentration (x 46,000). It is important to put a substantial population of electrons in the QD conduction band potential in order to ensure that a second photon can be absorbed from the ground state and satisfy the momentum

conservation rule. This can only be realized by using IR photons for the second transition. Since only a small range of IR photon energies can be used for the second photon, it is not possible to generate comparable photocurrent by using two sub-bandgap photons to the one-photon photocurrent being generated from the band-to-band transition. On the other hand, when the QDs are populated with electrons, the transition rate from the valance band to QD states will be reduced substantially as a direct consequence of the Pauli Exclusion Principle. We have shown these results in our previous work (Li, Dagenais, et al., 2015).

5.4 Characterization of signal generated with second transition via IR absorption and its implication in the realization of IBSC model

Room temperature is the most common operation condition for solar cells. We tried to detect the photocurrent signal of the doped QD device under IR excitation. However, we found that no signal could be detected even with good device shielding from surrounding E&M noise and long integration time. A possible reason is that the signal under IR excitation is very small and even comparable to the thermal noise of the QD device itself under room temperature. In order to quantify the amount of current generated by the transition from QD states to the conduction band, we have setup a liquid nitrogen measurement system to evaluate the current generated with a 4e/dot InGaAs/GaAs QD devices under IR excitation.

We have used a ST-500 cyrostat from Janis, with FTS-ST-25 transfer line inserted into a 10 liter liquid nitrogen dewar. The electrical signal is extracted via two vacuum wires. The IR light source is a blackbody emitter SLS202 from Thorlabs with a maximum power at λ=1.5 μm that extends up to 5.4 μm. Since the first transition from the valance band edge to quantum dot states is around 1 eV, we have used a 2.4 μm long-pass filter to make sure that the contribution from below 2.4 μm light has been excluded. The light has been focused on to the IR window of the cryostat with a ZnSe focus lens and a CaF_2 transmission window. The estimated power of the IR light at the surface of the QD device is averaged to be 6.5 mW with a spot size (full width of $1/e^2$ in power) of roughly 4 mm.

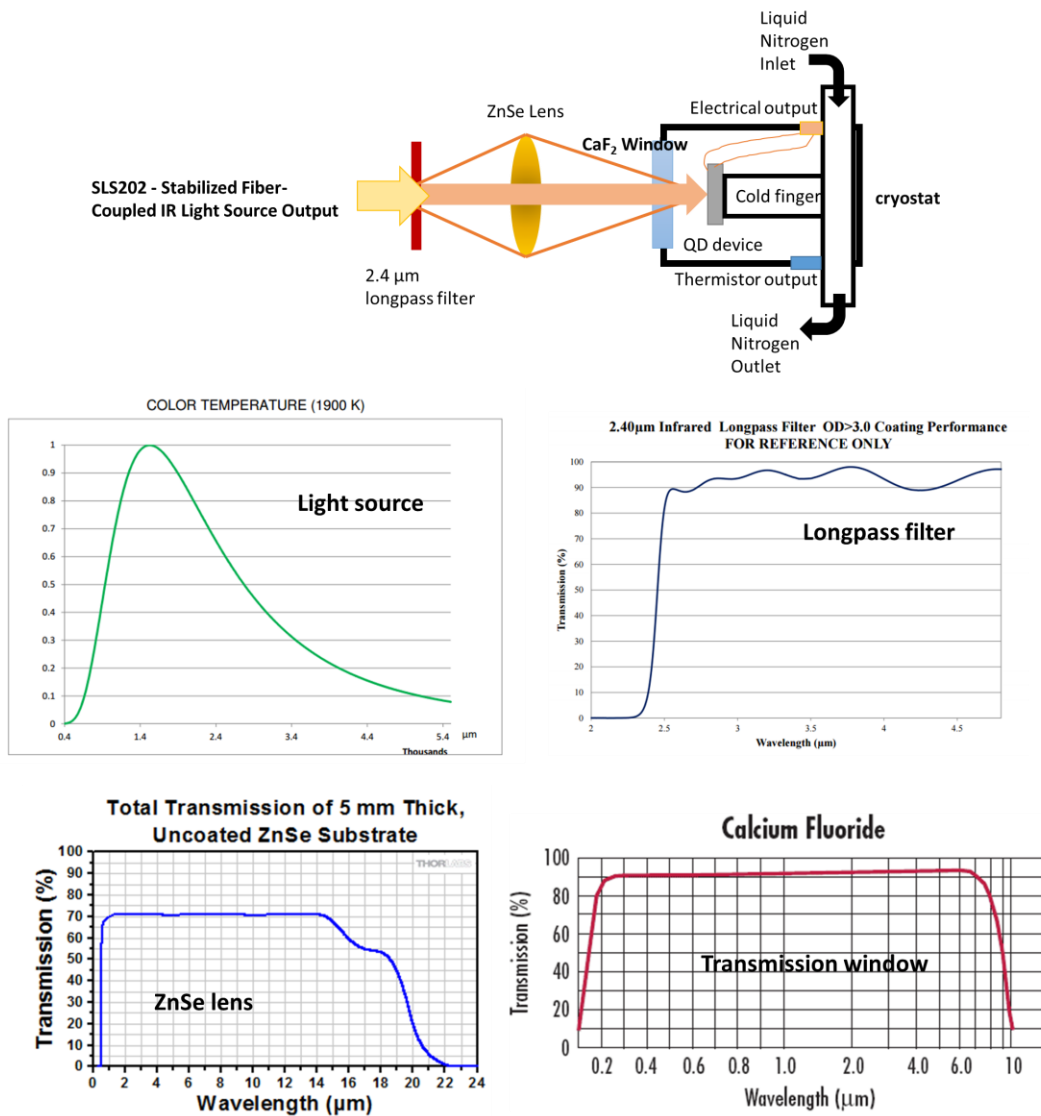

Figure 5-7. Liquid nitrogen setup for low temperature IR response measurement

Here list the operation steps for low temperature device measurement with liquid Nitrogen:

1. Pump the cryostat with turbo pump.
2. Before connecting the transfer line, make sure the transfer line has been pumped down and sealed well to avoid any leakage.

3. Fill the dewar with liquid nitrogen (available at physics receiving). Connect the adapter to the dewar. Close the pressure control valve.
4. Insert the withdrawal tube into the adapter. Let the tube reach the bottom of the dewar. Avoid hitting the bottom and don't subject the dewar to vibration or shock.
5. The pressure reading from the pressure gauge will increase from 0 to 1 psi rather quickly. Then the pressure will increase more slowly.
6. When the pressure rises to 2 psi. Open the flow valve regulator on top of the withdrawal tube. The outlet end should have cold Nitrogen gas coming out. The pressure of the dewar will keep increasing.
7. If the pressure increases to more than 3 psi. Release the pressure of the dewar by slowly opening the pressure control valve on the adapter. Let the liquid nitrogen keep flowing until there is liquid coming out.
8. Before inserting the transfer line into the cryostat, reduce the pressure to around 1.5 psi.
9. Monitor the resistance change of the thermistor, the reading should increase from 127 Ohm (room temp) to 381 Ohm (77K).
10. When finished, close the flow valve regulator. Open the pressure control valve to release the pressure. Always make sure the cryostat is at room temperature and the valve to the cryostat is open before connecting the pump.

The lock-in amplifier was connected with a chopping frequency of 283 Hz. The current-voltage pre-amplifier is connected with the output current signal. The

output of the pre-amplifier is connected to the signal input of the lock-in. We have used an integration time of 30 s to ensure the accuracy of the signal. When the IR light is off, a reading of 0.2 pA is observed. Noise is represented as varying background signal at all frequencies. The observed 0.2 pA is the noise that the lock-in amplifier picked up from the surroundings. When the IR light is on, a reading of 3.2 pA is observed. We have used a broadband IR source which is a blackbody emitter centered at 1900K to provide a continuous infrared light spectrum. With an input light power of around 6.5 mW with a coverage ranging from 2.4 μm to 5 μm, the total response of the 4e/dot device is only as small as 3 pA.

Using the QD samples from Australia, the valance band to QD ground state transition is 1.07 eV. Valance band to wetting layer transition is 1.3 eV. The bandgap of n-GaAs is around 1.41 eV. Taking the valance band offset to be 0.1 eV, we are expecting the energy separation between QD ground state and the wetting layer energy state to be 0.24 eV which is 5.17 um and the QD ground state to the conduction band minimum to be 0.35 eV which is 3.54 um. We have utilized a broad IR source ranging from 2.4 μm to 5 μm and have observed a response of 3 pA with around 6.5 mW light power. From section 4.6, we know that under one sun condition, the QDs produce a photocurrent via the transition from VB to QD states of around 12.35 $\mu A/cm^2/\mu m$ (2 μm thick QD region contributes to 19% of the extra photocurrent 1.3 mA/cm^2 measured from QD device compared with that of the bulk device). According to Figure 4-7, the

absorption spectrum coverage for transition from valance band to QD states is from 1.1 eV to 1.3 eV. The sun intensity at this range is calculated to be 11 mW/cm^2. The responsivity under room temperature is calculated to be $\frac{12.35\ \mu\text{A/cm}^2/\mu\text{m}}{11\ mW/\text{cm}^2} = \mathbf{1.12}\,\frac{\boldsymbol{\mu A}}{\boldsymbol{mW}}$ per 1 μm thick QD region (50 nm interlayer spacing)**.**

In comparison, under an IR source with input power of 6.5 mW and a spot size of 4 mm, only 1.48×10^{-4} μA/cm^2/μm can be produced via the transition from intermediate band to conduction band. The responsivity for this transition is estimated to be $\frac{1.48\times10^{-4}\ \mu\text{A/cm}^2/\mu\text{m}}{202.6\ mW/\text{cm}^2} = \mathbf{7.3} \times \mathbf{10^{-7}}\ \boldsymbol{\mu A/mW}$ per 1 μm thick QD region (50 nm interlayer spacing)**.**. Note that the IR signal can only be detected under cryogenic temperature. There is already **a mismatch factor of $\mathbf{1.5} \times \mathbf{10^{6}}$ between the two transitions**.

We have proved that the QD states to conduction band transition is too small to be able to produce a matching carrier flow from QD state to conduction with that from valance band to QD states, even under cryogenic temperature. It is fundamentally impossible to realize the intermediate band model utilizing self-assembled InAs/GaAs QDs.

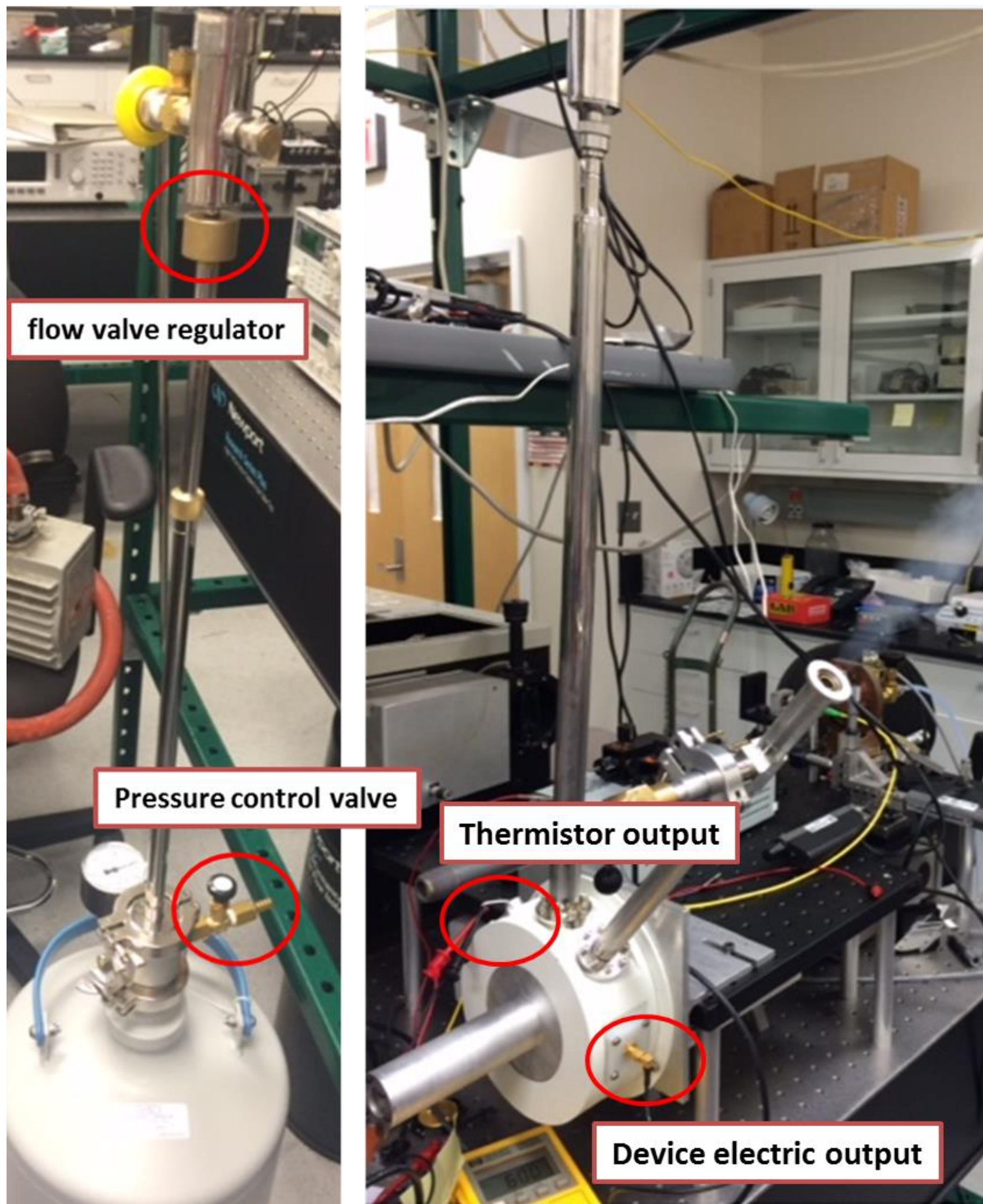

Figure 5-8: Low temperature IR response setup

6 Electron trapping properties of QDs and the electron-doping effect

The self-assembled $In_{0.5}Ga_{0.5}As/GaAs$ QDs solar cells were grown on n-GaAs substrate by metal organic chemical vapor deposition (MOCVD). The undoped QDs structure consists of n^+-doped substrate, n^--GaAs base layer, ten layers of 6 monolayers of $In_{0.5}Ga_{0.5}As/GaAs$ QDs separated by 50 nm of undoped GaAs barrier with a dot density of $\sim 4.5\times 10^{10}$ cm^{-2}, a p-$Al_{0.45}Ga_{0.55}As$ window and terminated with a p^+-doped GaAs contact layer. For the doped QDs solar cell, Si dopants are placed within a 4 nm thick GaAs barrier layer that is 10 nm below each QD layer, with a dopant sheet densities of $\sim 9\times 10^{10}$ cm^{-2} and$\sim 1.8\times 10^{11}$ cm^{-2} to provide ~2 and ~4 electrons per dot.

All samples were fabricated with Ti/Pt/Au p-type and Au/Ge/Ni/Au n-type ohmic contacts. The fabrication details can be found in Chapter 2. After metallization, the top 100nm p^+ GaAs contact layer was carefully removed with a slow etching recipe (citric acid and hydrogen peroxide mix). A thin layer of GaAs was deliberately left un-etched to protect the $Al_{0.45}Ga0_{.55}As$ layer from oxidizing. Devices were characterized without anti-reflection coatings to ensure accurate spectral response. Each device is electrically isolated via Induced Coupled Plasma (ICP) etching.

Standard solar cell characteristics were tested by an Oriel solar simulator. The external quantum efficiency (EQE) measurement was performed with the same setup described before. For the photoluminescence (PL) measurement, the same light source was used with a 950 nm long pass filter in order to eliminate the second order grating effect. The emitted photons were collected through the spectrometer and detected with the same Ge detector. We have also utilized a 1310 nm laser to accurately measure the linear photocurrent response and further evaluate the background density of states below the QDs ground states.

6.1 The impact of electron delta doping to quantum dots on short circuit current density

The current-voltage characteristics of the fabricated solar cells are shown in Figure 6-1(a). A gradually enhanced Jsc is observed with increased doping. The 0e/dot, 2e/dot to 4e/dot devices exhibited a short circuit current density of 10.1 mA/cm^2, 11.8 mA/cm^2 and 12.6 mA/cm^2 respectively. A summary of their detailed performances is shown in Table 6-1.

Table 6-1 Device Performance of 0e/dot, 2e/dot and 4e/dot device

	Jph(mA/cm^2)	**Voc(V)**	**FF(%)**	**Effi.(%)**	**J_{01}(mA/cm^2)**	**J_{02}(mA/cm^2)**
0e/dot	10.1	0.880	76.8	6.82	1.2×10^{-14}	6.2×10^{-8}

2e/dot	11.8	0.893	77.3	8.13	8.2×10^{-15}	5.5×10^{-8}
4e/dot	12.6	0.895	78.0	8.82	7.4×10^{-15}	9.3×10^{-8}

To evaluate the origins of the enhancement of Jsc with further n-doping, we have performed an absolute EQE measurement for above bandgap photoresponse, as shown in Figure 6-1(b). The results show that the 4e/dot device has higher external quantum efficiency than the undoped device. From the integration with the solar spectrum data provided by Oriel, we found that the above bandgap photons contribute to ~12.3 mA/cm^2 for the 4e/dot device and ~10 mA/cm^2 for the 0e/dot device. The result strongly suggests that the total measured overall Jsc mainly comes from the above bandgap photocurrent. We have also used a bulk GaAs wafer as a natural filter to filter out the above bandgap light from the solar simulator. The resulting photon current is around 0.15 mA/cm^2, which is comparatively small. As a result, after careful investigation with experimental results, we conclude that in these sets of devices, the extra absorption of sub bandgap photons is insignificant in determining the total Jsc. Further analysis of below bandgap absorption will appear later. However, the conclusion which appeared in ref (Sablon et al., 2011) is in disagreement with our measurements. In that work, the author claims a sub-bandgap photocurrent as large as 9 mA/cm^2 for a 6e/dot device while above bandgap photons generate 15 mA/cm^2, and concludes

that n doping the quantum dot region significantly improve the IR harvesting. First of all, given the total available number of above and below bandgap photons in the solar spectrum and the fact that the EQE drops substantially when going from higher energy to lower energy photons across the band edge, we have estimated that the sub-bandgap photocurrent will account for only a slight enhancement of Jsc (much less than 1 mA/cm^2)).

The agreement of the overall Jsc and the absolute above bandgap EQE integration with the solar spectrum lead us to believe that the enhancement of the Jsc with doping is mainly coming from the carrier collection efficiency difference of above bandgap photons. Given the extremely high absorption coefficient of above bandgap photons in GaAs, most of the incident photons will be absorbed close to the surface of the device, as shown in Figure 6-2(a). The majority of above bandgap photocarriers is generated before the quantum dot region. The generated holes are directly collected with the p-type electrode through a diffusion process. The generated electrons, however, need to be transported through the QDs region and the n-type base layer in order to be collected. Furthermore, the band offset of strained $In_{0.5}Ga_{0.5}As$ and GaAs appears mainly on the conduction band side while the hole-confined states are thermally connected. As a result, the QD electron-confined states can function as electron traps. The band diagram is shown in Figure 6-2(c).

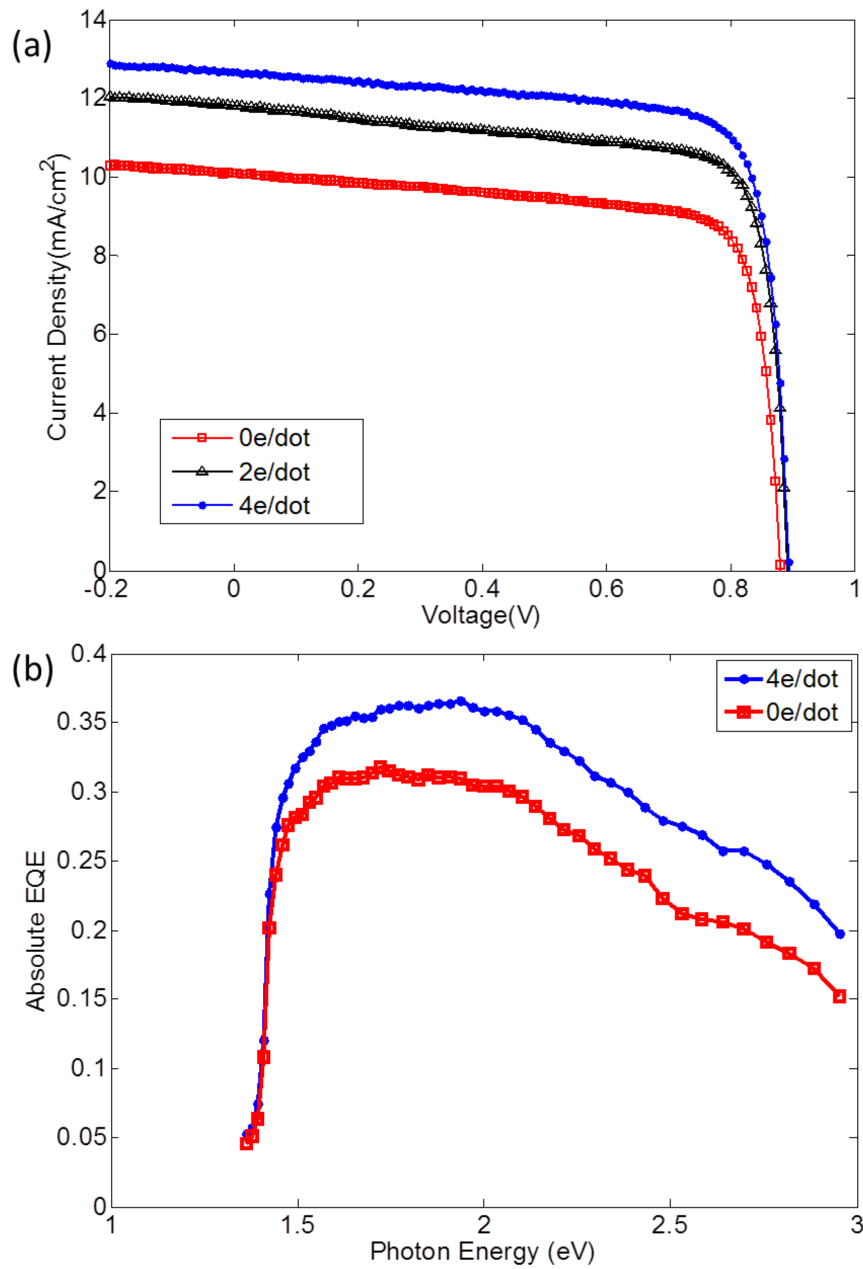

Figure 6-1: (a) Current-voltage characteristics of undoped, 2e/dot and 4e/dot devices (b) above bandgap absolute EQE of 0e/dot and 4e/dot

To explain the impact of electron doping on the carrier collection efficiency, we would like to make a comparison between confined quantum energy state occupation and impurity deionization processes. The quantum dots act as impurities/defect centers in the forbidden band. An impurity band will form as a consequence of increased impurity concentration when the trapped electron/hole wavefunction overlap. Similarly, the evolution of the discrete quantum states into intermediate band happens when electrons in quantum dot confined states become delocalized with an interspacing of less than 10 nm. For an electron trapping center, the trapping potential from this impurity disappears when fully occupied. Most of the impurities are one-electron trap. That is to say, after one electron has been trapped, the trap state no longer exists for trapping a second electron. The process is explained as a carrier screening effect. We found that this method is also applicable to explain the screened Coulomb potential energy of n-doped quantum dots(Dalgarno et al., 2008). The $In_{0.5}Ga_{0.5}As/GaAs$ quantum dots, without any intentional doping, have unoccupied ground or excited states. They potentially act as electron capturing centers(Turchinovich et al., 2003). When the quantum dot levels are partially occupied by electrons, they electrically weaken the trapping potential and even exert a repulsive force to the surrounding mobile electrons. The process is illustrated in Figure 6-2(b). When the above-bandgap photo-generated electrons transport through the QDs layer, the repulsive force exerted by the negatively charged QDs can alter the electron trajectory in such a

way to reduce the probability of electron trapping. This explains why a large photocurrent is measured for more highly doped QDs.

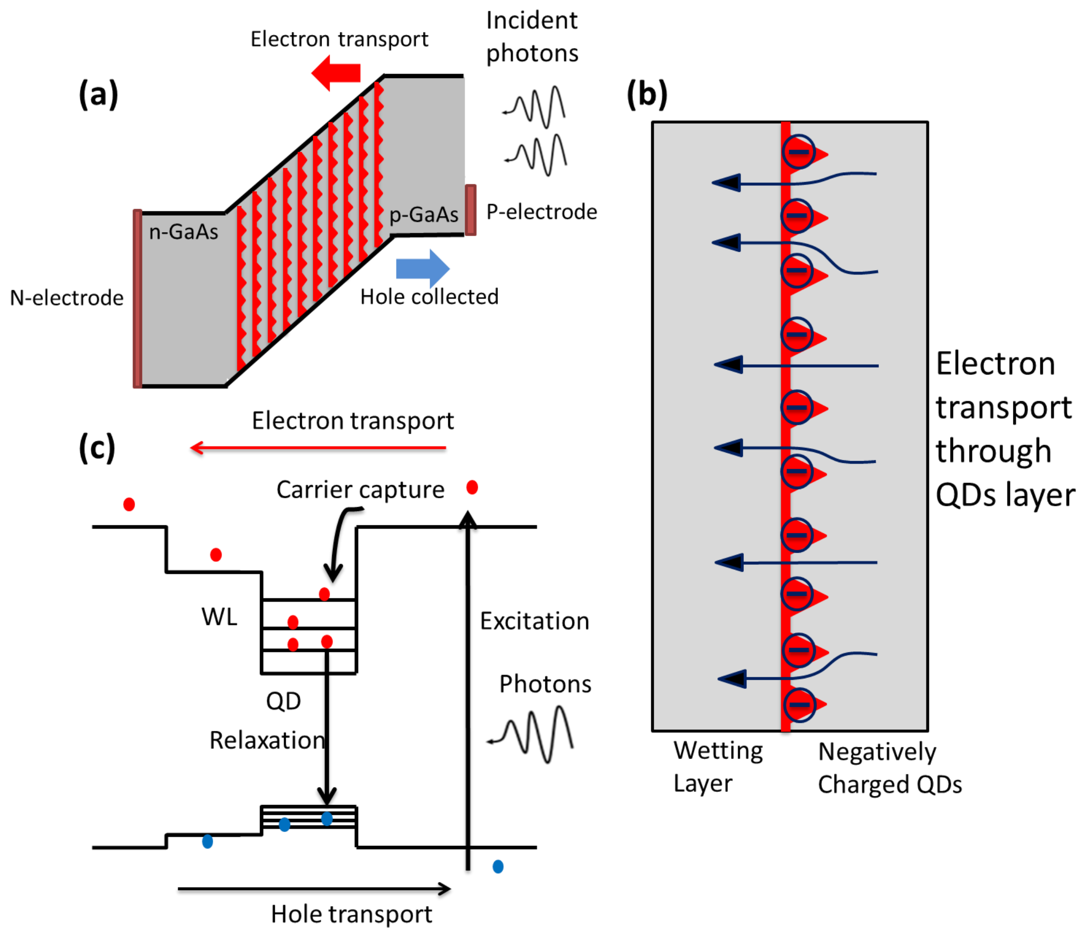

Figure 6-2: The majority of the above bandgap photo carriers are generated close to the device surface due to the large absorption coefficient of the incident photons. (a) Holes are directly collected at the p-electrode while above bandgap generated electrons need to transport through the QDs region and collected at n-electrode. (b) Electrons transport through a single QDs layer. (c) Electrons transport through one quantum dot.

6.2 The impact of electron doping on quantum dot energy states absorption and emission

In order to further investigate the sub-bandgap photocurrent generation, we have performed a high sensitivity below-bandgap EQE measurement (see Figure 6-3). The wetting layers transition is centered around 1.30 eV and the QDs transition is centered around 1.08 eV. As can be directly observed, the 0e/dot device has a much higher EQE value measured at the QD transition energy as compared to the doped QD devices. The explanation is quite straightforward. The available number of unoccupied confined electron states is reduced with further doping. According to the Fermi's Golden rule, the total transition rate decreases correspondingly. The reduction of the absorption in QDs in the presence of doping is a direct manifestation of the Pauli exclusion principle.

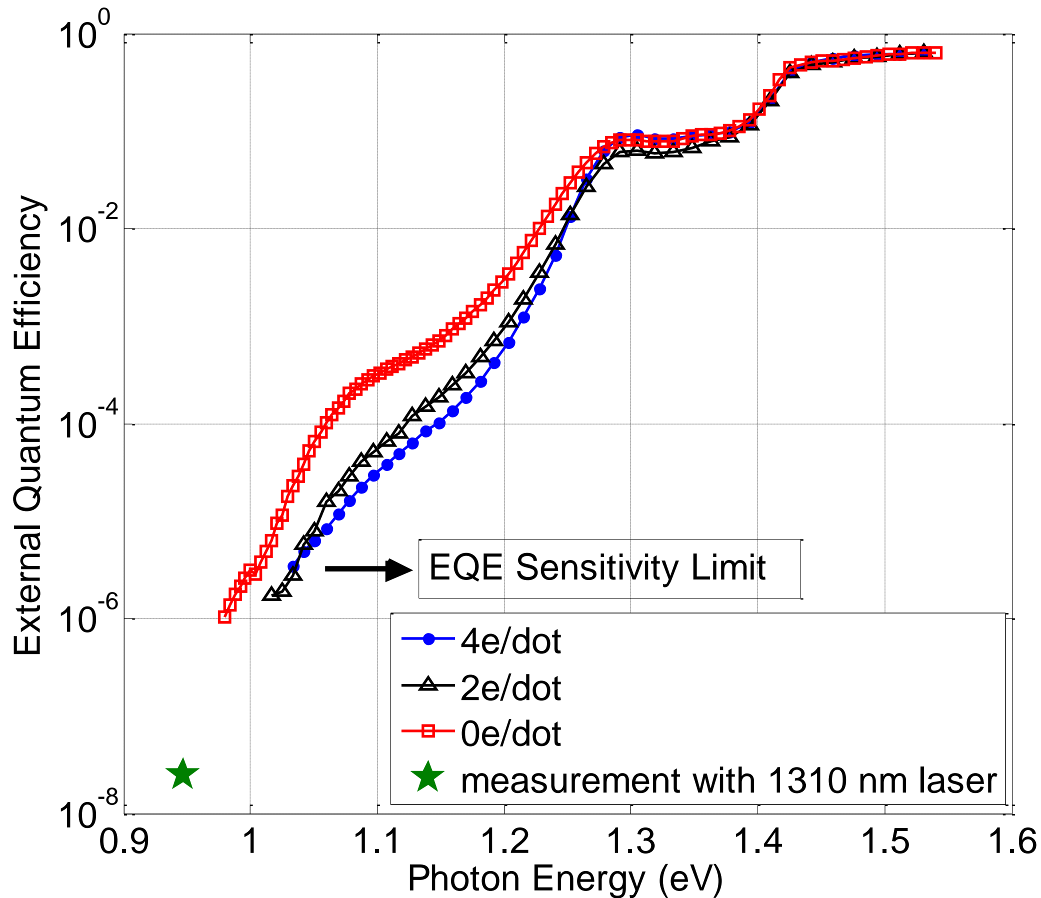

Figure 6-3: Normalized EQE for evaluating below bandgap photon response

We have also compared the photoluminescence of the 0e/dot, 2e/dot and 4e/dot devices. From the results shown in Figure 6-4, the intensity of quantum dots emission reduces as the doping increases. The Si dopants were incorporated 10 nm below the QDs layer, thus the dots sizes should be similar despite the different doping level. It was recently suggested that Si dopants might have a positive impact on improving the crystal quality around quantum dots(Yang et al., 2013). Our measurements do not indicate an improvement in the crystal quality as

the Si doping increases. This can be seen from the fact that the slope of the Urbach tail does not change much as the doping increases from 0e/dot to 4e/dot.

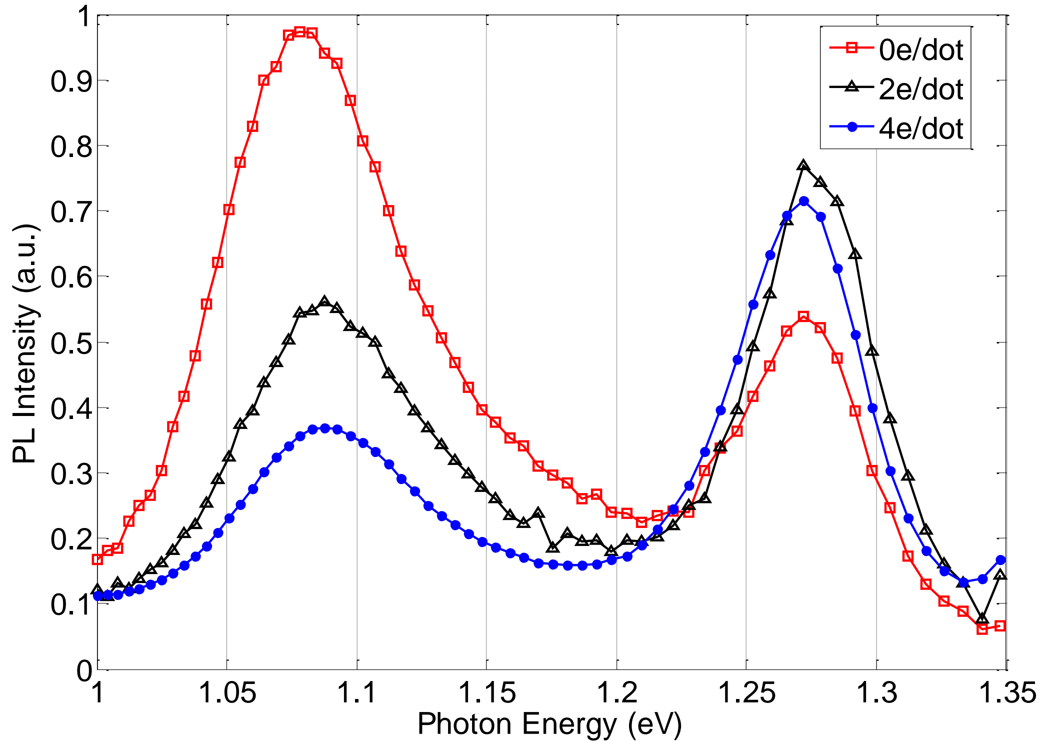

Figure 6-4: Photoluminescence of 0e/dot, 2e/dot and 4e/dot devices

The drift and diffusion field drive the mobile electrons along the film growth direction. When the electrons transport through the QDs layers, they are also driven by the repulsive Coulomb force. Consequently, the electrons tend to circumvent the quantum dots. The doped QDs thus traps fewer electrons. Our proposed theory is again in agreement with the PL results. The 0e/dot shows the highest emission intensity at the QDs ground state transition energy simply because the undoped QDs trap more electrons into the confined states.

The carries can relax through a continuum background. The mechanism was first observed by Toda(Toda et al., 1999). We have investigated this in further detail and have derived an exponential distribution of the continuum density of states. Additionally, the exponential absorption tail can also function as an efficient collection pathway for single photon generated electrons, especially in InAs/GaAs QDs system, competing with a two photon absorption process.

When the electrons are trapped in the quantum dot states, they can release their excess energy by emitting a photon. This photon is not reabsorbed since the absorption coefficient at the QD ground state energy is small (of order 100 cm^{-1} or less). The electrons at the quantum dot states are difficult to be collected if there is a lack of efficient collection mechanism. In our previous work, we derived a greatly broadened continuum density of states surrounding the confined quantum states that function as efficient relaxation and collection pathway in an InAs/GaAs quantum dot device. The Urbach energy was previously measured to be ~ 50 meV. In the present work, we have derived a much smaller Urbach energy of 30 meV for this set of InGaAs/GaAs quantum dots. This is expected since the interface strain is much less between $In_{0.5}Ga_{0.5}As$ and GaAs compared with InAs and GaAs. The tail contributed EQE around the $In_{0.5}Ga_{0.5}As$/GaAs QDs ground state is as low as 5×10^{-6} compared with 2×10^{-3} for the highly strained InAs/GaAs quantum dot device that we previously tested. This significant difference strongly suggests that the density of states of the continuum background around the ground state energy in the InGaAs QDs is much lower.

A narrow absorption tail leads to the observation of two separate luminescent peaks at the QDs and WL respectively, as shown in Figure 6-4. If the carriers at the wetting layer level can easily relax via the greatly broadened continuum background to the QDs ground state, only one emission peak at the QD ground energy can be observed in PL, as we have previously observed in InAs/GaAs QDs.

To conclude, we have evaluated the n-doping effect in $In_{0.5}Ga_{0.5}As/GaAs$ quantum dot solar cell. We found that electron doping of QDs leads to reduced quantum dot absorption as expected from the Pauli exclusion principle. Also, through careful investigation, we believe that the enhanced Jsc comes from a higher carrier collection efficiency of especially above bandgap photon generated electrons. This has been confirmed by an integration of the above bandgap absolute EQE with AM 1.5G solar spectrum. The negatively charged quantum dots exert a repulsive force in the planar direction on the mobile electrons when they travel through the QDs layers. This reduces the number of trapped electron by quantum dot confined states. This theory was further validated by a PL measurement where the reduced ground state emission in charged dots can be explained by the reduced total number of electrons that are trapped by QDs.

7 Summary

To summarize our key achievements of the present work to the field of QD IBSC, we list below some of the first time contributions.

1. We have realized an InAs/GaAs quantum dot solar cells with an efficiency of 17.8% with a **record** current density of 29.9 mA/cm^2.
2. We have incorporated the extended tailing density of states into the density of state model of QDSC.
3. We have demonstrated the significance of incorporating an extended Urbach tail absorption in analyzing quantum dot devices and separated the contribution to Jsc of the tail, QD states and WL states using room temperature EQE measurements.
4. We have developed a method to determine the width of the tail with below-bandgap EQE semi-log plot.
5. We have located the QD state transition with room temperature EQE measurement, the results are in agreement with others using photo-reflectance measurement.
6. We have introduced a z-scan technique to evaluate the non-linear opto-electronic measurement. The two-photon absorption is proven to be via the tailing density of state rather than the QD isolated states. The biggest advantage of our method over others is that it can clearly differentiate the two-

photon process with other non-linear one-photon process such as intensity saturation effect and heating effect.

7. We have correlated the photoluminescence results with the measure Voc based on the width of the tailing density of states. Generally, for a QDSC with larger Voc, the PL results usually show two peaks. One centered at the lowest QD state and the other one centered at the WL state. For those who only have one PL peak, the Voc is generally smaller. The reasoning behind this is that: the extended tail functions as an efficient carrier relaxation/extraction pathway. When the tail is wide enough, the carriers can relax to the lowest QD states before they recombine. However, with a narrower tail, the rate of recombination process at WL states is comparable with the rate of relaxation so that two peaks can be observed.
8. We have modified the SQ model to theoretically evaluate the increase of the dark saturation current density, which leads to the degradation of Voc.
9. With the characterization systems we have set up in our lab for mid-IR and near-IR photons detection within an ensemble of quantum dots, we have made the first observation of the effect of extended tailing states on the sub-bandgap photocurrent generation in QDs. If we consider the InAs/GaAs self-assembled QDs for example, the absorption via the extended tailing distribution of density of states contributes more than half of the total sub-bandgap current.
10. Based on all the discussion above, we have summarized the fundamental limiting factors of the conversion efficiency of the quantum dot intermediate

band solar cells. First, a modified detailed balance analysis shows that by the incorporation of QDs, the existence of an extended tailing density of states would fundamentally enhance the dark saturation density thus degrade the open circuit voltage. Second, the signal generated by IR photons absorption via a transition from QD states to conduction band is too small to match the current generated via the transition from valance band to QD states, thus rendering it impossible to utilize InAs/GaAs QD for the realization of the IBSC model with any significant extra conversion efficiency.

We have focused our research with the hope of providing guidance toward a more practical implementation of photovoltaic devices using advanced nano-device structures. By improving an understanding of the physics in nano-structures, we hope that nano-structure will lead the way to achieving higher conversion efficiency solar cells in future devices.

Appendix

A. An introduction to the Shockley-Queisser model (Detailed Balance limit calculation)

The Shockley-Queisser model assumes a detailed balance between the generation of carriers due to light absorption and radiative recombination. It gives the maximum efficiency of a pn junction solar converter. The detailed balance model is based on the assumptions that each above Eg photon will create an electron hole pair and each electron hole pair will either be collected as current or radiatively recombine.

The spectral photon flux of the sun is

$$F_S = \frac{2}{h^3c^2}\frac{E^2}{e^{\frac{E}{k_BT_S}} - 1}$$

Where h is the Planck 's constant, c is the speed of light and k_B is the Boltzmann constant. E is the photon energy. Ts is the temperature of the Sun. The total absorbed photon number is:

$$N_{abs} = \int_{\Omega} \int_S \int_E Fs \cdot a(E)\cos(\theta)\, dEdSd\Omega$$

In the above expression, a(E) is the absorbance or absorptivity which means the probability to absorb a photon. θ is the projection angle of the absorption cone. The first integration is over the solid angle of absorption. dΩ can be expressed as

2πsinθdθ. The second integration is over the solid surface and the third one is over the energy of the photons. Generally, the absorption angle θ can go from 0 to π/2. The illumination causes the density of EH pairs to increase above the equilibrium values E_F and this makes the Fermi energy to split. Under this condition, the spontaneous emission rate increases as well. Now the photon emission from the cell has become:

$$N_{emit} = \int_{\Omega}\int_{S}\int_{E} e(E)\frac{2}{h^3c^2}\frac{E^2}{e^{\frac{E-qV}{k_BT_c}}-1}\cos(\theta)\,dEdSd\Omega$$

Where e(E) is the emissivity which is the probability that the photon emits.

For a solar cell, the extracted current is given by the electron charge × (the amount of absorbed photon - the amount of emitted photons):

$$\begin{aligned} \mathrm{I} &= \mathrm{q}\cdot(N_{abs}-N_{emit}) \\ &= \mathrm{q} \\ &\cdot\left[\int_{\Omega}\int_{S}\int_{E}\left[a(E)\frac{2}{h^3c^2}\frac{E^2}{e^{\frac{E}{k_BT_S}}-1}\right.\right. \\ &\left.\left.-e(E)\frac{2}{h^3c^2}\frac{E^2}{e^{\frac{E-qV}{k_BT_C}}-1}\right]\cos(\theta)dEdSd\Omega\right] \end{aligned}$$

The left term yields a constant value which is the light-generated current I_L and the right term has a dependence on applied voltage to the cell. Note that in the steady state, current much balance (a(E) = e(E)).

By using

$$\frac{1}{e^{\frac{E-qV}{k_B T_C}}-1} \cong e^{-\frac{E_g}{k_B T_C}} \cdot e^{\frac{qV}{k_B T_C}}$$

The equation for emission current density can be rewritten as

$$\mathrm{q} \cdot \left[\iint_{\Omega} \int_{S} \int_{E} a(E) \frac{2E^2}{h^3 c^2} e^{-\frac{E_g}{k_B T_C}} \cos(\theta)\, dE dS d\Omega \cdot e^{\frac{qV}{k_B T_C}}\right] = I_0 \cdot e^{\frac{qV}{k_B T_C}}$$

$$\mathrm{I} = I_L - I_0 \cdot (e^{\frac{qV}{k_B T_C}} - 1)$$

Under sun illumination, the acceptance angle is θ_S.

$$\tan\theta_S = \frac{R_S}{D_S}$$

Where R_S is the radius of the sun which is $7.0 \times 10^8\ m$, and D_S is the distance between the sun and the earth which is $1.5 \times 10^{11}\ m$. θ_S is calculated to be 0.00467 rad. The photo-generated current density will be:

$$\frac{I_L}{A} = q \int_{\theta=0}^{\theta_S} \cos\theta\ 2\pi \sin\theta\, d\theta \int_{E=E_g}^{\infty} \frac{2}{h^3 c^2} \frac{E^2}{e^{\frac{E}{k_B T_S}} - 1} \mathrm{dE}$$

$$\boldsymbol{= \mathbf{q} \frac{\pi}{2}(1 - \cos 2\theta_S) \int_{E=E_g}^{\infty} \frac{2}{h^3 c^2} \frac{E^2}{e^{\frac{E}{k_B T_S}} - 1} \mathbf{dE}}$$

The light coming from the Sun is from an acceptance angle θ_S. If we use a lens and allow concentration, we will have a concentration factor X. Maximum θ_S is $\frac{\pi}{2}$.

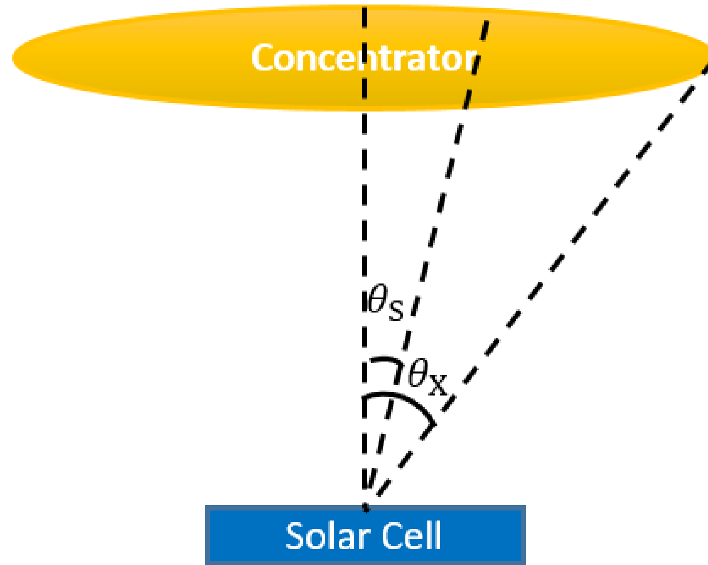

Figure A. 1. Illustration of absorption angle under one sun condition (θ_S) and under concentration (θ_X).

$$X_{max} = \frac{\sin^2 \theta_X}{\sin^2 \theta_S} = \frac{1}{\sin^2 \theta_S} = \frac{1}{\sin^2(0.00467 \text{ rad})} = \mathbf{46050}$$

Typically the emission angle is $\frac{\pi}{2}$, which means that photons are emitted in all directions from the surface. Similarly, the dark current density can be expressed as

$$\frac{I_0}{A} = q\frac{\pi}{2}(1 - \cos 2\theta_E)\int_{E=E_g}^{\infty} \frac{2}{h^3 c^2} \frac{E^2}{e^{\frac{E}{k_B T_C}} - 1} dE$$

To calculate the output power of the solar cell. We need to find the maximum point of the product of extracted current and voltage.

$$P_{out} = IV$$

$$\frac{\mathrm{d}P_{out_Max}}{\mathrm{dV}} = \frac{\mathrm{d(I \cdot V)}}{\mathrm{dV}} = \frac{\mathrm{d}}{\mathrm{dV}}\left[I_L - I_0 \cdot (e^{\frac{qV}{k_B T_C}} - 1)\right]$$

$$= I_L - I_0 \cdot [\frac{q}{k_B T_C} e^{\frac{qV}{k_B T_C}} \cdot V + (e^{\frac{qV}{k_B T_C}} - 1)] = 0$$

This equation can then be solved numerically to obtain the value of operation voltage at the maximum power output (V_M).

The expression for V_M is

$$qV = Eg\ \left(1 - \frac{Tc}{Ts}\right) - K_B T_C \ln \frac{1 - \cos(2\theta_e)}{1 - \cos(2\theta_s)}$$

The first term is the “Carnot loss” and the second term is the “Boltzmann loss”.

The value of I_M can also be obtained by taking V_M back to the equation. The overall conversion efficiency is

$$\boldsymbol{\eta} = \frac{\boldsymbol{P_M}}{\boldsymbol{P_{in}}} = \frac{\boldsymbol{V_M I_M}}{\int_{\Omega} \int_{S} \int_{E=0}^{E=\infty} \boldsymbol{F_S \cdot E \cos(\theta)\, dEdSd\Omega}}$$

E is the energy of that photon and Fs is the spectral photon flux from the Sun. The calculated maximum efficiency under one sun condition with different bandgap for single bandgap solar cell is shown in Figure A. 3.

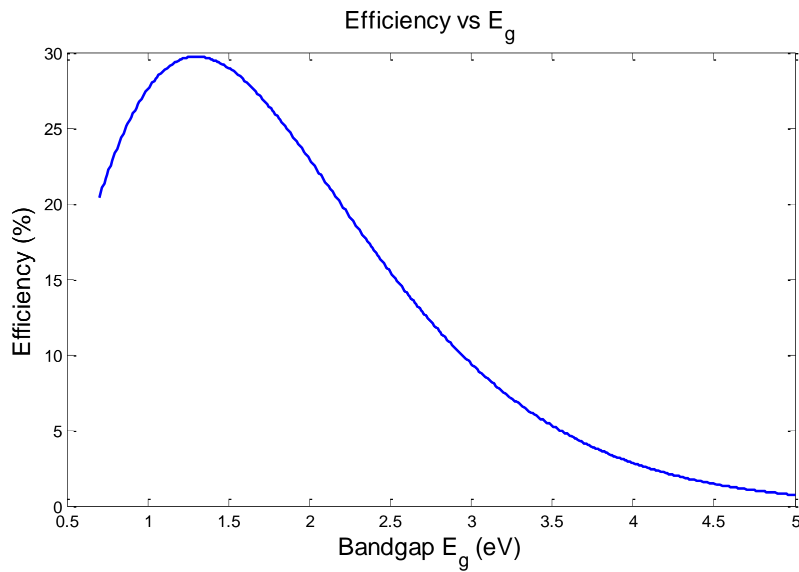

Figure A. 3. Plot of the efficiency limit vs. bandgap

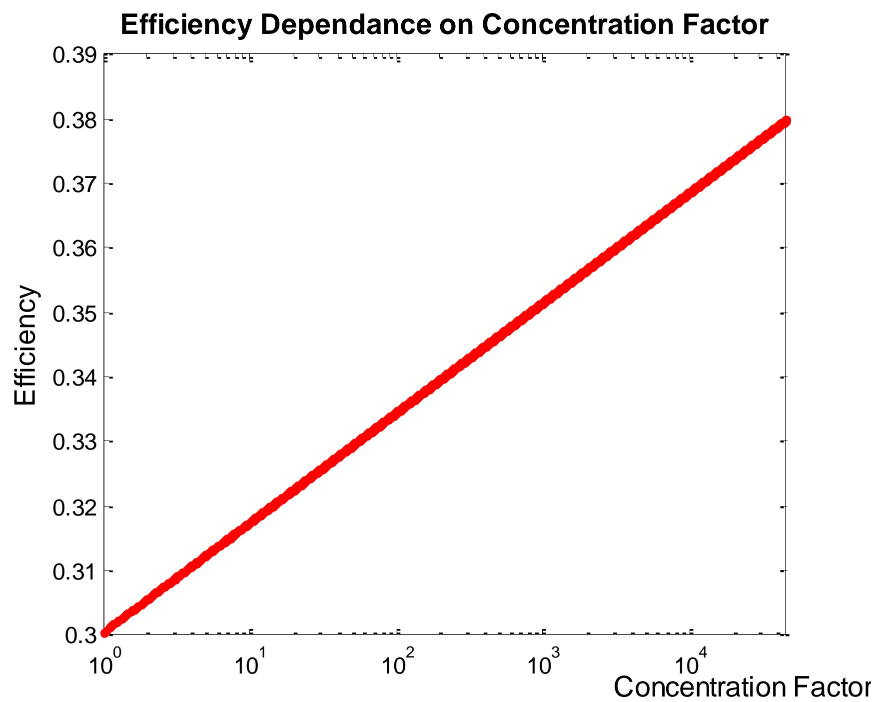

Figure A. 4. Theoretical efficiency vs. concentrator factors for a single bandgap solar cell with $E_G = 1.4$ eV

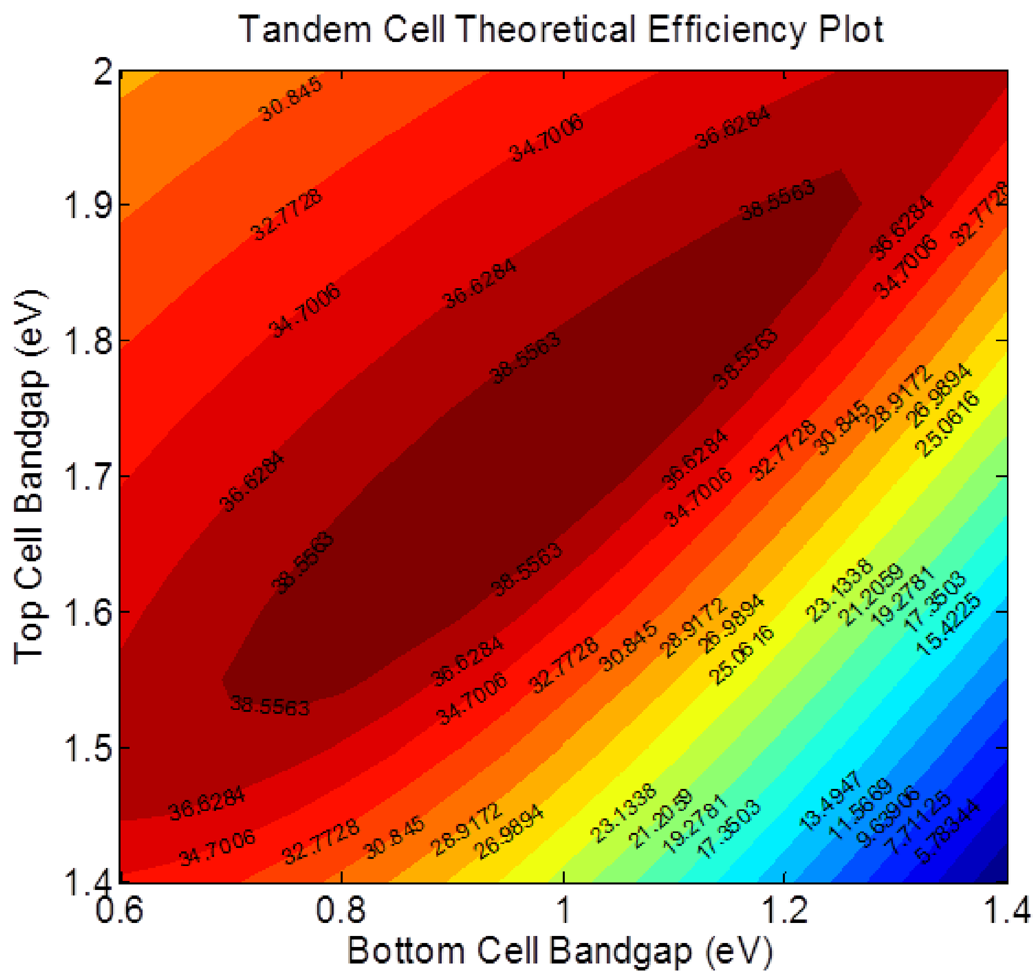

Figure A. 5. Plot of theoretical efficiency vs. bandgap of tandem cell

B. The theoretical efficiency limit of intermediate band model and its assumptions

For the intermediate band model, the theoretical efficiency calculated by Luque and Marti is based on the following assumptions (Luque and Mart í, 1997b):

1. There is no non-radiative transition. The generated carriers will either be extracted or recombine radiatively.
2. Quasi-Fermi level is uniform across the active region. There are three bands: the conduction band, the valance band and the impurity band.
3. No carriers shall be extracted from the impurity band.
4. All photons with a higher energy than the transition energy are absorbed.
5. There is a back-side mirror so that the radiation from the cell only escapes from the surface.
6. Photon absorption occurs across the highest transition possible. In Figure B.1, photons with energy larger than E_G will be absorbed for transition across the valance band to the conduction band; photons with energy lower than Eg but larger than E_C will pump electrons from IB to CB; the transition from CB to IB can be facilitated by the absorption of all the photons with energy between E_I and E_C.

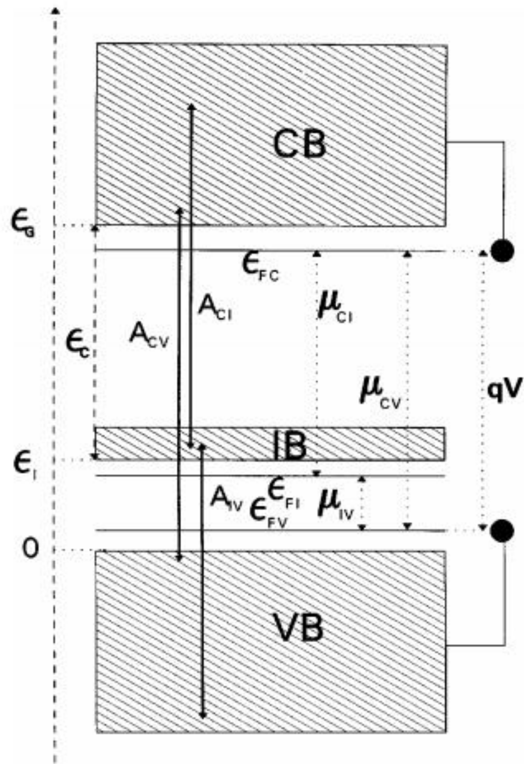

Figure B. 1. Band diagram of the intermediate band solar cell model [(Luque and Martí 1997b)]

Under the above assumptions, the current per area from the conduction band can be written as the combination of the current generated by the valance band to the conduction band transitions and the current generated from the impurity band to the conduction band transitions.

$$
\begin{aligned}
\mathrm{I} = \mathrm{q}\cdot\left[\left(N_{abs_{VBtoCB}} - N_{emit_{VBtoCB}}\right)+\left(N_{abs_{IBtoCB}} - N_{emit_{IBtoCB}}\right)\right] \\
= \mathrm{q} \\
\cdot\left[\int_{\Omega}\int_{S}\int_{E=Eg}^{E=\infty}\left[\frac{2}{h^3c^2}\frac{E^2}{e^{\frac{E}{k_BT_S}}-1}-\frac{2}{h^3c^2}\frac{E^2}{e^{\frac{E-q\mu_{CV}}{k_BT_C}}-1}\right]\cos(\theta)\,dEdSd\Omega\right. \\
\left.+\left[\int_{\Omega}\int_{S}\int_{E=Ec}^{E=Eg}\left[\frac{2}{h^3c^2}\frac{E^2}{e^{\frac{E}{k_BT_S}}-1}-\frac{2}{h^3c^2}\frac{E^2}{e^{\frac{E-q\mu_{CI}}{k_BT_C}}-1}\right]\cos(\theta)\,dEdSd\Omega\right]\right]
\end{aligned}
$$

As the same time, no current should be extracted from the intermediate band so that the carriers generated/emitted from the intermediate band should be balanced out.

$$
\mathrm{I} = \mathrm{q}\cdot\left[\left(N_{abs_{VBtoIB}} - N_{emit_{VBtoIB}}\right)-\left(N_{abs_{IBtoCB}} - N_{emit_{IBtoCB}}\right)\right] = 0
$$

$$
\begin{aligned}
\int_{\Omega}\int_{S}\int_{E=Ec}^{E=Eg}\left[\frac{2}{h^3c^2}\frac{E^2}{e^{\frac{E}{k_BT_S}}-1}-\frac{2}{h^3c^2}\frac{E^2}{e^{\frac{E-q\mu_{CI}}{k_BT_C}}-1}\right]\cos(\theta)\,dEdSd\Omega \\
= \int_{\Omega}\int_{S}\int_{E=Ei}^{E=Ec}\left[\frac{2}{h^3c^2}\frac{E^2}{e^{\frac{E}{k_BT_S}}-1}-\frac{2}{h^3c^2}\frac{E^2}{e^{\frac{E-q\mu_{IV}}{k_BT_C}}-1}\right]\cos(\theta)\,dEdSd\Omega
\end{aligned}
$$

The output voltage should be the splitting between the electron quasi-Fermi level and the hole quasi-Fermi levels:

$$
qV = \mu_{CV}
$$

According the above assumptions, an efficiency as high as 63.2 % was obtained with the total bandgap Eg=1.93 eV and Ei= 0.7 eV under maximum concentration. In this ideal structure, photons with energy between 0.7 eV to 1.23 eV will contribute to the transitions from the valance band to the intemediate band and

will balance out the transition from the intemediate band to the conduction band which absorbs all the photons with energy from 1.23 eV to 1.93 eV. The calculation results are ploted in Figure B. 3 [(Luque and Mart í 1997b, Jenks, S., Gilmore, R., 2014.)]. The absorption specturm is shown in the following figure.

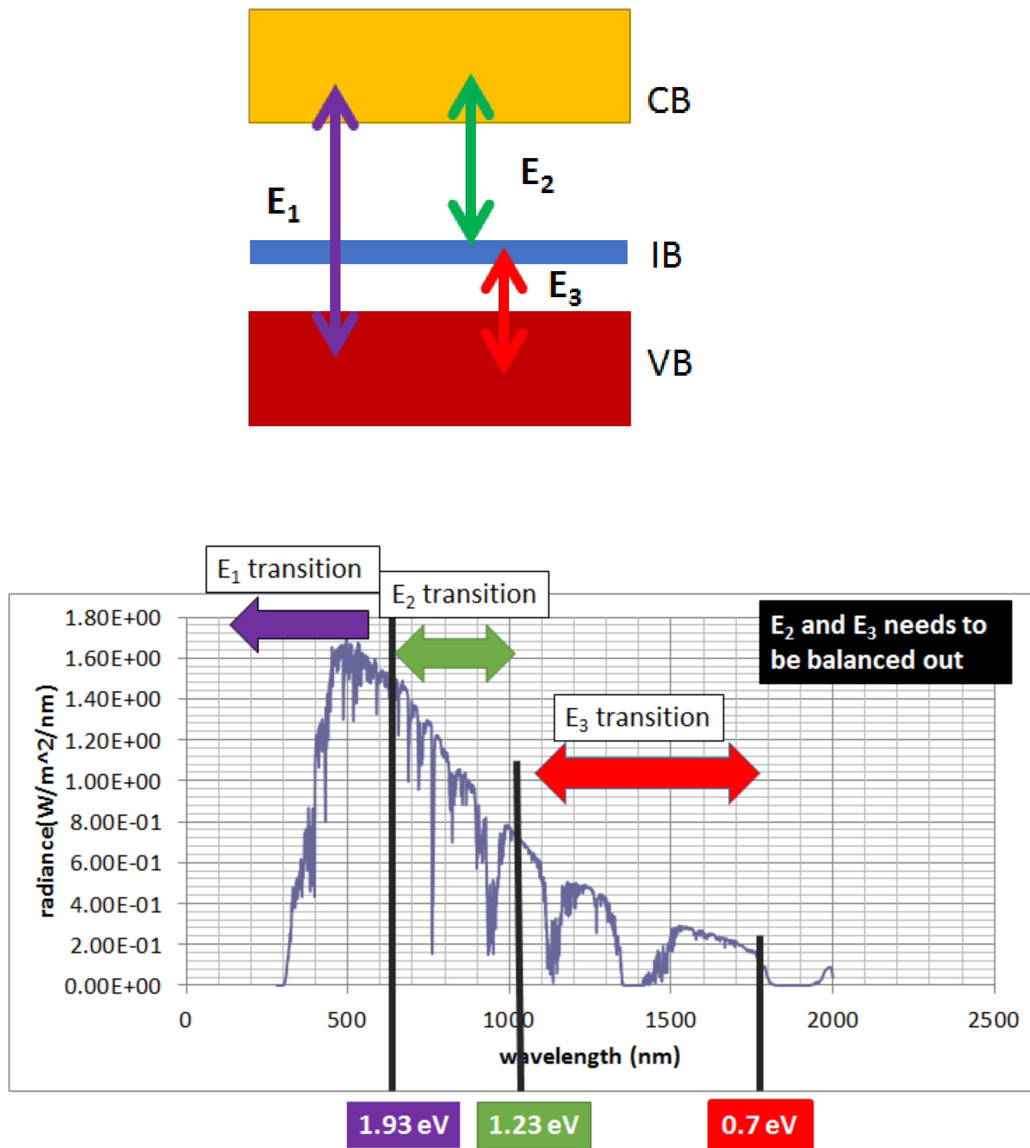

Figure B. 2. The absorption spectrum of an ideal intermediate band solar cell model with bandgap of 1.93 eV and an energy seperation between the valance band and the intermediate band of 0.7 eV.

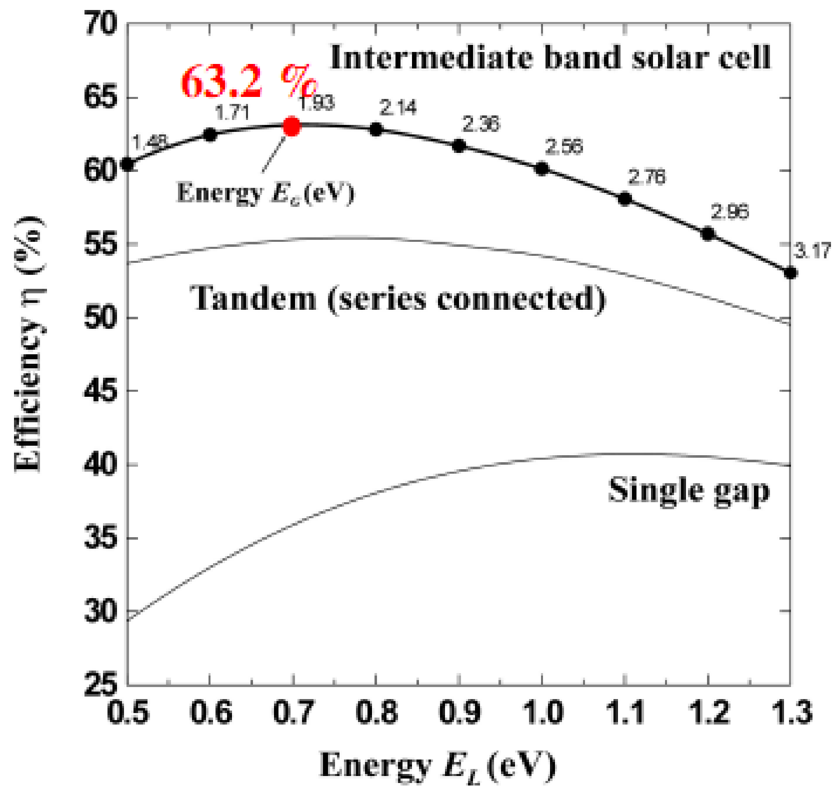

(a)

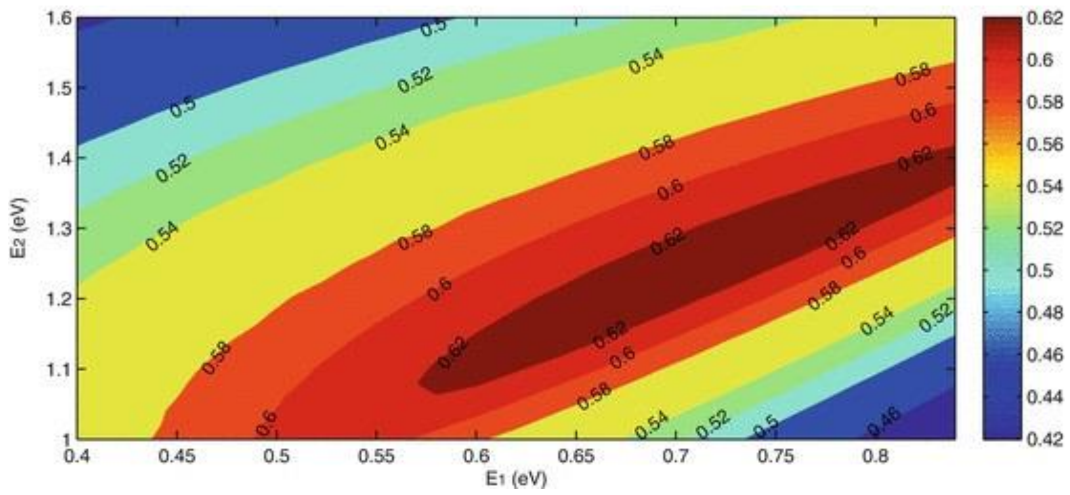

(b)

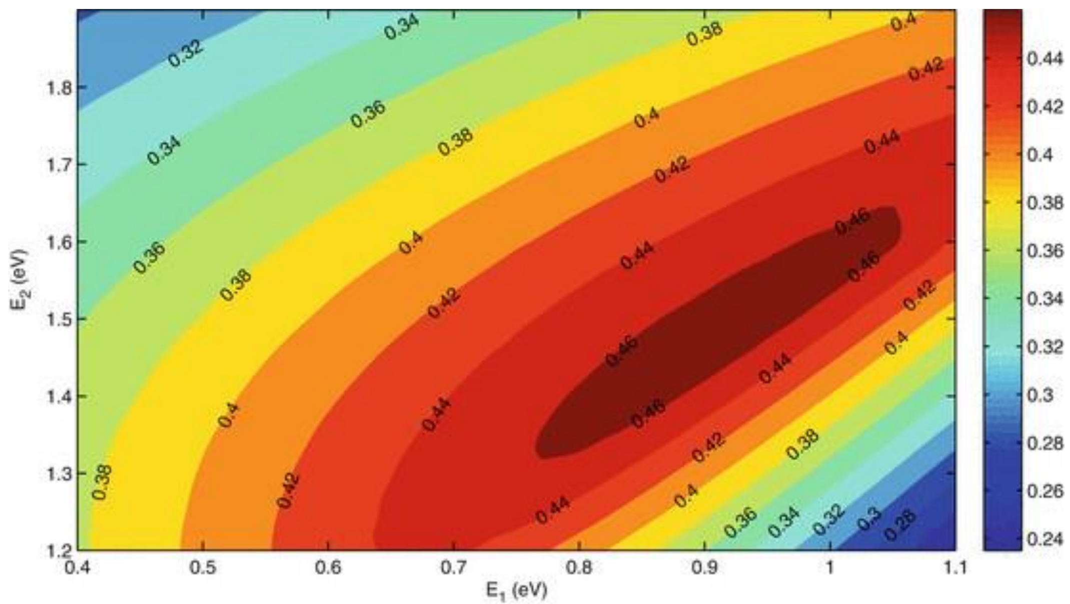

(c)

Figure B. 3. (a)(b) Intermediate band solar cell efficiency under concentration with different band gap energy. (c) Intermediate band solar cell efficiency vs. bandgap under 1 sun condition [(Luque and Mart í 1997b.)].

Bibliography

Aigouy, L., Holden, T., Pollak, F.H., Ledentsov, N.N., Ustinov, W.M., Kop'ev, P.S., Bimberg, D., 1997. Contactless electroreflectance study of a vertically coupled quantum dot-based InAs/GaAs laser structure. Appl. Phys. Lett. 70, 3329. doi:doi:10.1063/1.119160

Alén, B., Bickel, F., Karrai, K., Warburton, R.J., Petroff, P.M., 2003. Stark-shift modulation absorption spectroscopy of single quantum dots. Appl. Phys. Lett. 83, 2235–2237. doi:doi:10.1063/1.1609243

Aslan, B., Liu, H.C., Korkusinski, M., Cheng, S.-J., Hawrylak, P., 2003. Response spectra from mid- to far-infrared, polarization behaviors, and effects of electron numbers in quantum-dot photodetectors. Appl. Phys. Lett. 82, 630–632. doi:doi:10.1063/1.1540728

Bailey, C.G., Forbes, D.V., Polly, S.J., Bittner, Z.S., Dai, Y., Mackos, C., Raffaelle, R.P., Hubbard, S.M., 2012. Open-Circuit Voltage Improvement of InAs/GaAs Quantum-Dot Solar Cells Using Reduced InAs Coverage. IEEE J. Photovolt. 2, 269–275. doi:10.1109/JPHOTOV.2012.2189047

Bailey, C.G., Forbes, D.V., Raffaelle, R.P., Hubbard, S.M., 2011. Near 1 V open circuit voltage InAs/GaAs quantum dot solar cells. Appl. Phys. Lett. 98. doi:10.1063/1.3580765

Bayer, M., Forchel, A., 2002. Temperature dependence of the exciton homogeneous linewidth in In_{0.60}Ga_{0.40}As/GaAs self-assembled

quantum dots. Phys. Rev. B 65, 041308. doi:10.1103/PhysRevB.65.041308

Birkedal, D., Bloch, J., Shah, J., Pfeiffer, L.N., West, K., 2000. Femtosecond dynamics and absorbance of self-organized InAs quantum dots emitting near 1.3 μm at room temperature. Appl. Phys. Lett. 77, 2201–2203. doi:doi:10.1063/1.1315347

Borri, P., Langbein, W., Schneider, S., Woggon, U., Sellin, R.L., Ouyang, D., Bimberg, D., 2001. Ultralong Dephasing Time in InGaAs Quantum Dots. Phys. Rev. Lett. 87, 157401. doi:10.1103/PhysRevLett.87.157401

Braun, A., Katz, E.A., Feuermann, D., Kayes, B.M., Gordon, J.M., 2013. Photovoltaic performance enhancement by external recycling of photon emission. Energy Environ. Sci. 6, 1499–1503. doi:10.1039/C3EE40377G

Cánovas, E., Martí, A., Fuertes Marrón, D., Antolín, E., Linares, P.G., Luque, A., Farmer, C.D., Stanley, C.R., 2008. Optical characterization of quantum dot intermediate band solar cells. Presented at the Proc. 23rd Eur. Phot. Solar Energy Conf., Proc. 23rd Eur. Phot. Solar Energy Conf., Valencia-Spain.

Chen, Z., Baklenov, O., Kim, E.T., Mukhametzhanov, I., Tie, J., Madhukar, A., Ye, Z., Campbell, J.C., 2001. Normal incidence InAs/AlxGa1−xAs quantum dot infrared photodetectors with undoped active region. J. Appl. Phys. 89, 4558–4563. doi:doi:10.1063/1.1356430

Chuang, S.L., 2009. Photodetectors and Solar Cells, in: Physics of Photonic Devices. John Wiley & Sons, Hoboken, NJ, USA, pp. 740–743.

Dagenais, M., Li, T., Zhang, Y., Bartolo, R., 2013. Intermediate Band Solar Cells: Promises and Reality, in: International Photonics and Optoelectronics Meetings (POEM), OSA Technical Digest (online). Presented at the International Photonics and Optoelectronics Meetings (POEM), Optical Society of America, p. ASa2A.1. doi:10.1364/AOEE.2013.ASa2A.1

Dalgarno, P.A., Smith, J.M., McFarlane, J., Gerardot, B.D., Karrai, K., Badolato, A., Petroff, P.M., Warburton, R.J., 2008. Coulomb interactions in single, charged self-assembled quantum dots: radiative lifetime and recombination energy. Phys. Rev. B 77. doi:10.1103/PhysRevB.77.245311

Ding, D., Johnson, S.R., Yu, S.-Q., Wu, S.-N., Zhang, Y.-H., 2011. A semi-analytical model for semiconductor solar cells. J. Appl. Phys. 110, 123104. doi:10.1063/1.3671061

Gardner, J., Albers, E., Bailey, C.G., Hubbard, S., Raffaelle, R., 2009. Thermal and spectroscopic characterization of quantum dot-enhanced solar cells, in: 2009 34th IEEE Photovoltaic Specialists Conference (PVSC). Presented at the 2009 34th IEEE Photovoltaic Specialists Conference (PVSC), pp. 000993–000998. doi:10.1109/PVSC.2009.5411190

Greeff, C.W., Glyde, H.R., 1995a. Anomalous Urbach tail in GaAs. Phys. Rev. B 51, 1778–1783. doi:10.1103/PhysRevB.51.1778

Greeff, C.W., Glyde, H.R., 1995b. Anomalous Urbach tail in GaAs. Phys. Rev. B 51, 1778–1783. doi:10.1103/PhysRevB.51.1778

Green, M.A., Emery, K., Hishikawa, Y., Warta, W., Dunlop, E.D., 2014. Solar cell efficiency tables (version 44). Prog. Photovolt. Res. Appl. 22, 701–710. doi:10.1002/pip.2525

Green, M.A., Emery, K., Hishikawa, Y., Warta, W., Dunlop, E.D., 2013. Solar cell efficiency tables (version 41). Prog. Photovolt. Res. Appl. 21, 1–11. doi:10.1002/pip.2352

Harbord, E., Spencer, P., Clarke, E., Murray, R., 2009. Radiative lifetimes in undoped and p-doped InAs/GaAs quantum dots. Phys. Rev. B 80, 195312. doi:10.1103/PhysRevB.80.195312

Johnson, S.R., Tiedje, T., 1995. Temperature dependence of the Urbach edge in GaAs. J. Appl. Phys. 78, 5609–5613. doi:doi:10.1063/1.359683

Jolley, G., Lu, H.F., Fu, L., Tan, H.H., Jagadish, C., 2010. Electron-hole recombination properties of In0.5Ga0.5As/GaAs quantum dot solar cells and the influence on the open circuit voltage. Appl. Phys. Lett. 97, 123505–123505–3. doi:doi:10.1063/1.3492836

Kadlec, F., Němec, H., Kužel, P., 2004. Optical two-photon absorption in GaAs measured by optical-pump terahertz-probe spectroscopy. Phys. Rev. B 70. doi:10.1103/PhysRevB.70.125205

Laghumavarapu, R.B., El-Emawy, M., Nuntawong, N., Moscho, A., Lester, L.F., Huffaker, D.L., 2007. Improved device performance of InAs/GaAs quantum dot solar cells with GaP strain compensation layers. Appl. Phys. Lett. 91, 243115–243115–3. doi:doi:10.1063/1.2816904

Li, T., Amirloo, J., Murray, J., Sablon, K.A., Little, J., Uppal, P., Munday, J., Dagenais, M., Sept. A comparison of bulk and quantum dot GaAs solar cells, in: 2012 IEEE Photonics Conference (IPC). Presented at the 2012 IEEE Photonics Conference (IPC), pp. 194–195. doi:10.1109/IPCon.2012.6358557

Li, T., Bartolo, R., Dagenais, M., n.d. GaAs/InAs Quantum Dot High Efficiency Solar Cell. Presented at the 2013 IEEE Photonics.

Li, T., Bartolo, R.E., Dagenais, M., 2013. Challenges to the concept of an intermediate band in InAs/GaAs quantum dot solar cells. Appl. Phys. Lett. 103, 141113. doi:doi:10.1063/1.4822322

Li, T., Dagenais, M., 2014. Urbach tail in intermediate band InAs/GaAs quantum dot solar cells, in: Photovoltaic Specialist Conference (PVSC), 2014 IEEE 40th. Presented at the Photovoltaic Specialist Conference (PVSC), 2014 IEEE 40th, pp. 3622–3625. doi:10.1109/PVSC.2014.6924890

Li, T., Dagenais, M., n.d. Below-Bandgap Absorption in InAs/GaAs Self-Assembled Quantum Dot Solar Cells. Prog. Photovolt. Res. Appl. 2014. 10.1002/pip.2515

Li, T., Lu, H., Fu, L., Tan, H.H., Jagadish, C., Dagenais, M., 2015. Enhanced carrier collection efficiency and reduced quantum state absorption by electron doping in self-assembled quantum dot solar cells. Appl. Phys. Lett. 106, 053902. doi:10.1063/1.4907348

Luque, A., Martí, A., 2010. The Intermediate Band Solar Cell: Progress Toward the Realization of an Attractive Concept. Adv. Mater. 22, 160–174. doi:10.1002/adma.200902388

Luque, A., Martí, A., 1997a. Increasing the Efficiency of Ideal Solar Cells by Photon Induced Transitions at Intermediate Levels. Phys. Rev. Lett. 78, 5014–5017. doi:10.1103/PhysRevLett.78.5014

Luque, A., Martí, A., 1997b. Increasing the Efficiency of Ideal Solar Cells by Photon Induced Transitions at Intermediate Levels. Phys. Rev. Lett. 78, 5014–5017. doi:10.1103/PhysRevLett.78.5014

Martí, A., Antolín, E., Stanley, C., Farmer, C., López, N., Díaz, P., Cánovas, E., Linares, P., Luque, A., 2006. Production of Photocurrent due to Intermediate-to-Conduction-Band Transitions: A Demonstration of a Key Operating Principle of the Intermediate-Band Solar Cell. Phys. Rev. Lett. 97. doi:10.1103/PhysRevLett.97.247701

Miller, O.D., Yablonovitch, E., Kurtz, S.R., 2012. Strong Internal and External Luminescence as Solar Cells Approach the Shockley #x2013;Queisser Limit. IEEE J. Photovolt. 2, 303–311. doi:10.1109/JPHOTOV.2012.2198434

Oshima, R., Takata, A., Shoji, Y., Akahane, K., Okada, Y., 2010. InAs/GaNAs strain-compensated quantum dots stacked up to 50 layers for use in high-efficiency solar cell. Phys. E Low-Dimens. Syst. Nanostructures 42, 2757–2760. doi:10.1016/j.physe.2009.12.036

Pankove, J.I., 1975. Transitions between band tails, in: Optical Processes in Semiconductors. Dover, New York, pp. 43–46.

Sablon, K.A., Little, J.W., Mitin, V., Sergeev, A., Vagidov, N., Reinhardt, K., 2011. Strong Enhancement of Solar Cell Efficiency Due to Quantum Dots with Built-In Charge. Nano Lett. 11, 2311–2317. doi:10.1021/nl200543v

Shockley, W., Queisser, H.J., 1961. Detailed Balance Limit of Efficiency of p-n Junction Solar Cells. J. Appl. Phys. 32, 510–519. doi:doi:10.1063/1.1736034

Shoji, Y., Akimoto, K., Okada, Y., 2013. Self-organized InGaAs/GaAs quantum dot arrays for use in high-efficiency intermediate-band solar cells. J. Phys. Appl. Phys. 46, 024002. doi:10.1088/0022-3727/46/2/024002

Jenks, S., Gilmore, R., 2014. Material selection for the quantum dot intermediate band solar cell. Quantum Dot Solar Cells. DOI: 10.1007/978-1-4614-8148-5_6

Sugaya, T., Numakami, O., Oshima, R., Furue, S., Komaki, H., Amano, T., Matsubara, K., Okano, Y., Niki, S., 2012a. Ultra-high stacks of InGaAs/GaAs quantum dots for high efficiency solar cells. Energy Environ. Sci. 5, 6233–6237. doi:10.1039/C2EE01930B

Sugaya, T., Numakami, O., Oshima, R., Furue, S., Komaki, H., Amano, T., Matsubara, K., Okano, Y., Niki, S., 2012b. Ultra-high stacks of InGaAs/GaAs quantum dots for high efficiency solar cells. Energy Environ. Sci. 5, 6233–6237. doi:10.1039/C2EE01930B

Tanabe, K., Guimard, D., Bordel, D., Arakawa, Y., 2012. High-efficiency InAs/GaAs quantum dot solar cells by metalorganic chemical vapor deposition. Appl. Phys. Lett. 100, 193905–193905–3. doi:doi:10.1063/1.4714767

Toda, Y., Moriwaki, O., Nishioka, M., Arakawa, Y., 1999. Efficient Carrier Relaxation Mechanism in InGaAs/GaAs Self-Assembled Quantum Dots Based on the Existence of Continuum States. Phys. Rev. Lett. 82, 4114–4117. doi:10.1103/PhysRevLett.82.4114

Turchinovich, D., Pierz, K., Uhd Jepsen, P., 2003. InAs/GaAs quantum dots as efficient free carrier deep traps. Phys. Status Solidi C 0, 1556–1559. doi:10.1002/pssc.200303230

Urbach, F., 1953. The Long-Wavelength Edge of Photographic Sensitivity and of the Electronic Absorption of Solids. Phys. Rev. 92, 1324–1324. doi:10.1103/PhysRev.92.1324

Valley, G.C., Boggess, T.F., Dubard, J., Smirl, A.L., 1989. Picosecond pump-probe technique to measure deep-level, free-carrier, and two photon cross sections in GaAs. J. Appl. Phys. 66, 2407–2413. doi:10.1063/1.344248

Yang, X., Wang, K., Gu, Y., Ni, H., Wang, X., Yang, T., Wang, Z., 2013. Improved efficiency of InAs/GaAs quantum dots solar cells by Si-doping. Sol. Energy Mater. Sol. Cells 113, 144–147. doi:10.1016/j.solmat.2013.02.005

Yariv, Amnon, 1989. Quantum Electronics, Third Edition. Wiley.

Zhang, J.-Z., Galbraith, I., 2004. Intraband absorption for InAs/GaAs quantum dot infrared photodetectors. Appl. Phys. Lett. 84, 1934–1936. doi:doi:10.1063/1.1687459

Zheng, Z., Weiner, A.M., Marsh, J.H., Karkhanehchi, M.M., 1997. Ultrafast optical thresholding based on two-photon absorption GaAs waveguide photodetectors. IEEE Photonics Technol. Lett. 9, 493–495. doi:10.1109/68.559399